TRANSDERMAL IONTOPHORESIS OF SMALL MOLECULES

WITH COTRANSPORT OF POLYSTYRENE

SULFONATE OLIGOMERS

Mark Rulon Liddell

A dissertation submitted to the faculty of
The University of Utah
in partial fulfillment of the requirements for the degree of

Doctor of Philosophy

Department of Pharmaceutics and Pharmaceutical Chemistry

The University of Utah

May 2012

The University of Utah Graduate School

STATEMENT OF DISSERTATION APPROVAL

The dissertation of **Mark Rulon Liddell**

has been approved by the following supervisory committee members:

William I. Higuchi	, Chair	**03/14/2012** Date Approved
Steven Kern	, Member	**03/15/2012** Date Approved
Jindrich Kopecek	, Member	**03/14/2012** Date Approved
S. Kevin Li	, Member	**03/15/2012** Date Approved
Henry S. White	, Member	**03/14/2012** Date Approved

and by **David W. Grainger**, Chair of the Department of **Pharmaceutics and Pharmaceutical Chemistry**

and by Charles A. Wight, Dean of The Graduate School.

ABSTRACT

The fluxes of ionic and nonionic probe permeants across hairless mouse skin (HMS) were induced by direct current (DC) iontophoresis and used to characterize the transport pathways of the epidermal membrane under two conditions: 1) with phosphate buffered saline (PBS) in both the anodal and cathodal chamber, referred to as baseline studies; and 2) with PBS in the anodal chamber and with sodium polystyrene sulfonate (PSS) in the cathodal chamber. Probe permeants used in these experiments were nonionic permeants (urea, mannitol, and raffinose), monovalent cationic permeants (sodium, tetraethylammonium, and tetraphenylphosphonium ions), and monovalent anionic permeants (chloride, salicylate, and taurocholate ions). The permeability coefficients of the nonionic probe permeants increased up to sixfold with sodium PSS in the cathodal chamber. Increases in the permeability coefficients of nonionic permeants were independent of the sodium PSS concentrations (sodium PSS concentrations investigated included 1.37, 13.7 and 137 mg/mL). Permeability coefficients of the cationic probe permeants also increased up to threefold relative to baseline results and remained constant, independent of the sodium PSS concentration in the cathodal chamber. The permeability coefficients of the anionic probe permeants increased slightly relative to baseline results with 1.37 mg/mL sodium PSS in the cathodal chamber and then decreased as the concentration of sodium PSS in the cathodal chamber increased. In addition to investigating the transport behavior of the probe permeants, the modified

Nernst-Planck model was used as a theoretical framework for interpreting the data and calculating the effective pore radius (*Rp*) of pathways available to the probe permeants during iontophoresis. Under baseline conditions the *Rp* values obtained using nonionic permeant transport data ranged from 7 – 13 Å; with sodium PSS in the cathodal chamber *Rp* values ranged from 9 – 27 Å. The results of theoretical Nernst-Planck calculations also helped to explain the transport behavior of the cationic probe permeants and confirmed, based on cationic probe permeant data, that with sodium PSS in the cathodal chamber *Rp* values were in the same range (20 – 30 Å) as those calculated in baseline studies.

For my parents who taught me to never quit, and for

my family who have never quit on me...

...and for Pooh.

TABLE OF CONTENTS

LIST OF TABLES

Table

ACKNOWLEDGMENTS

I would be remiss if I did not recognize the many hours spent by mentors, colleagues, friends, and family that have enabled me to complete this dissertation. I am sincerely grateful to Dr. William Higuchi for allowing me to work under his supervision. He has demonstrated to me that the pursuit of quality scientific endeavor takes time, and requires both patience and tenacity. I feel both honored and somewhat regretful that I am among the last in a long line of graduate students that have studied under his guidance. I am indebted to Dr. Kevin Li, who has been a constant source of encouragement and support. Throughout the course of many scientific discussions he has shown the utmost respect for the opinions and viewpoints of myself and other scientists. I would also like to thank Dr. Henry White for his initial prompting and assistance as our laboratory adopted the use of the modeling software that has allowed us to gain significant insights to several of the questions posed in this dissertation. I would also like to thank Dr. Steven Kern and Dr. Jindrich Kopecek for their participation as members of my supervisory committee.

One of the great joys of working on this project has the many helpful discussions with colleagues and mentors at the University of Utah, the U.S. Pharmacopeial Convention (USP), the University of Cincinnati, and wherever a fellow scientist was willing to aid in my pursuit of learning. In particular, I wish to express my sincere gratitude to my friend and mentor Dr. Erika Stippler at USP. Her help in translating obscure manuscripts from German to English and most importantly her constant

encouragement (“Just get it done Mark!’) has helped immensely. I am also thankful to Dr. Edward Trujillo and Dr. Jinsong Hao who provided timely help and training as I learned to use the computer software already mentioned. This list is by no means exhaustive, but for all those who have helped and encouraged me along the way, you know who you are and I thank you.

Words cannot express the deep feelings of gratitude that I feel towards my mother and father, who taught me to not only pursue a task until it is complete, but to make sure that the job is done well; toward Robyn, who has shown absolute support for me and our family – she has lived years of sacrificing her time and personal comfort to allow me to pursue my education; toward my children, to whom I am grateful for their constant and unconditional love; and finally, for all of the friends and family that have offered their prayers and encouragement throughout the years.

This research was supported, in part, by a pre-doctoral fellowship from the American Foundation for Pharmaceutical Education.

CHAPTER 1

INTRODUCTION

1.1 Transdermal Drug Delivery

Because of its large surface area and immediate access to the external environment, skin is a common site for the application of medicine and therapeutic treatments. The use of ointments, salves, poultices, and many other forms of topically applied treatments have been recorded for centuries. Drug substances administered to the patient via the skin can be divided into two main categories: (1) drugs intended to act locally, near the site of application or in the immediate and surrounding tissues; or (2) drugs that are intended to act systemically. Treatments that fall into the first category are referred to as topical treatments and will not be discussed. Treatments that fall into the second category are typically administered as part of a patch or delivery system and the entire finished product (including the excipients, adhesives, backing membrane, release membranes, etc.) is referred to as a transdermal drug delivery system (TDDS). In the last three decades TDDS's have become a commercially viable alternative to orally administered drug products. According to Prausnitz and Langer between the years of 1979 to 2002 a new TDDS was approved every 2.2 years with the rate increasing to one every 7.5 months in the period of 2005 – 2007.[1]

While the number of approved products has increased, the physicochemical characteristics of drug molecules that have been successfully integrated into a TDDS are relatively limited. The majority of drug molecules that have been targeted in the development of TDDS's have been low molecular weight (i.e., less than about 0.5 kDa), highly lipophilic, and have high potency. Some examples of these include scopolamine, nitroglycerin, clonidine, nicotine, oestradiol, oxybutinin, testosterone, and fentanyl.[2] In an effort to expand the pool of candidate molecules that may be considered for transdermal delivery a tremendous amount of research has focused on methods to enhance the transport of hydrophilic and ionic drug molecules across the skin. Methods used to enhance the transport of hydrophilic and ionized drugs across the skin include the following: chemical enhancers,[3-6] electroporation methods,[7-10] sonophoresis,[11-14] microneedles,[15-17] iontophoresis,[7,18-22] and various combinations of these methods.[23-28] In addition to interest in the systemic delivery of drugs, skin has also been utilized as a site for the non-invasive extraction of drugs and other therapeutically relevant molecules from the systemic circulation.[29-37]

1.2 Anatomy of Human Skin

Figure 1.1 shows an illustration of the basic features of mammalian skin. The skin is composed of three main layers: the epidermis, dermis and subcutis. The dermis and subcutis contain nerve endings, connective tissues, hair follicles, sweat glands and other organs and structures that may vary depending on the species and location on the body. An important feature of the dermis and subcutis that is common in all mammals is the

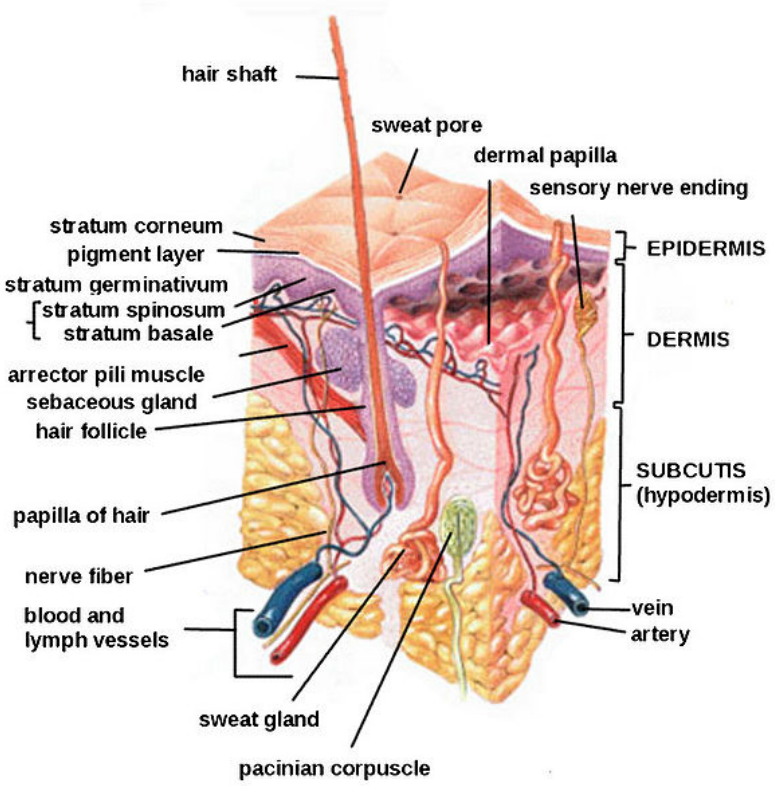

Figure 1.1. Diagram of human skin.[38] (Permission to copy granted under the terms of the GNU Free Documentation License and the Creative Commons Attribution-Share Alike license. See reference for website and license information.)

presence of capillary beds, arteries and veins that are responsible for the supply of blood flow to and from the skin. The capillary beds are the principle targets for the delivery of molecules that are intended for systemic circulation.

The outermost layer of the skin, the epidermis, is composed of two main layers, the stratum corneum and the stratum germinativum or viable epidermis. The viable epidermis contains an inner layer of living cells which are constantly dividing, differentiating, and migrating upward to replenish the outermost later, the stratum corneum. The primary function of the stratum corneum is to keep exogenous chemicals on the outside of the body while keeping moisture and other life-sustaining components inside the body. A brick and mortar model is typically used to describe the stratum corneum. Dead keratinized cells called corneocytes are represented by the bricks while multiple layers of intercellular lipids composed of ceramides, cholesterol and fatty acids are represented by the mortar between the bricks. Also included in the surface of the stratum corneum are pores for hair follicles and sweat ducts. Relative to the total surface area of the skin, the cross sectional area of these pores is low. While only about 10 – 25 μm thick, the stratum corneum is widely considered to be the principle barrier to the transport of charged and hydrophilic molecules.

1.3.1 Transport pathways of hydrophilic molecules

Figure 1.2 (adapted from Prausnitz et al.[2]) illustrates the possible locations of transport pathways available to hydrophilic permeants during transdermal drug delivery. Shown in Figure 1.2 are the intercellular pathway across the stratum corneum (site a), transport pathways through the hair follicle and associated sebaceous glands (site b),

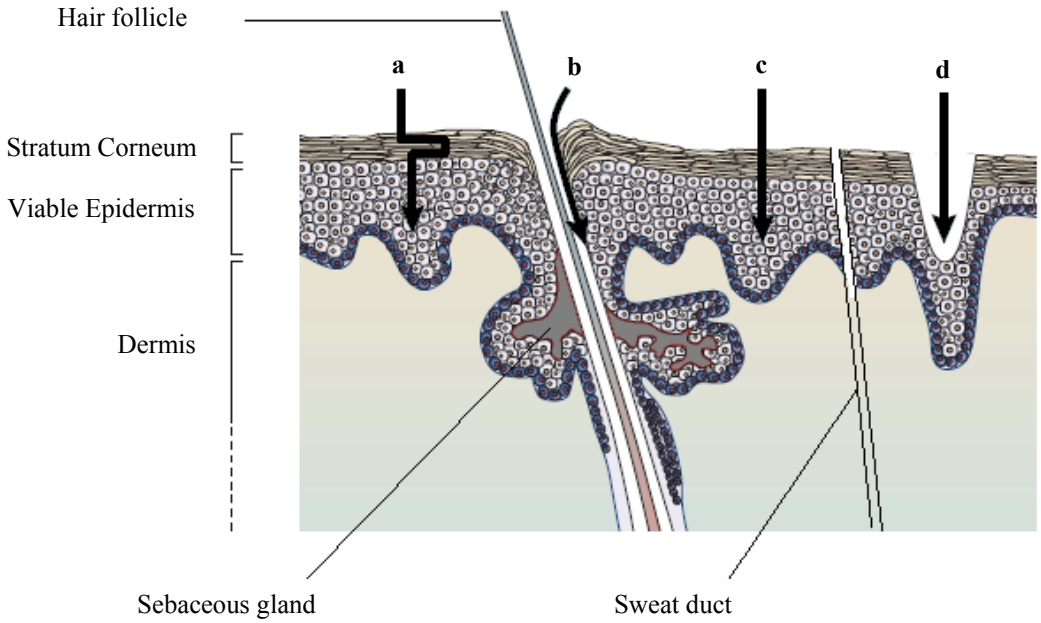

Figure 1.2. Schematic of transport pathways across the stratum corneum (adapted from Prausnitz et al.[2]). Transport of drug molecules through the pathways indicated in the diagram occur as a result of the following mechanisms: (a) diffusion across stratum corneum via intercellular lipid regions; (b) transport through hair follicles and sweat ducts; (c) transcellular transport due to disruption of lipid bilayers; and/or (d) physical alterations to the thickness and/or continuity of the epidermal layer.

transcellular pathways (site c) and pathways that result from disruption of the stratum corneum barrier integrity via microneedles or other physical methods (site d). Several authors have investigated the possible location of aqueous pore pathways in the stratum corneum (site a). Bodde et al. used mercuric chloride uptake experiments to show that aqueous pore pathways were primarily located in the intercellular lipids of the stratum corneum.[39] Sznitowska et al. also confirmed that the transport of hydrophilic permeants across the stratum corneum was likely to occur via aqueous pore pathways which resulted from hydrophilic lipid domains existing in the intercellular matrices between the corneocytes of the stratum corneum.[40] Bath et al. have shown that a significant amount of the electroosmotic and electrophoretic transport of molecules across hairless mouse skin (HMS) occurs via the hair follicle during low current density DC iontophoresis.[41,42] The pathways illustrated by sites c and d show pathways that appear to be associated with high voltage electroporation and physical disruption of the stratum corneum (i.e., the use of microneedles, tape stripping, laser ablation, etc.), respectively.[10,43]

1.3 Transdermal Iontophoresis

The application of an electrical current across the skin to enhance the transport of both ionic and nonionic permeants is known as transdermal iontophoresis. With only a small amount of electrical current applied to a few square centimeters, significant increases in the transport of permeants across the skin have been observed. Iontophoresis has been used for the treatment of hyperhidrosis,[44] for local anesthesia before dermatological procedures and/or injections,[45-47] for the diagnosis of cystic fibrosis,[48] and for the measurement of blood glucose levels.[49] One of the principle advantages of using

iontophoresis as a method to enhance the transport of permeants across the skin is the ability to control the flux by controlling the current density, polarity and duration of the applied electric field.

Figure 1.3 shows a schematic of an iontophoretic drug delivery system. In Figure 1.3 the electrodes used to apply the electric current are placed in the anodal and cathodal chamber and could be any number of different metal/halide combinations. The drug of choice shown in Figure 1.3 is a cationic drug. By applying an electric current across the skin a potential gradient is established from one side of the membrane to the other. The electric field enhances the transport of the cationic drug trough by three main mechanisms: electroporation, electrophoresis, and electroosmosis. These transport mechanisms have been investigated extensively throughout the last twenty five years in our laboratory and others.

1.3.1 Electroporation

Electroporation can be defined an increase in the permeability of a membrane due to the application of voltage across a membrane. When electroporation is used as an exclusive enhancement method, high voltage pulses are needed to induce large, transient, aqueous pores which increase the permeability of the skin to hydrophilic permeants;[10] however, even with low current densities and relatively low applied voltages some degree of electroporation will be observed. Srinivasan et al. concluded that for applied voltages as low at 125 mV, significant and irreversible damage was done to hairless mouse skin.[50]

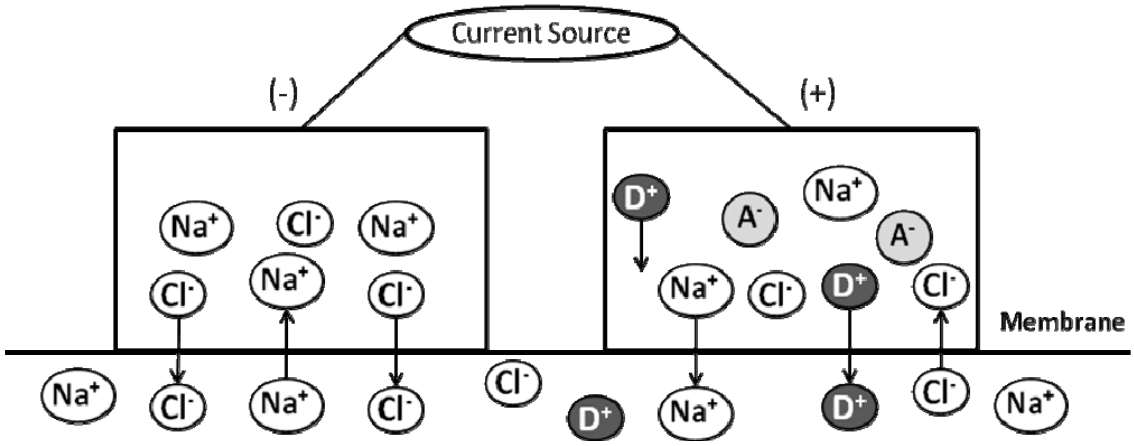

Figure 1.3. Schematic of a transdermal iontophoresis drug delivery system.

Evidence of electroporation can be seen in the observed decrease of the electrical resistance of the skin in response to the application of an electric current. Researchers in our laboratory and others have observed that along with a decrease in the electrical resistance of the skin, a corresponding increase in permeant transport is also typically observed.[8,43,51]

1.3.2 Electrophoresis

Electrophoresis refers to the transport of a charged molecule moving in response to an applied electric field. Cationic permeants move toward the negative electrode (referred to as the cathode in iontophoresis) and anionic permeants move toward the positive electrode (referred to as the anode). The electrophoretic flux of ionic permeants is related to their size and effective charge, i.e., their electromobility. Henchoz et al. have used capillary zone electrophoresis (CZE) to measure the effective electromobility of a series of peptides in order to predict the electrophoretic flux of the peptides during in vitro iontophoresis experiments.[52] Their research provides further evidence of the relationship between the iontophoretic flux of large, polyvalent and hydrophilic molecules and their electromobility. An obvious advantage of utilizing this mechanism as a means to enhance the transport of an ionic permeant across the skin lies in the ability to control the polarity, density and duration of the applied electric field to better control the magnitude and duration of permeant flux across the skin.

1.3.3 Electroosmosis

The role of electroosmosis in transdermal iontophoresis has been studied extensively by several authors.[22,53-55] Electroosmosis has also been investigated as a means of extracting nonionic and cationic permeants for diagnostic purposes from the interstitial fluid present in the dermis.[49,56,57] Electroosmosis refers to the field induced movement of solvent perpendicular to a charged surface. This mechanism comes about as a result of the net negative surface charge that exists in aqueous pore pathways of mammalian skin. A diffuse layer of cations, typically sodium ions, develops to neutralize the net negative charge at the surface of the pore. When an electric field is applied perpendicular to the pore surface, the cations in the diffuse layer begin to move toward the cathode causing the surrounding solvent molecules to also move in the same direction. Under normal experimental conditions, i.e., neutral pH and equal concentrations of ions on both sides of the membrane, the contribution of electroosmosis to the iontophoretic transport of small ionic permeants is typically small compared to electrophoresis.

1.4 Statement of the Problem

As described above, the mechanisms involved in the iontophoretic transport of ionic and nonionic permeants are well understood; however, most of the studies cited above have been conducted using a variety of membranes, theoretical models, and experimental conditions that may not represent (in terms of the concentrations of ions on either side of the membrane) a practical iontophoresis system designed for the delivery of large, polyvalent and hydrophilic molecules. One of the common experimental conditions

used for mechanistic in vitro iontophoresis studies is to ensure that equal concentrations of ions are present in solution on both sides of the membrane. Of course in practice, having the same composition in the external iontophoresis chamber compared to the internal compartment (i.e., the interstitial fluid of the dermis) is not very common. In many cases, in order to maximize the portion of the electrical current carried by the drug, the concentration of the ionized drug or charged peptide must be high in order to maximize the fraction of the electrical current carried by the ionic species of interest. From a mechanistic standpoint, this scenario, particularly in the case of peptides and high molecular weight polyelectrolytes, is not well understood. The purpose of this dissertation is to investigate low current density DC iontophoresis when the electrolyte solution in the external chamber contains varying concentrations of sodium polystyrene sulfonate (PSS; selected as a model, anionic polyelectrolyte). The specific aims of this research project are as follows:

1. Using the Nernst-Planck model as a theoretical framework, determine the effective pore radius (*Rp*) of hairless mouse skin (HMS) from iontophoresis experiments conducted under conditions with equal concentrations of ions on both sides of the membrane (baseline conditions) compared to *Rp* values obtained from iontophoresis experiments conducted with varying concentrations of sodium PSS in the cathodal chamber.
2. Determine the relative contributions from electrophoresis and electroosmosis to the total iontophoretic fluxes of ionic probe permeants under baseline conditions compared to experiments with varying concentrations of sodium PSS in the cathodal chamber.

3. Characterize the changes in the electrical properties of the HMS during iontophoresis experiments with varying concentrations of sodium PSS in the cathodal chamber and compare the results to those observed during iontophoresis experiments with equal concentrations of ions on both sides of the membrane.
4. Perform theoretical Nernst-Planck calculations in order to investigate changes in the following: potential gradient in the pore pathway, concentration profiles of probe permeants and current determining ions inside the membrane, and the relative contributions from the diffusive, electrophoretic, and electroosmotic flux components during iontophoresis experiments with sodium PSS in the cathodal chamber.

By completing the specific aims described above it is believed that researchers in the field of transdermal iontophoresis will be able to better understand the effect of having high concentrations of polyvalent ions in the external compartment of iontophoresis systems.

1.5 References

1. Prausnitz MR, Langer R 2008. Transdermal drug delivery. Nat Biotechnol 26(11):1261-1268.

2. Prausnitz MR, Mitragotri S, Langer R 2004. Current status and future potential of transdermal drug delivery. Nat Rev Drug Discov 3(2):115-124.

3. He N, Li SK, Suhonen TM, Warner KS, Higuchi WI 2003. Mechanistic study of alkyl azacycloheptanones as skin permeation enhancers by permeation and partition experiments with hairless mouse skin. J Pharm Sci 92(2):297-310.

4. He N, Warner KS, Higuchi WI, Li SK 2005. Model analysis of flux enhancement across hairless mouse skin induced by chemical permeation enhancers. Int J Pharm 297(1-2):9-21.

5. Kanikkannan N, Kandimalla K, Lamba SS, Singh M 2000. Structure-activity relationship of chemical penetration enhancers in transdermal drug delivery. Curr Med Chem 7(6):593-608.

6. Warner KS, Li SK, He N, Suhonen TM, Chantasart D, Bolikal D, Higuchi WI 2003. Structure-activity relationship for chemical skin permeation enhancers: probing the chemical microenvironment of the site of action. J Pharm Sci 92(6):1305-1322.

7. Higuchi WI, Li SK, Ghanem AH, Zhu H, Song Y 1999. Mechanistic aspects of iontophoresis in human epidermal membrane. J Control Release 62(1-2):13-23.

8. Prausnitz MR, Bose VG, Langer R, Weaver JC 1993. Electroporation of mammalian skin: a mechanism to enhance transdermal drug delivery. Proc Natl Acad Sci U S A 90(22):10504-10508.

9. Prausnitz MR, Lau BS, Milano CD, Conner S, Langer R, Weaver JC 1993. A quantitative study of electroporation showing a plateau in net molecular transport. Biophys J 65(1):414-422.

10. Weaver JC, Vaughan TE, Chizmadzhev Y 1999. Theory of electrical creation of aqueous pathways across skin transport barriers. Adv Drug Deliv Rev 35(1):21-39.

11. Tang H, Wang CC, Blankschtein D, Langer R 2002. An investigation of the role of cavitation in low-frequency ultrasound-mediated transdermal drug transport. Pharm Res 19(8):1160-1169.

12. Mitragotri S, Farrell J, Tang H, Terahara T, Kost J, Langer R 2000. Determination of threshold energy dose for ultrasound-induced transdermal drug transport. J Control Release 63(1-2):41-52.

13. Mitragotri S, Blankschtein D, Langer R 1995. Ultrasound-mediated transdermal protein delivery. Science 269(5225):850-853.

14. Levy D, Kost J, Meshulam Y, Langer R 1989. Effect of ultrasound on transdermal drug delivery to rats and guinea pigs. J Clin Invest 83(6):2074-2078.

15. Bramson J, Dayball K, Evelegh C, Wan YH, Page D, Smith A 2003. Enabling topical immunization via microporation: a novel method for pain-free and needle-free delivery of adenovirus-based vaccines. Gene Ther 10(3):251-260.

16. Lin W, Cormier M, Samiee A, Griffin A, Johnson B, Teng CL, Hardee GE, Daddona PE 2001. Transdermal delivery of antisense oligonucleotides with microprojection patch (Macroflux) technology. Pharm Res 18(12):1789-1793.

17. Mikszta JA, Alarcon JB, Brittingham JM, Sutter DE, Pettis RJ, Harvey NG 2002. Improved genetic immunization via micromechanical disruption of skin-barrier function and targeted epidermal delivery. Nat Med 8(4):415-419.

18. Banga AK. 1998. Electrically assisted transdermal and topical drug delivery. ed., London ; Bristol, PA: Taylor & Francis Group. p xi, 172 p.

19. Hoogstraate AJ, Srinivasan V, Sims SM, Higuchi WI 1994. Iontophoretic enhancement of peptides: behavior of leuprolide versus model permeants. J Controlled Release 31(1):41-47.

20. Pikal M 1990. Transport mechanisms in iontophoresis. I. A theoretical model for the effect of electroosmotic flow on flux enhancement in transdermal iontophoresis. Pharm Res 7(2):118-126.

21. Pikal M 1990. Transport mechanisms in iontophoresis. III. An experimental study of the contributions of electroosmotic flow and permeability change in transport of low and high molecular weight solutes. Pharm Res 7(3):222-229.

22. Pikal M, Shah S 1990. Transport mechanisms in iontophoresis. II. Electroosmotic flow and transference number measurements for hairless mouse skin. Pharm Res 7(3):213-221.

23. Johnson ME, Mitragotri S, Patel A, Blankschtein D, Langer R 1996. Synergistic effects of chemical enhancers and therapeutic ultrasound on transdermal drug delivery. J Pharm Sci 85(7):670-679.

24. Le L, Kost J, Mitragotri S 2000. Combined effect of low-frequency ultrasound and iontophoresis: applications for transdermal heparin delivery. Pharm Res 17(9):1151-1154.

25. Mitragotri S, Ray D, Farrell J, Tang H, Yu B, Kost J, Blankschtein D, Langer R 2000. Synergistic effect of low-frequency ultrasound and sodium lauryl sulfate on transdermal transport. J Pharm Sci 89(7):892-900.

26. Oh SY, Jeong SY, Park TG, Lee JH 1998. Enhanced transdermal delivery of AZT (Zidovudine) using iontophoresis and penetration enhancer. J Control Release 51(2-3):161-168.

27. Srinivasan V, Su MH, Higuchi WI, Behl CR 1990. Iontophoresis of polypeptides: effect of ethanol pretreatment of human skin. J Pharm Sci 79(7):588-591.

28. Zewert TE, Pliquett UF, Vanbever R, Langer R, Weaver JC 1999. Creation of transdermal pathways for macromolecule transport by skin electroporation and a low toxicity, pathway-enlarging molecule. Bioelectrochem Bioenerg 49(1):11-20.

29. Benjamin BF, Cornbleet T 1954. Cutaneous sodium and potassium determined by reverse iontophoresis. J Invest Dermatol 23(4):287-292.

30. Benjamin FB, Kempen R, Mulder AG, Ivy AC 1954. Sodium-potassium ratio of human skin as obtained by reverse iontophoresis. J Appl Physiol 6(7):401-407.

31. Rao G, Guy RH, Glikfeld P, LaCourse WR, Leung L, Tamada J, Potts RO, Azimi N 1995. Reverse iontophoresis: noninvasive glucose monitoring in vivo in humans. Pharm Res 12(12):1869-1873.

32. Leboulanger B, Fathi M, Guy RH, Delgado-Charro MB 2004. Reverse iontophoresis as a noninvasive tool for lithium monitoring and pharmacokinetic profiling. Pharm Res 21(7):1214-1222.

33. Wascotte V, Leboulanger B, Guy RH, Begona Delgado-Charro M 2005. Reverse iontophoresis of lithium: electrode formulation using a thermoreversible polymer. Eur J Pharm Biopharm 59(1):237-240.

34. Ching TS, Connolly P 2008. Simultaneous transdermal extraction of glucose and lactate from human subjects by reverse iontophoresis. Int J Nanomedicine 3(2):211-223.

35. Sieg A, Jeanneret F, Fathi M, Hochstrasser D, Rudaz S, Veuthey JL, Guy RH, Delgado-Charro MB 2009. Extraction of amino acids by reverse iontophoresis in vivo. Eur J Pharm Biopharm 72(1): 226-231.

36. Ching CT, Sun TP, Huang SH, Shieh HL, Chen CY 2010. A mediated glucose biosensor incorporated with reverse iontophoresis function for noninvasive glucose monitoring. Ann Biomed Eng 38(4):1548-1555.

37. Sun TP, Shieh HL, Ching CT, Yao YD, Huang SH, Liu CM, Liu WH, Chen CY 2010. Carbon nanotube composites for glucose biosensor incorporated with reverse iontophoresis function for noninvasive glucose monitoring. Int J Nanomedicine 5:343-349.

38. Telles DdS. 2010. ed. A complete diagram of the human skin. From website: http://en.wikipedia.org/wiki/File:HumanSkinDiagram.jpg (last accessed March 6, 2012).

39. Bodde HE, Vandenbrink I, Koerten HK, Dehaan FHN 1991. Visualization of in vitro percutaneous penetration of mercuric chloride; transport through intercellular space versus cellular uptake through desmosomes. J Control Release 15(3):227-236.

40. Sznitowska M, Janicki S, Williams AC 1998. Intracellular or intercellular localization of the polar pathway of penetration across stratum corneum. J Pharm Sci 87(9):1109-1114.

41. Bath BD, Scott ER, Phipps JB, White HS 2000. Scanning electrochemical microscopy of iontophoretic transport in hairless mouse skin. Analysis of the relative contributions of diffusion, migration, and electroosmosis to transport in hair follicles. J Pharm Sci 89(12):1537-1549.

42. Bath BD, White HS, Scott ER 2000. Visualization and analysis of electroosmotic flow in hairless mouse skin. Pharm Res 17(4):471-475.

43. Prausnitz MR 1999. A practical assessment of transdermal drug delivery by skin electroporation. Adv Drug Deliv Rev 35(1):61-76.

44. Holzle E, Alberti N 1987. Long-term efficacy and side effects of tap water iontophoresis of palmoplantar hyperhidrosis - the usefulness of home therapy. Dermatologica 175(3):126-135.

45. Maloney JM 1992. Local anesthesia obtained via iontophoresis as an aid to shave biopsy. Arch Dermatol 128(3):331-332.

46. Ashburn MA, Gauthier M, Love G, Basta S, Gaylord B, Kessler K 1997. Iontophoretic administration of 2% lidocaine HCl and 1:100,000 epinephrine in humans. Clin J Pain 13(1):22-26.

47. Rose JB, Galinkin JL, Jantzen EC, Chiavacci RM 2002. A study of lidocaine iontophoresis for pediatric venipuncture. Anesth Analg 94(4):867-871, table of contents.

48. Warwick WJ, Huang NN, Waring WW, Cherian AG, Brown I, Stejskal-Lorenz E, Yeung WH, Duhon G, Hill JG, Strominger D 1986. Evaluation of a cystic fibrosis screening system incorporating a miniature sweat stimulator and disposable chloride sensor. Clin Chem 32(5):850-853.

49. Tierney MJ, Tamada JA, Potts RO, Jovanovic L, Garg S 2001. Clinical evaluation of the GlucoWatch biographer: a continual, non-invasive glucose monitor for patients with diabetes. Biosens Bioelectron 16(9-12):621-629.

50. Srinivasan V, Higuchi WI, Su MH 1989. Baseline studies with the 4-electrode system - the effect of skin permeability increase and water transport on the flux of a model uncharged solute during iontophoresis. Journal of Controlled Release 10(2):157-165.

51. Zhu H, Peck KD, Li SK, Ghanem AH, Higuchi WI 2001. Quantification of pore induction in human epidermal membrane during iontophoresis: the importance of background electrolyte selection. J Pharm Sci 90(7):932-942.

52. Henchoz Y, Abla N, Veuthey JL, Carrupt PA 2009. A fast screening strategy for characterizing peptide delivery by transdermal iontophoresis. J Control Release 137(2):123-129.

53. Kim A, Green PG, Rao G, Guy RH 1993. Convective solvent flow across the skin during iontophoresis. Pharm Res 10(9):1315-1320.

54. Pikal M 2001. The role of electroosmotic flow in transdermal iontophoresis. Adv Drug Deliv Rev 46:281-305.

55. Yan G, Peck KD, Zhu H, Higuchi WI, Li SK 2005. Effects of electrophoresis and electroosmosis during alternating current iontophoresis across human epidermal membrane. J Pharm Sci 94(3):547-558.

56. Cazares-Delgadillo J, Naik A, Ganem-Rondero A, Quintanar-Guerrero D, Kalia YN 2007. Transdermal delivery of cytochrome C - a 12.4 kDa protein - across intact skin by constant-current iontophoresis. Pharm Res 24(7):1360-1368.

57. Ching CT, Chou TR, Sun TP, Huang SY, Shieh HL 2011. Simultaneous, noninvasive, and transdermal extraction of urea and homocysteine by reverse iontophoresis. Int J Nanomedicine 6:417-423.

CHAPTER 2

BASELINE STUDIES

2.1 Introduction

In the past two decades, the body of literature related to transdermal iontophoresis has grown greatly. We have believed that the development of effective iontophoretic drug delivery systems would be significantly aided by systematic mechanistic studies of transdermal iontophoresis. To this end, our laboratory and others have attempted to quantify the various transport mechanisms and membrane parameters that are expected to be important in the iontophoretic delivery and extraction of charged and nonionic molecules during constant direct current (DC) iontophoresis. Various authors have approached this problem using a variety of theoretical models, membranes, and probe permeants.[1-11] Pikal has reviewed data collected using both hairless mouse skin (HMS) and human skin in order to quantify the role of electroosmotic flow in transdermal iontophoresis.[12] Ruddy and Hadzija have applied hydrodynamic theory to model the transport of polyethylene glycols (with molecular weights ranging from 194 - 1382 Daltons) across hairless rat skin with reasonable success.[9] Many of the studies conducted in our laboratory have relied on the application of the modified Nernst-Planck model

Reprinted with permission from John Wiley & Sons (Hoboken, NJ): Liddell MR, Li SK, and Higuchi WI. Transport behavior of hairless mouse skin during constant current DC iontophoresis I: baseline studies. J Pharm Sci 100(4): 1475-1487

(MNP) to understand the effects of both electroosmosis and electrophoresis during constant current and/or constant voltage iontophoresis with heat-separated human cadaver skin [human epidermal membrane (HEM)].[13-15] As Luzardo-Alvarez et al. have shown, even a common parameter such as the transference number of the current carrying species can vary widely depending on the type of membrane and the experimental conditions used.[10] In all of the cases cited above, the experimental conditions, the model membrane employed, and theoretical models applied to the data have varied significantly.

In the present study, the nature of the transport pathways in HMS available to nonionic and ionic permeants was to be investigated with the MNP as a theoretical framework. The purpose of these experiments was to systematically study the transport behavior of a range of cationic, anionic and nonionic permeants under identical DC iontophoresis conditions, using the same model membrane, and using consistent theoretical models to treat the data. The following specific questions were to be addressed: (i) Are the pore radii (*Rp*) values obtained from constant current iontophoresis experiments with nonionic permeant pairs, cationic permeant pairs, and anionic permeant pairs different? (ii) Is the electrophoretic component of cation and anion fluxes similar for ions of comparable size when transported under the same iontophoretic conditions? (iii) Is HMS an adequate model for the HEM in mechanistic studies of iontophoretic transport?

To address the questions posed above the following experimental strategy was employed: (i) determine the diffusion coefficient and solute radius of each permeant; (ii) use the MNP model to calculate *Rp* from HMS flux data obtained with cationic, anionic, and nonionic permeant pairs; (iii) compare the fluxes of anionic and cationic permeants

of similar molecular size to test the extent of ion selectivity of the HMS during constant current DC iontophoresis; and (iv) use a synthetic ion exchange membrane to test the agreement between *Rp* estimates obtained using the hindrance factor for passive diffusion and electrophoresis versus *Rp* values obtained using the hindrance factor for permeants transported by convective solvent flow. The methodology and results of the present study were used as the baseline information in studies that were to be undertaken to investigate the effect of cotransport of oligomeric polyanions during reverse iontophoresis extraction of cationic and nonionic permeants.

2.2 Materials and Methods

2.2.1 Materials

All chemicals used were reagent grade and purchased from Sigma-Aldrich Company (St. Louis, MO), unless otherwise specified. [^{14}C] Sucrose, [^{14}C] salicylate (SA), [^{3}H] taurocholate (TC), [^{3}H] raffinose (Raff), [^{36}Cl] isotopic chlorine, [^{14}C] tetraethylammonium (TEA) bromide, and [^{3}H] tetraphenylphosphonium (TPP) bromide were obtained from American Radiolabeled Chemicals (St. Louis, MO). [^{14}C] Mannitol (Mann), [^{3}H] mannitol, and [^{22}Na] isotopic sodium were obtained from Perkin Elmer Life Sciences (Boston, MA). [^{14}C] Urea was obtained from Moravek Biochemicals (Brea, CA). Radiolabeled chemicals had an advertised purity of ≥ 98%. The purity of radiolabeled compounds was also verified using HPLC before and after selected experiments. Solutions were prepared using deionized water that had been purified using a Milli-Q® filtration system (resistivity > 10 MΩ·cm, Millipore Corp., Billerica, MA).

0.1 M ionic strength phosphate buffered saline (PBS: 0.013 M total phosphate; 0.077 M NaCl) with 50 mg/L gentamicin added as a preservative was prepared and adjusted to pH 7.4. Liquid silver paint was obtained from Ladd Research Industries (Williston, VT). Silver foil and other laboratory supplies were obtained from VWR Inc. (West Chester, PA).

2.2.2 Determination of permeant diffusion coefficient and molecular radius

An approach similar to that used by Peck et al. was employed to determine the diffusion coefficients.[16] The diffusion cell assembly consisted of a fritted glass disk (20 mm diameter, type F, Wilmad-Labglass, Buena, NJ) positioned between two rubber gaskets and sandwiched between the two halves of a side-by-side diffusion cell. The joint was sealed with laboratory film and both sides of the diffusion cell were filled with PBS. After equilibration in a circulating water bath overnight, the donor chamber solution was replaced with a premixed PBS solution containing trace amounts (0.25-1.0 μCi/mL) of the radioisotope or radiolabeled permeant of interest. A glass stopper modified to include a stopcock was then used to seal off the donor chamber, thus preventing pressure-induced solvent flow between the donor and receiver chambers. Constant stirring was maintained by magnetic stir bars placed in the chamber on each side of the fritted glass disk. The solution temperature was maintained at 37 ± 1ºC by a circulating water bath. Samples (1 mL) were taken from the receiver chamber and replaced with fresh PBS every hour for the first two hours of the experiment and every half hour for the remainder of the experiment. Donor solution samples (10 μL) were taken in triplicate at the beginning and end of each experiment to monitor for depletion of permeants from the donor chamber.

All samples were mixed with 10 mL of radio scintillation cocktail (Ultima Gold™, PerkinElmer, Waltham, MA) and were assayed by a liquid scintillation counter (Packard TriCarb™ Model 1900TR Liquid Scintillation Analyzer, PerkinElmer, Waltham, MA) using a dual counting protocol.

The diffusion coefficients were calculated using the expression

$$D_x = D_r \left(\frac{\frac{J_x}{C_x}}{\frac{J_r}{C_r}} \right) \tag{2.1}$$

where J_x and J_r are the experimental fluxes, C_x and C_r are the donor concentrations of the permeants, and the subscripts x and r refer to the permeant with an unknown diffusion coefficient and the reference permeant, respectively. Eq. 2.1 was used to calculate the diffusion coefficients for all of the permeants in the present study. Sucrose was used as a reference permeant (sucrose diffusion coefficient: 6.98×10^{-6} cm^2/s at 37°C).[17] The PBS buffer at ionic strength of 0.1 M served to essentially eliminate any diffusion potential effects upon the transport of an ionic permeant.[18]

The Stokes-Einstein radius, R_{SE}, was calculated using Eq. 2.2.

$$R_{SE} = \frac{kT}{6\pi\eta D} \tag{2.2}$$

where k, T, D, and η are the Boltzmann constant, absolute temperature, diffusion coefficient, and viscosity of the solution, respectively. Eq. 2.2 is only correct when the

diffusing solute is much larger than the solvent. For obtaining a more accurate estimate of the solute radius, *r*, Eq. 2.3 has been used when water is the solvent.[19]

$$R_{SE} = \left(1.5 \times \frac{R_w}{r} + \frac{r}{r + 2 \times R_w} \right)^{-1} \times r \qquad (2.3)$$

In Eq. 2.3 R_w is the radius of the water molecule and was assumed to be 1.5 Å. Eq. 2.3 was derived empirically based on the diffusion behavior of nonionic solutes. When the solute is an ion in water the situation with regard to the applicability of Eq. 2.3 would appear to be less clear. We have selected Eq. 2.3 both for its simplicity and so that the results obtained in the current investigations could be directly compared to results obtained previously in our laboratory.

2.2.3 Iontophoresis experiments with HMS

The use of HMS allowed for relatively good control over the following parameters that could have affected membrane permeability: age of the skin, source of the skin supply, and the environmental conditions during animal development. The ability to control the supply of membrane samples was critical for this type of systematic study. Experiments with HMS were conducted at low current densities so that the steady-state electrical resistance of the skin was similar from experiment to experiment and minimal changes in the membrane resistance were observed throughout the experiments.

After sacrificing the animals (female hairless mice, strain SKH1-hr, at least 12 weeks old from Charles River, Wilmington, MA; all experiments were reviewed and approved by the Institutional Animal Care and Use Committee at the University of Utah), sections of skin were removed from the abdomen. Except for the inclusion of a modified

stopper, the same diffusion cell configuration as that used for diffusion coefficient experiments was used for the HMS iontophoresis experiments. After sealing the HMS between the two halves of a side-by-side diffusion cell (volume of each half cell = 2 mL; diffusional area = 0.95 cm^2), the HMS was allowed to equilibrate with PBS on both sides of the membrane for 2 hours. To determine the initial resistance (R_{init}) of the HMS, 100 mV was applied across the HMS and the current was measured using a four-electrode potentiostat system (JAS Instrument Systems Inc., Salt Lake City, UT). Ohm's law was then used to calculate R_{init} of the membrane. After equilibration in PBS, only those HMS samples with $R_{init} \geq 25\ k\Omega \cdot cm^2$ were used for the iontophoresis experiments.

Figure 2.1 shows a schematic representation of the experimental setup used. At the end of the equilibration period (2 hours) a silver foil electrode (0.3 cm × 4 cm) and a painted Ag/AgCl electrode (sites c and f) was attached to the anode and cathode, respectively, of the constant current device (site a) and placed in opposite chambers. Painted Ag/AgCl electrodes were prepared by dipping strips of silver foil (0.3 cm × 4 cm) in a mixture of liquid silver paint mixed with crushed AgCl powder (1:1 weight ratio). The silver foil and Ag/AgCl electrodes were used to apply a constant current density of $0.11 \pm 0.01\ mA/cm^2$ to the HMS. The HMS was configured with the stratum corneum facing the cathode. This configuration was used for all of the iontophoresis experiments. Additional silver foil electrodes were placed on each side of the HMS (sites d and e) and connected to a voltmeter (site b). These additional electrodes were used to monitor the voltage drop across the membrane throughout the experiments. Constant stirring was maintained with magnetic stir bars on each side of the membrane. The entire diffusion

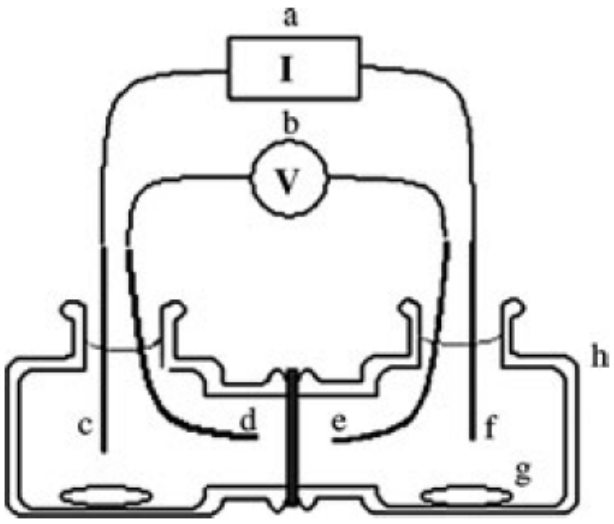

Figure 2.1. Schematic representation of iontophoresis experimental setup used for both HMS and synthetic ion exchange membrane experiments: (a) constant current power supply, (b) voltmeter used to monitor voltage drop across membrane, (c) silver foil electrode connected to anode of constant current device, (d and e) silver foil electrodes placed on each side of the membrane and connected to voltmeter, (f) painted Ag/AgCl electrode connected to cathode of constant current device, (g) magnetic stir bar used to maintain constant stirring, and (h) side-by-side diffusion cell.

cell assembly was submersed in a constant temperature water bath and the temperature of the bath was maintained at a temperature of 37 ± 1ºC via circulating water bath.

Experiments were conducted using nonionic permeant pairs, anionic permeant pairs, or cationic permeant pairs. Probe permeants were grouped in pairs in order to allow the calculation of the effective pore radius based on the ratio of the permeability coefficients of the probe permeants (see explanation below) and to maximize experimental efficiency. At the start of the experiment, the donor chamber was filled with pre-mixed solution of PBS containing trace amounts (0.25-1.0 μCi/mL) of the radioisotope and/or radiolabeled permeants. Samples were taken from the receiver chamber (1 mL every hour) and donor chamber (10 μL every two hours) for up to six hours. Receiver samples were replaced with an equivalent volume of fresh PBS. After analysis by liquid scintillation counting the following equation was used to calculate the experimental permeability coefficient, *P* or *P*-value,

$$P = \frac{1}{AC_D}\frac{\Delta Q}{\Delta t} \tag{2.4}$$

where A is the area of the membrane, C_D is the concentration of the donor solution, and $\Delta Q/\Delta t$ is the slope of the receiver cumulative amount vs. time plot (only the region where $R^2 > 0.98$ was used to calculate experimental *P*-values). Effectively, the permeability coefficient in this case is simply the flux normalized by the donor concentration. The linear region of the receiver cumulative amount vs. time plot generally consisted of data collected when $t \geq 120$ minutes.

2.2.4 Relating the experimental *P*-values to theory and calculating *Rp*

2.2.4.1 Nonionic permeants

When the transport of a nonionic molecule across a porous membrane is enhanced due to the presence of an electric field the following equation was used to relate the permeability coefficient, $P_{nonionic}$, to theory.[13]

$$P_{nonionic} = \frac{\varepsilon' HD}{h} \frac{Pe}{1 - \exp(-Pe)} \tag{2.5}$$

Here, for the sake of simplicity, it was assumed that there was a single uniform pore size and that pores were represented by a circular cylinder with a length much greater than the diameter. In Eq. 2.5, ε' is the effective porosity of the membrane (where $\varepsilon' = \varepsilon/\tau$, with ε defined as the fraction of the total membrane area available for permeant transport and τ is the tortuosity of the pathway), h is the membrane thickness, H is the hindrance factor for passive diffusion across the membrane, D is the diffusion coefficient of the permeant, and Pe is the Peclet number. $Pe = WvΔx/(HD)$, where W is the hindrance factor for convective solvent flow, v is the solvent flow velocity, and $Δx$ is the length of the pathway and is equal to the product of $\tau \times h$. The hindrance factors W and H are described by the following equations.

$$W = \frac{\Phi(2 - \Phi)K_s}{2K_t} \tag{2.6}$$

and

$$H = \frac{6\pi\Phi}{K_t} \tag{2.7}$$

In Eq. 2.6 and 2.7, $\Phi = (1-\lambda)^2$ and $\lambda = r/Rp$, where r is the solute radius (see Eq. 2.3) and Rp is the effective pore radius of the transport pathway. K_t and K_s are given by the following equations.

$$K_t = \frac{9}{4}\pi^2\sqrt{2}(1-\lambda)^{-5/2}[1+\sum_{n=1}^{2}a_n(1-\lambda)^n]+\sum_{n=0}^{4}a_{n+3}\lambda^n \tag{2.8}$$

$$K_s = \frac{9}{4}\pi^2\sqrt{2}(1-\lambda)^{-5/2}[1+\sum_{n=1}^{2}b_n(1-\lambda)^n]+\sum_{n=0}^{4}b_{n+3}\lambda^n \tag{2.9}$$

with a_1 = -1.2167; a_2 = 1.5336; a_3 = -22.5083; a_4 = -5.6117; a_5 = -0.3363; a_6 = -1.216; a_7 = 1.647; b_1 = 0.1167; b_2 = -0.0442; b_3 = 4.0180; b_4 = -3.9788; b_5 = -1.9215; b_6 = 4.392; and b_7 = 5.006. For Eqs. 2.6 – 2.9, W and H are valid when $0 \leq \lambda \leq 1$. The derivations of Eqs. 2.6 – 2.9 have been discussed extensively by Deen.[20]

Under convective flow limiting conditions (i.e., when $Pe \geq 4$ in Eq. 2.5), taking the ratio of permeability coefficients for two nonionic permeants results in the following equation (here and throughout the paper the subscripts 1 and 2 refer to the smaller and the larger of the two permeants, respectively).

$$\frac{P_{nonionic,1}}{P_{nonionic,2}} = \frac{W_1}{W_2} \tag{2.10}$$

Eq. 2.10 was used to calculate *Rp* using data from iontophoresis experiments with nonionic permeants by taking the ratio of experimental *P*-values and iteratively solving Eq. 2.10 for *Rp*. According to Eq. 2.6 and Eq. 2.10,

$$\lim_{Rp\to\infty} \frac{P_{nonionic,1}}{P_{nonionic,2}} = 1 \tag{2.11}$$

Eq. 2.11 shows the lower bound of *P*-value ratios when electroosmosis is the dominant transport mechanism. This theoretical limiting value is distinctly different from the limiting value of permeability coefficient ratios for passive and electrophoretically enhanced membrane transport (see below).

2.2.4.2 Ionic permeants

For ionic permeants, the corresponding expression for the permeability coefficient, P_{ion}, is

$$P_{ion} = \frac{\varepsilon' HD}{h} \frac{(K \pm Pe)}{1 - \exp[-(K \pm Pe)]} \tag{2.12}$$

where $K = zF\Delta\psi/(RT)$ and z is the charge of the permeant of interest, F is Faraday's constant, $\Delta\psi$ is the voltage drop across the membrane, R is the universal gas constant, and T is the temperature.[21,22] In Eq. 2.12, H is the hindrance factor taken to be the same for both passive diffusion and electrophoretic migration of ions. All of the experiments were designed such that the enhancement due to the applied field was in the same direction as passive diffusion along the concentration gradient. The sign of *Pe* in Eq. 2.12

depends on the direction of electroosmosis with respect to electrophoretic enhancement. When electroosmosis and electrophoresis are in opposite directions, the negative sign is used. When electrophoresis and electroosmosis are in the same direction, the positive sign is used. For HMS experiments conducted at pH 7.4, the positive sign and the negative sign are used for cations and for anions, respectively.

Under conditions where $\exp[-(K \pm Pe)] << 1.0$,

$$P_{ion} = \frac{\varepsilon' HD}{h}(K \pm Pe) \tag{2.13}$$

In such cases the permeability coefficient of an ionic permeant can be expressed as a linear combination of the electrophoretic portion, $P_{ion,ep}$, and the electroosmotic portion, $P_{ion,eo}$, of the total experimental permeability coefficient. In other words,

$$P_{ion} = P_{ion,ep} \pm P_{ion,eo} \tag{2.14}$$

Again, the sign of the electroosmotic portion of the total permeability depends on the direction of electroosmosis with respect to electrophoresis. As will be shown later, the condition $\exp[-(K \pm Pe)] << 1.0$ would seem to be appropriate for all situations encountered in the present study. According to Eq. 2.14, by substituting the appropriate experimentally deduced $P_{nonionic}$ value for $P_{ion,eo}$ we are able to calculate $P_{ion,ep}$ by simply adding or subtracting the $P_{nonionic}$ value from P_{ion} in Eq. 2.14. How this is done will be described in further detail in the Results section. Using this approach may overestimate to some degree the contribution from electroosmosis to the total permeability coefficient (P_{ion}) for the smallest permeants; however, this was not expected to be of concern in

those cases where $P_{ion,eo}$ was significant compared to $P_{ion,ep}$ (i.e., for the largest permeants, TC and TPP, where *Pe* was expected to be large). After accounting for the contribution from electroosmosis, pore sizes appropriate for ionic permeant pairs could be calculated using the following equation:

$$\frac{P_{ion,ep,1}}{P_{ion,ep,2}} = \frac{D_1 H_1}{D_2 H_2} \tag{2.15}$$

where *H* is given by Eq. 2.7. For permeants transported under only passive conditions, Eq. 2.15 may also be used by substituting the ratio of passive permeability coefficients for the left side of Eq. 2.15. According to Eq. 2.7 and Eq. 2.15,

$$\lim_{Rp\to\infty} \frac{P_{ion,ep,1}}{P_{ion,ep,2}} = \frac{D_1}{D_2} \tag{2.16}$$

Eq. 2.16 shows that for both passive transport and transport that is dominated by electrophoresis, the lower limit of permeability coefficient ratios for very large *Rp* is simply the ratio of diffusion coefficients.

2.2.5 Permeability experiments with a model synthetic membrane

A review of the literature has revealed no assurances that, for a given membrane, *Rp* values calculated using Eq. 2.6 and Eq. 2.10 with electroosmosis data and *Rp* values calculated using Eq. 2.7 and Eq. 2.15 with electrophoresis data should be essentially the same, especially when the permeant molecular radius becomes comparable to *Rp*. For this reason experiments were conducted with a model synthetic membrane to examine this

question. Permeability experiments were conducted with the synthetic cation exchange membrane IONAC™ MC-3470, a heterogeneous membrane with a net negative pore surface charge (cation exchanger) and low porosity, obtained from Sybron Chemicals (Birmingham, NJ). This synthetic membrane was not expected to exhibit any significant membrane alterations in the presence of an applied external electric field whereas considerable porosity and/or pore size changes in mammalian epidermal membranes are known to take place with increasing applied voltages during iontophoresis.[22,23]

Before each transport experiment, the membranes were washed with water and sonicated for ~15 minutes using a Bransonic ultrasonic cleaner (Branson Ultrasonic Corp., Danbury, CT). The membranes were then allowed to equilibrate in PBS for at least 12 hours before assembling the diffusion cell. The diffusion cell setup consisted of essentially the same arrangement as shown in Figure 2.1 with two of the synthetic membranes sandwiched between the two half-cells. After equilibration, the donor chamber was filled with a premixed PBS solution containing trace amounts of radiolabeled permeants (0.25-1.0 μCi/mL). [^{14}C] mannitol and [^{3}H] raffinose were selected for these experiments. Constant temperature (37 ± 1°C) and stirring were maintained throughout the experiments. During the iontophoresis experiment, a current density of 2.9 ± 0.3 mA/cm^2 was required to observe significant enhancement of nonionic molecules relative to passive diffusion. It was also necessary to replace the electrodes and solutions in the anodal and cathodal chambers every 45 minutes because of the electrochemical depletion of ions from the PBS solution. Passive permeability and constant current iontophoresis experiments were conducted on alternate days. The donor

and receiver chambers were rinsed repeatedly with fresh PBS between each of the experiments. Experimental permeability coefficients were calculated using Eq. 2.4.

Calculating the ratio of the iontophoretically enhanced permeability coefficients to passive permeability coefficients resulted in the enhancement factor, E, which was a single-valued function of Pe for nonionic permeants.

$$E = \frac{P_{nonionic}}{P_{nonionic,passive}} = \frac{Pe}{[1-\exp(-Pe)]} \tag{2.17}$$

The calculation of Pe was necessary to ensure that iontophoresis experiments were conducted under convective flow limiting conditions; it was then possible to determine Rp of the synthetic ion exchange membrane based on the ratio of the iontophoretic permeability coefficients for mannitol and raffinose and Eq. 2.10. Under passive conditions Rp was determined using the ratio of experimental permeability coefficients and Eq. 2.15 (i.e., the right hand side of Eq. 2.15 was equated to the ratio of the passive permeability coefficients).

2.3 Results

2.3.1 Measurement of diffusion coefficients

Diffusion coefficients obtained from the fritted glass disk diffusion experiments are shown in Table 2.1. Also shown for each permeant is the nominal charge, molecular weight, Stokes-Einstein radius (calculated using Eq. 2.2), hydrodynamic radius (calculated using Eq. 2.3), and diffusion coefficients taken from the literature. The use of Eq. 2.3 resulted in the largest percentage differences between R_{SE} and r when applied to

Table 2.1. Summary of nominal charge, MW, experimentally determined diffusion coefficients, Stokes-Einstein radius, equivalent solute radius, and literature diffusion coefficients for probe permeants considered in this study.

Permeant	z	MW	D (10^{-6} cm^2/s)[a]	R_{SE} (Å)	r (Å)	D from Literature (10^{-6} cm^2/s)
^{36}Cl	-1	36	27± 1	1.2	1.9	27.2 [b,c]
^{22}Na	+1	23	17.6 ± 0.9	1.9	2.5	18.1 [b,c]
[^{14}C]-Urea	0	60	18 ± 1	1.8	2.5	18.5 [b,d]
[^{14}C]-Salicylate	-1	137	12.7 ± 0.4	2.6	3.2	12.8 [b,c]
[^{14}C]-TEA	+1	130	11.8 ± 0.7	2.8	3.4	11.6 [b,c]
[^{14}C]-Mannitol	0	182	8.9 ± 0.1	3.7	4.1	8.6 [b,d]
[^{3}H]-Taurocholate	-1	516	5.7 ± 0.1	5.8	6.1	N/A
[^{3}H]-TPP	+1	340	4.9 ± 0.3	6.8	6.9	N/A
[^{3}H]-Raffinose	0	505	5.8 ± 0.4	5.7	5.9	5.7 [b,d]

[a] Mean experimental diffusion coefficients ± SD, for $n \geq 3$ experiments.
[b] Values have been corrected for viscosity and temperature changes.
[c] Diffusion coefficient was calculated using the relationship $zFD = \mu R_{gas}T$, where μ is the electromobility at infinite dilution, z is the valence, R_{gas} is the gas constant, T is the temperature, and F is Faraday's constant. [24]
[d] Literature diffusion coefficients for nonionic molecules were measured in water and extrapolated to infinite dilution.[25]

the smallest permeants. For example, using Eq. 2.3 to calculate the radius, *r*, of the chloride ion resulted in a radius that was 58% larger than the calculated value of R_{SE}; however, applying the same correction to the TPP ion resulted in only a 2% increase in *r* relative to R_{SE}. These results demonstrate, as expected, that Eq. 2.2 was most accurate when the permeant molecular size was much larger than that of the solvent. While the use of Eq. 2.3 allows for direct comparison with previous data from our laboratory, using this equation to correct for the radius of ions may not be appropriate because the equation only accounts for steric interactions with the surrounding solvent molecules. The diffusion coefficients determined for ions and uncharged polar molecules were in close agreement with values that were used in previous studies conducted in our laboratory.[14,21]

2.3.2 HMS iontophoresis experiments with ionic permeants

The results of HMS iontophoresis experiments using ionic permeants as the probe permeants are summarized in Table 2.2 (anionic permeant pairs) and Table 2.3 (cationic permeant pairs). The data are the initial resistance (R_{init}) of the HMS, the steady-state resistance of the HMS during iontophoresis ($R_{s\text{-}s}$), the experimental permeability coefficients (P_{ion}), the electrophoretic portion of the total permeability coefficient($P_{ion,ep}$), and the effective pore radius, *Rp,* calculated from the mean of $P_{ion,ep}$ ratios and Eq. 2.15. $P_{ion,ep}$ values were calculated using Eq. 2.14. The value of $P_{ion,eo}$ for each ion was estimated by plotting $P_{nonionic}$ values of the nonionic permeants (taken from Table 2.4) versus their respective diffusion coefficients and then using the resulting best fit line of the plot to obtain $P_{ion,eo}$ by interpolating for the diffusion coefficient value of the ionic

Table 2.2. Summary of data from experiments with anionic permeant pairs.

Permeant Pair	R_{init} ($k\Omega \cdot cm^2$)	R_{s-s} ($k\Omega \cdot cm^2$)	$P_{ion,1}$ (10^{-7} cm/s)	$P_{ion,2}$ (10^{-7} cm/s)	$P_{ion,ep,1}$ (10^{-7} cm/s)	$P_{ion,ep,2}$ (10^{-7} cm/s)	Ratio [a]	*Rp* (Å)[b]
^{36}Cl:Sal	181 ± 137	7 ± 2	51 ± 3	21 ± 1	56 ± 3	23 ± 1	2.45 (2.37, 2.52)	49 (41, 67)
^{36}Cl:TC	110 ± 76	6 ± 1	49 ± 4	2.8 ± 0.4	55 ± 4	3.8 ± 0.3	14.5 (13.3, 15.6)	22 (21, 24)
Sal:TC	104 ± 28	7 ± 1	23 ± 1	3.5 ± 0.4	25 ± 1	4.6 ± 0.4	5.5 (4.9, 6.2)	20 (18, 22)

Data points represent mean ± SD for $n \geq 6$ experiments. The subscripts 1 and 2 represent the smaller and larger of the two permeants, respectively.

[a] Mean of $P_{ion,ep,1}/P_{ion,ep,2}$ from individual experiments. The upper and lower limits of the 95% CI are shown in parentheses.
[b] *Rp* calculated using Eq. 2.15 and the mean value of $P_{ion,ep,1}/P_{ion,ep,2}$. Upper and lower limits shown in parenthesis were calculated based on the 95% confidence interval (CI) of mean values.

Table 2.3. Summary of data from experiments with cationic permeant pairs.

Permeant Pair	R_{init} ($k\Omega \cdot cm^2$)	R_{s-s} ($k\Omega \cdot cm^2$)	$P_{ion,1}$ (10^{-7} cm/s)	$P_{ion,2}$ (10^{-7} cm/s)	$P_{ion,ep,1}$ (10^{-7} cm/s)	$P_{ion,ep,2}$ (10^{-7} cm/s)	Ratio [a]	*Rp* (Å)[b]
^{22}Na:TEA	132 ± 88	5 ± 1	44 ± 2	24 ± 2	41± 2	22 ± 2	1.9 (1.7, 2.0)	19 (16, 33)
^{22}Na:TPP	100 ± 60	7 ± 1	49 ± 4	6.4 ± 1.1	48 ± 4	5.9 ± 1.1	8.4 (6.6, 10.2)	30 (25, 40)
TEA:TPP	110 ± 31	5 ± 1	27 ± 6	5.8 ± 2.2	30 ± 7	5.3 ± 2.2	6.3 (3.4, 9.2)	24 (19, 55)

Data points represent mean ± SD for $n \geq 5$ experiments. The subscripts 1 and 2 represent the smaller and larger of the two permeants, respectively.

[a] Mean of $P_{ionep,1}/P_{ion,ep,2}$ from individual experiments. The upper and lower limits of the 95% CI are shown in parentheses.
[b] *Rp* calculated using Eq. 2.15 and the mean value of $P_{ion,ep,1}/P_{ion,ep,2}$. Upper and lower limits shown in parenthesis were calculated based on the 95% CI of mean $P_{ion,ep,1}/P_{ion,ep,2}$ values.

Table 2.4. Summary of data from experiments with nonionic permeants.

Permeant Pair	R_{init} ($k\Omega \cdot cm^2$)	R_{s-s} ($k\Omega \cdot cm^2$)	$P_{noninoic,1}$ (10^{-7} cm/s)	$P_{nonionic,2}$ (10^{-7} cm/s)	Ratio [a]	*Rp* (Å)[b]	*Rp* (Å)[c]
Urea:Mann	92 ± 31	7 ± 1	3.1 ± 0.5	1.2 ± 0.2	2.7 (2.5, 2.9)	6.7 (6.5, 7.0)	6.8 (6.6, 7.0)
Urea:Raff	105 ± 63	6 ± 1	3.9 ± 0.6	1.2 ± 0.2	3.4 (2.8, 3.9)	9.9 (9.4, 10.6)	10.3 (9.8, 11.2)
Mann:Raff	73 ± 51	6 ± 1	1.9 ± 0.5	1.3 ± 0.3	1.5 (1.4, 1.6)	13.4 (12.5, 14.7)	14.7 (13.4, 16.6)

Data points represent mean ± SD for $n \geq 6$ experiments. The subscripts 1 and 2 represent the smaller and larger of the two permeants, respectively.

[a] Mean of $P_{nonionic,1}/P_{nonionic,2}$ from individual experiments. The upper and lower limits of the 95% CI are shown in parentheses.
[b] *Rp* calculated using Eq. 2.10 and mean value of $P_{nonionic,1}/P_{nonionic,2}$. Upper and lower limits shown in parenthesis were calculated based on the 95% CI of mean values.
[c] *Rp* calculated using Eq. 2.20 and *Pe* values of 2.2, 2.5, and 5.7 for urea, mannitol, and raffinose, respectively. Upper and lower limits shown in parenthesis were calculated based on the 95% confidence CI of mean values.

permeant. The data in parentheses (the last column of Table 2.2 and Table 2.3) represent the lower and upper limits of *Rp* estimates which were calculated using the upper and lower limits of the 95% confidence interval (CI) of mean $P_{ion,ep}$ ratios.

Figure 2.2 shows a plot of $P_{ion,ep}$ values for cations and anions versus their respective diffusion coefficients. The two lines drawn through the data are best-fit lines illustrating the differences in $P_{ion,ep}$ values for anions versus cations. Figure 2.2 showed that $P_{ion,ep}$ values for cations were typically higher compared with $P_{ion,ep}$ for anions.

2.3.3 HMS iontophoresis experiments with nonionic permeants

The results of HMS iontophoresis experiments with the nonionic permeants are summarized in Table 2.4. The data are the initial HMS resistance (R_{init}), the steady-state resistance of HMS during iontophoresis ($R_{s\text{-}s}$), the experimental permeability coefficients of urea, mannitol, and raffinose ($P_{nonionic}$; calculated using Eq. 2.4), the mean permeability coefficient ratio ($P_{nonionic,1}/P_{nonionic,2}$) and the effective pore radius calculated using the mean permeability coefficient ratio and Eq. 2.10 under the assumption of convective flow limiting conditions (i.e., for $Pe > 4$). Data in parenthesis represent the lower and upper limits of *Rp* estimates which have been calculated based on the upper and lower limits of the 95% CI of mean $P_{nonionic}$ ratios.

To examine the convective flow limit assumption used in the calculation of *Rp* for nonionic permeants, the following method was used to estimate *Pe* for each of the nonionic permeants. The permeability coefficient of a hypothetical ion, P°_{ion}, having a diffusion coefficient equal to that of the nonionic permeant may be represented by a line drawn midway between the two regression lines in Figure 2.2. The hypothetical ion is

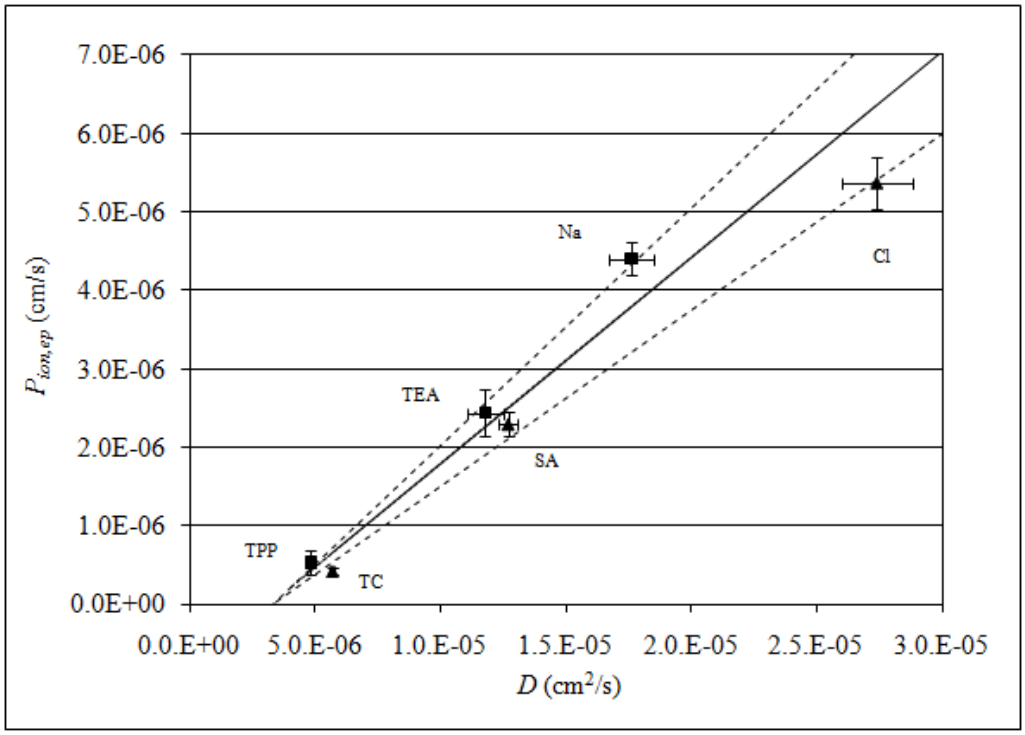

Figure 2.2. Electrophoretic portion of permeability coefficients, $P_{ion,ep}$, plotted against their respective diffusion coefficients for anions and cations: (▲) anionic permeants, (■) cationic permeants, Y-error bars represent the standard deviation (SD) of mean values, and X-error bars represent the SD of experimentally determined diffusion coefficients. Dashed lines represent the best-fit lines for anionic and cationic permeants. The solid line represents the permeability coefficient of the hypothetical ion where the difference between $P_{ion,ep}$ for a positive and negative ion has been eliminated.

defined as that for which the difference between $P_{ion,ep}$ for a positive ion and a negative ion with the same diffusion coefficient has been arbitrarily eliminated. As discussed later, this difference likely arises from the difference in the pore microenvironment partitioning tendency between a negative ion and a positive ion of the same size. On the basis of the mean value of the measured applied voltage during iontophoresis experiments, the mean value of K was 25.4 for |z| = 1. From Eq. 2.12, under the assumption that $(K + Pe) > 4$ and $K >> Pe$, we may write the relation for $P_{ion,passive}$ for the hypothetical ion,

$$P_{ion,passive} = \frac{P^{\circ}_{ion}}{K} \tag{2.18}$$

Since P°_{ion} was obtained for an ion with the same diffusion coefficient as that of the nonionic permeant, it is reasonable to assume that $P_{ion,passive} \approx P_{nonionic,passive}$. With such an estimate for $P_{nonionic,passive}$, it is possible to calculate the value of Pe for each of the nonionic permeants using Eq. 2.17 and the $P_{nonionic}$ values. The value of Pe can then be used in Eq. 2.19 to calculate a second estimate of $P_{nonionic,passive}$.

$$P_{nonionic,passive} = P_{ion,passive} = \frac{P^{\circ}_{ion}}{(K + Pe)} \tag{2.19}$$

Using Eq. 2.19 eliminates the need for the assumption that $K >> Pe$. Eq. 2.19 was then used iteratively, along with Eq. 2.17, until estimates of Pe converged to a single value. Using Eq. 2.19 we obtained Pe estimates of 2.2, 2.5, and 5.7 for urea, mannitol and raffinose, respectively. As expected, Pe decreased as the size of the permeant decreased.

By this analysis, it is also apparent that the convective flow limit assumption, *Pe* > *4*, would be true only in the case of the largest nonionic permeant, raffinose.

To understand the effect of assuming convective flow limiting conditions in the calculation of *Rp* for nonionic permeants, *Rp* was also calculated using Eq. 2.20, which allowed for the consideration of *Pe*.

$$\frac{P_{nonionic,1}}{P_{nonionic,2}} = \frac{W_1}{W_2}\frac{\left[1-\exp(-Pe_2)\right]}{\left[1-\exp(-Pe_1)\right]} \tag{2.20}$$

Rp estimates of 6.8, 10.3, and 14.8 Å were obtained based on the mean of urea:mannitol, urea:raffinose, and mannitol:raffinose permeability coefficient ratios, respectively. The largest difference observed in values of *Rp* calculated with and without assuming convective flow limiting conditions was observed for the mannitol:raffinose pair and was around 1.5 Å. For the other two pairs, urea:mannitol and urea:raffinose, using *Pe* in the calculation of *Rp* made little difference in the final results. The results of calculating *Rp* using Eq. 2.20 are shown in the final column of Table 2.4.

2.3.4 Synthetic membrane permeability experiments

The results of permeability experiments with the synthetic ion exchange membrane are summarized in Table 2.5. Passive and enhanced permeability coefficients are shown for the two diffusion cells. Experimental *Pe* values were calculated using Eq. 2.17. The mean ± SD of *Pe* was 5 ± 1 and 94 ± 11 for mannitol and raffinose, respectively. Given the experimental *Pe* values, it is clear that the iontophoretically enhanced transport experiments took place under convective flow limiting conditions. *Rp*

Table 2.5. Summary of synthetic ion exchange membrane data with mannitol (mann) and raffinose (raff) as the probe permeant pair.

Diffusion Cell	Condition	P_{mann} (10^{-7} cm/s)	Pe_{mann}	P_{raff} (10^{-8} cm/s)	Pe_{raff}
1	Passive	2.1 ± 0.2	N/A	1.1 ± 0.2	N/A
	3 mA/cm^2	9.9 ± 0.7	5	98.8 ± 7.2	90
2	Passive	2.4 ± 0.1	N/A	1.3 ± 0.3	N/A
	3 mA/cm^2	12.6 ± 1.9	5	126.2 ± 19.1	99

Permeability coefficients shown represent mean ± SD for $n \geq 3$ experiments. *Pe* was calculated using Eq. 2.17.

was calculated for experiments conducted under iontophoretic conditions using the ratio of experimental permeability coefficients and Eq. 2.10. *Rp* was also calculated for experiments conducted under passive conditions using the ratio of experimental *P*-values and Eq. 2.15. The mean *Rp* value (mean ± SD; n = 14 experiments) calculated for experiments where electroosmosis is the dominant driving force was 7.2 ± 0.2 Å. The mean *Rp* value (mean ± SD; n = 12 experiments) calculated for experiments under passive diffusion conditions was 7.0 ± 0.3 Å. The results of synthetic membrane experiments demonstrated that using *W* (Eqs. 2.6 and 2.10) and *H* (Eqs. 2.7 and 2.15) resulted in mean *Rp* values that were comparable.

The steric partition function (Φ in Eq. 2.6 and Eq. 2.7) has also been used successfully in previous studies to predict nonionic solute rejection in nanofiltration membranes.[26,27] However, much of the work done with nanofiltration membranes has focused on the rejection of solutes under conditions where high pressure was used to induce solvent flow across the membrane. The results of our experiments with synthetic ion exchange membranes demonstrated that *W* and *H* (Eq. 2.6 and Eq. 2.7, respectively) gave consistent results under conditions in which solvent flow was induced via an applied electrical field.

2.4 Discussion

2.4.1 Electrical properties of HMS

Although R_{init} values varied widely for HMS samples in these experiments, $R_{s\text{-}s}$ values showed noticeably lower variability (see Tables 2.2 – 2.4). Reduced variability

was reflected in the lower percent relative standard deviations (%RSD) for mean $R_{s\text{-}s}$ values, compared to R_{init} values. In some cases the %RSD of $R_{s\text{-}s}$ values decreased up to threefold compared to the %RSD of R_{init} values. One-way analysis of variance (ANOVA) was used to compare mean $R_{s\text{-}s}$ values from experiments conducted with each of the permeant pairs. Mean $R_{s\text{-}s}$ values were significantly different ($p < 0.05$) from each other for sets of experiments conducted using different permeant pairs. Differences among mean $R_{s\text{-}s}$ values demonstrate that, even at low current densities and using HMS samples from the same source, maintaining constant electrical conductance properties of HMS samples was difficult.

Although the trend of decreasing variability for $R_{s\text{-}s}$ values compared with R_{init} values was similar for HMS and HEM, HMS showed a lower degree of variability in $R_{s\text{-}s}$ values. Previous studies conducted by Zhu et al. have shown $R_{s\text{-}s}$ values of HEM varied from 6 to 14 $k\Omega \cdot cm^2$ under conditions of low current density (0.13 mA/cm^2) DC iontophoresis experiments.[15] For all of the iontophoresis experiments in the current study, mean $R_{s\text{-}s}$ values varied from 4.6 to 7.6 $k\Omega \cdot cm^2$. To maintain consistent $R_{s\text{-}s}$ values while using HEM as the model membrane, Zhu et al. proposed using an applied alternating current to maintain control of $R_{s\text{-}s}$ values.[15] This approach was not used in the present studies.

2.4.2 Transport behavior of ions and nonionic permeants across HMS

With the exception of TC and TPP, electroosmosis did not seem to play an important role in the transport of small ionic permeants. Evidence for this was seen by comparing $P_{ion,ep}$ values for ions (Tables 2.2 and 2.3) to the $P_{nonionic}$ values (Table 2.4). In

contrast, for the largest ionic permeants (TC and TPP) the contribution of electroosmosis to the total permeability coefficient, P_{ion}, was relatively large (compare, for example, $P_{ion,ep}$ values of TC and TPP with $P_{nonionic}$ of raffinose). Calculated *Pe* values for the nonionic permeants were also consistent with the decreasing importance of electroosmosis observed for the small permeants.

In addition to similarities in the electrical properties of HMS and HEM, the iontophoretic permeability coefficients of mannitol and TEA were also similar for the two membranes. Within the scatter of the data, mannitol permeability coefficients for HMS overlap with those observed for HEM under similar experimental conditions ($1.5\times10^{-7} \pm 0.8\times10^{-7}$ cm/s with HMS compared to $2.1\times10^{-7} \pm 1.0\times10^{-7}$ cm/s using HEM as the model membrane[15]). The permeability coefficients of TEA obtained from iontophoresis experiments with HMS were also comparable to those obtained using HEM as the model membrane under similar iontophoresis conditions ($2.5\times10^{-6} \pm 0.5\times10^{-6}$ cm/s with HMS compared to $4.7\times10^{-6} \pm 1.7\times10^{-6}$ cm/s using HEM as the model membrane; n = 8; unpublished results).

Further evidence of the similarities between HMS and other mammalian epidermal membranes is seen in the calculated effective porosity value. Using the experimental value of *K* (mean value of 25.4), the *Rp* value calculated for each of the ionic permeant pairs, an *h* value of 15 μm (values of *h* reported in the literature range from 10 – 25 μm[4,28,29]), the *Pe* value calculated for the nonionic permeant with a similar size to that of the ionic probe permeant, and the value of *D*, values of ε' were calculated using Eq. 2.12 for each of the ionic probe permeants. Calculated values of ε' ranged from

1.4×10^{-5} to 2.6×10^{-5}. Mitragotri has also reported a porosity value of 2×10^{-5} for porcine skin having an electrical resistance of approximately 100 $k\Omega\cdot cm^2$.[29] Pikal reported a value of 6.9×10^{-5} for the total porosity of HMS.[4] Given the differences in the membrane types, experimental details, and theoretical models used to calculate the porosity values, it is quite remarkable that all of the porosity values are within two or threefold of each other.

2.4.3 Effective pore radius values

According to the theory of electroosmosis, enhanced transport of nonionic molecules during transdermal iontophoresis at neutral pH is dominated by pore pathways with a negative surface charge; therefore, *Rp* values obtained from experiments with nonionic permeants were expected to reflect the size of negatively charged pore pathways.[12] The *Rp* values obtained using charged permeants were expected to reflect the radius of both charged and uncharged pore pathways. In addition to differences among *Rp* estimates obtained using charged permeants compared to *Rp* obtained from experiments with nonionic molecules, there also appears to be a size distribution among *Rp* values obtained from experiments with nonionic permeant pairs.

Except for the *Rp* value of 49 Å calculated for the Cl:SA pair, the majority of *Rp* values calculated based on the mean permeability coefficient ratios for ionic permeants were in the range of 19 – 28 Å (see final columns of Tables 2.2 and 2.3). To show that the large *Rp* estimates obtained from the Cl:SA pair were not a result of using the corrected solute radius (*r*) to calculate *Rp* instead of the Stokes-Einstein radius (R_{SE}), R_{SE}

was also used with Eq. 2.15 to calculate values of *Rp*. Using R_{SE} in the place of *r* to calculate values of *Rp* made little difference in the results.

One possible explanation for the large values of *Rp* obtained for the Cl:SA pair can be seen in the theoretical plots shown in Figure 2.3. The calculation of *Rp* for the smallest permeant pairs was much more sensitive to variability in the permeability coefficient ratios compared to calculations using the ratio of permeability coefficients for permeant pairs with larger mean solute radii. According to Figure 2.3, in the *Rp* region of interest (i.e., 17 – 30 Å), small changes in the Cl:SA and Na:TEA permeability coefficient ratios resulted in large changes in the calculated *Rp* values. In the case of the Cl:SA pair, a 15% decrease in the permeability coefficient ratio could result in an increase of almost 30 Å in the calculated value of *Rp*.

Although small, the differences in the $P_{ion,ep}$ and *Rp* values between the cationic and the anionic permeants are consistent with the interpretation that the negatively charged pores of the membrane having pore radii and an electrical double layer thickness on the same order of magnitude as the radius of the diffusing ionic permeant exhibited preferential selectivity for the cationic permeants. Munch et al. found that in order to model the transport of large negatively charged macromolecules in pores with a negatively charged surface it was necessary to treat the electrical double layer as a static barrier for synthetic membranes having a negative surface charge where the interaction between the pore wall and the permeant was repulsive.[30] Although differences in the *Rp* values in Tables 2.2 and 2.3 were within the scatter of the data, the upper limit of the range of *Rp* values calculated for the cationic permeant pairs was generally larger (with the exception of the Cl:SA pair) than the upper limit for the anionic permeant pairs. This

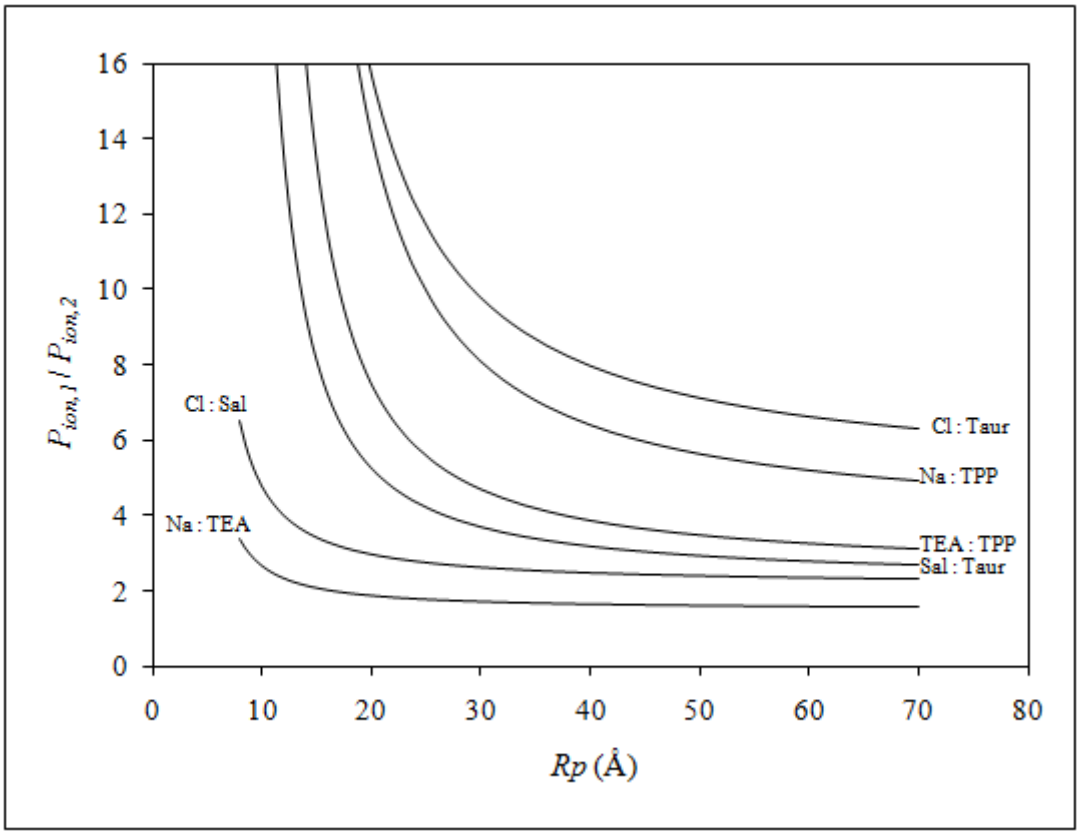

Figure 2.3. Plot of the theoretical permeability coefficient ratio ($P_{ion,1}/P_{ion,2}$) versus the effective pore radius (Rp) for charged permeant pairs (calculated using Eq. 2.15).

trend, along with the differences of $P_{ion,ep}$ between cations and anions (see Figure 2.2), is consistent with the transport behavior observed by Munch et al. *Rp* values obtained from experiments with nonionic permeants were consistently lower than those obtained from experiments with ionic molecules. Flux experiments with the model synthetic membrane indicated that, for membranes having relatively uniform transport pathways, using *W* (Eq. 2.6 and Eq. 2.10) and *H* (Eq. 2.7 and Eq. 2.15) to obtain *Rp* should have resulted in similar values.

There also appeared to be a distribution of *Rp* values observed in experiments with the nonionic permeants. Notice that *Rp* estimates obtained from the urea:mannitol pair resulted in the smallest *Rp* values while using the urea:raffinose and mannitol:raffinose pairs to calculate *Rp* resulted in larger *Rp* estimates. This trend suggests that a distribution of pore radii may exist within the population of the negatively charged pores in HMS. Differences observed in *Rp* values calculated for nonionic and ionic permeants are consistent with earlier work reviewed by Pikal.[12] Pikal reported that it was necessary to include multiple pore pathways having positive, negative, and zero surface charge characteristics in order to model data obtained from electrical conductivity experiments with HMS. In addition to considering a model requiring pores with different surface charge characteristics, Pikal also suggested that each type of pore had a different pore radius. Although *Rp* estimates calculated in the present study indicate a different rank order compared to earlier results from Pikal (i.e., the present results of negatively charged pores being smaller than the combination of neutral and charged pores compared to larger negative pores as suggested by Pikal), it is important to keep in mind that Pikal's experiments were conducted at different current densities and pH ranges.

On the basis of the work of Pikal and the results of the present study, nonionic molecules are likely to be iontophoretically transported (i.e. via electroosmosis) through only a fraction of the total pores available for permeant transport in HMS. Since *Pe* estimates were obtained using ionic permeant data to estimate the passive permeability coefficient and because electrophoretic enhancement of ionic permeant transport occurs in all of the available pore pathways (i.e., pathways with both neutral and negative surface charge), it is likely that that we may have underestimated the *Pe* values using the approach reported in the present study (i.e., the *Pe* values based on Eq. 2.19). We have therefore also examined a two-pathway model with the same data set. Using the Nernst-Planck equation and defining the term α to be the fraction of total pores with zero surface charge, Eq. 2.21 can be used to gain a sense of whether restricting the available pores for electroosmosis may provide insight into the differences in the *Rp* results between the nonionic and the ionic probe permeants.

$$P_{nonionic} = \frac{\varepsilon' HD}{h}\left[\alpha + \frac{(1-\alpha)Pe}{1-\exp(-Pe)}\right] \tag{2.21}$$

The above model takes into account the transport of nonionic permeants in pores with zero surface charge and in pores having negative surface charge. Generally, using a two-pathway model to calculate *Pe* and *Rp* values resulted in higher values of *Pe* but seemed to have little effect on the calculated *Rp* values compared to the values shown in Table 2.4.

Of practical significance is that the *Rp* values obtained using urea:mannitol as the permeant pair were similar to those obtained from experiments using HEM as the model

membrane. The mean *Rp* value obtained from urea:mannitol experiments with HMS was 6.7 Å (Table 2.4), whereas *Rp* values obtained in previous studies conducted in our laboratory using HEM under similar iontophoresis conditions and with urea:mannitol as the probe permeants were in the range 5.7 Å – 7.1 Å.[13,15]

2.5 Conclusions

Using the hindrance factor equations in conjunction with the modified Nernst-Planck model provided an opportunity to use steady-state permeability data collected from HMS iontophoresis experiments to systematically compare the transport of a range of permeants with different size and charge characteristics. Comparing the results of DC iontophoresis experiments with charged versus nonionic permeants confirmed the existence of heterogeneous pore pathways within the HMS epidermal membrane (possibly mammalian epidermal membranes in general) possesing differences in both pore size and variable surface charge characteristics. The results of iontophoresis experiments with ionic probe permeants showed modest ion-selectivity for HMS under conditions of the low current density DC iontophoresis of the present study. Given the reduced variability in electrical properties and the similarities between the experimental permeability coefficients and calculated *Rp* values for HMS compared to HEM, HMS was found to be an appropriate model membrane for HEM and may be considered for such under the conditions of the present study (low current density and relatively short duration).

These experiments were conducted under conditions in which the ionic strength and buffer composition was the same on both sides of the HMS. The current experiments

have also provided suitable baseline data for further systematic investigations where one side of the HMS was exposed to varying concentrations oligomeric polyanions.

2.6 References

1. Wearley L, Liu J-C, Chien YW 1989. Iontophoresis-facilitated transdermal delivery of verapamil. II. Factors affecting the reversibility of skin permeability. J Control Release 9:231-242.

2. Wearley L, Liu J-C, Chien YW 1989. Iontophoresis-facilitated transdermal delivery of verapamil. I. In vitro evaluation and mechanistic studies. J Control Release 8:237-250.

3. Burnette RR, Bagniefski TM 1988. Influence of constant current iontophoresis on the impedance and passive Na+ permeability of excised nude mouse skin. J Pharm Sci 77(6):492-497.

4. Pikal M 1990. Transport mechanisms in iontophoresis. I. A theoretical model for the effect of electroosmotic flow on flux enhancement in transdermal iontophoresis. Pharm Res 7(2):118-126.

5. Pikal M, Shah S 1990. Transport mechanisms in iontophoresis. II. Electroosmotic flow and transference number measurements for hairless mouse skin. Pharm Res 7(3):213-221.

6. Pikal M 1990. Transport mechanisms in iontophoresis. III. An experimental study of the contributions of electroosmotic flow and permeability change in transport of low and high molecular weight solutes. Pharm Res 7(3):222-229.

7. Prausnitz MR, Bose VG, Langer R, Weaver JC 1993. Electroporation of mammalian skin: a mechanism to enhance transdermal drug delivery. Proc Natl Acad Sci U S A 90(22):10504-10508.

8. Sims SM, Higuchi WI, Srinivasan V 1991. Interaction of electric field and electro-osmotic effects in determining iontophoretic enhancement of anions and cations. Int J Pharm 77:107-118.

9. Ruddy SB, Hadzija BW 1992. Iontophoretic permeability of polyethylene glycols through hairless rat skin: Application of hydrodynamic theory for hindered transport through liquid-filled pores. Drug Design and Discovery 8:207-224.

10. Luzardo-Alvarez A, Rodriguez-Fernandez M, Blanco-Mendez J, Guy RH, Delgado-Charro MB 1998. Iontophoretic permselectivity of mammalian skin: Characterization of hairless mouse and porcine membrane models. Pharm Res 15(7):984-987.

11. Hoogstraate AJ, Srinivasan V, Sims SM, Higuchi WI 1994. Iontophoretic enhancement of peptides: behavior of leuprolide versus model permeants. J Control Release 31(1):41-47.

12. Pikal M 2001. The role of electroosmotic flow in transdermal iontophoresis. Adv Drug Deliv Rev 46:281-305.

13. Li SK, Ghanem AH, Peck KD, Higuchi WI 1998. Characterization of the transport pathways induced during low to moderate voltage iontophoresis in human epidermal membrane. J Pharm Sci 87(1):40-48.

14. Zhu H, Peck KD, Li SK, Ghanem AH, Higuchi WI 2001. Quantification of pore induction in human epidermal membrane during iontophoresis: the importance of background electrolyte selection. J Pharm Sci 90(7):932-942.

15. Zhu H, Li SK, Peck KD, Miller DJ, Higuchi WI 2002. Improvement on conventional constant current DC iontophoresis: a study using constant conductance AC iontophoresis. J Control Release 82:249-261.

16. Peck KD, Ghanem AH, Higuchi WI 1994. Hindered diffusion of polar molecules through and effective pore radii estimates of intact and ethanol treated human epidermal membrane. Pharm Res 11(9):1306-1314.

17. Deen WM, Bohrer MP, Epstein NB 1981. Effect of molecular size and configuration on diffusion in microporous membranes. AIChE J 27:952-959.

18. Vinograd JR 1941. Diffusion of electrolytes and of the ions in their mixtures. Journal of American Chemical Society 63:2008-2015.

19. Beck RE, Schultz JS 1972. Hindrance of solute diffusion within membranes as measured with microporous membranes of known pore geometry. Biochim Biophys Acta 255:273-303.

20. Deen WM 1987. Hindered transport of large molecules in liquid-filled pores. A I Ch E Journal 33(9):1409-1425.

21. Li SK, Ghanem AH, Peck KD, Higuchi WI 1997. Iontophoretic transport across a synthetic membrane and human epidermal membrane: a study of the effects of permeant charge. J Pharm Sci 86(6):680-689.

22. Higuchi WI, Li SK, Ghanem AH, Zhu H, Song Y 1999. Mechanistic aspects of iontophoresis in human epidermal membrane. J Control Release 62(1-2):13-23.

23. Inada H, Ghanem AH, Higuchi WI 1994. Studies on the effects of applied voltage and duration of human epidermal membrane alteration/recovery and the resultant effects upon iontophoresis. Pharm Res 11(5):687-697.

24. Lide DR editor 1990. CRC handbook of chemistry and physics. 71st ed.: CRC Press (Taylor & Francis, Manhattan, New York, NY).

25. Lide DR editor 2002. CRC handbook of chemistry and physics. 84th ed.: CRC Press(Taylor & Francis, Manhattan, New York, NY).

26. Bowen WR, Welfoot JS 2002. Modelling the performance of membrane nanofiltration-critical assesment and model development. Chem Eng Sci 57:1121-1137.

27. Palmeri J, Blanc P, Larbot A, David P 2000. Hafnia ceramic nanofiltration membranes part II. Modeling of pressure-drived transport of neutral solutes and ions. J Memb Sci 179:243-266.

28. Banga AK. 1998. Electrically assisted transdermal and topical drug delivery. ed., Bristol, PA: Tayor & Francis. p 172.

29. Mitragotri S 2003. Modeling skin permeability to hydrophilic and hydrophobic solutes based on four permeation pathways. J Control Release 86:69-92.

30. Munch WD, Zestar LP, Anderson JL 1979. Rejection of polyelectrolytes from microporous membranes. J Memb Sci 5:77-102.

CHAPTER 3

IONTOPHORESIS OF SMALL NONIONIC MOLECULES WITH COTRANSPORT OF POLYSTYRENE SULFONATE OLIGOMERS

3.1 Introduction

The ability to enhance and control the transdermal delivery of bioactive agents is one of the principal motivations for the development of transdermal iontophoresis delivery systems. Because iontophoresis is typically considered as a method to enhance the delivery of molecules from an external compartment, the process of extracting analytes via iontophoresis is commonly referred to as reverse iontophoresis.[1-6] Although the potential for enhanced and controlled drug delivery from an external reservoir has been a significant focus of many investigators, the application of iontophoresis to extract therapeutically relevant molecules has also shown significant promise. In 2001 the Glucowatch Biographer® (Cygnus, Inc., Redwood City, CA) was approved by the US FDA to noninvasively monitor blood sugar levels in adults.[7] Leboulanger et al. have reviewed the application of reverse iontophoresis in monitoring several additional analytes of interest including phenytoin, lithium, valproate, theophylline, and clonidine

Reprinted with permission from John Wiley & Sons (Hoboken, NJ): Liddell MR, Li SK, and Higuchi WI. Transport behavior of hairless mouse skin during constant current DC iontophoresis, part 2: iontophoresis of nonionic molecules with cotransport of polystyrene sulfonate oligomers. J Pharm Sci 100(7): 2816-2825

among others.[8] One disadvantage of using this technique to monitor blood levels of analytes is the relatively slow rate of transport across the epidermal membrane and the low levels of the extracted analyte. Techniques to enhance the transport of molecules from the dermal or blood side of the epidermal membrane would be of value. By increasing the rate of extraction, it may be possible to reduce the lag time between the changes in the blood concentration and the extracted levels of analytes while at the same time reducing the analytical sensitivity requirements for the assay of the extracted analytes. One of the purposes of the current studies was to characterize the enhanced extraction of nonionic molecules observed during the cotransport of oligomeric polyelectrolytes.

In an effort to better understand the mechanisms involved in the iontophoretic transport of small molecules, our laboratory has conducted experiments to characterize the transport properties of the hairless mouse skin (HMS) epidermal membrane under constant direct current (DC) iontophoresis conditions. The results summarized in Chapter 2 have demonstrated the utility of using full thickness HMS as a model membrane to gain a better understanding of the behavior of the epidermal membrane during DC iontophoresis. Experiments described in Chapter 2 (referred to as "baseline" experiments) were conducted with equal concentrations of phosphate buffered saline (PBS) in both the cathodal and anodal compartments.

In preliminary experiments designed to improve the reproducibility and efficiency of reverse iontophoresis, it was noted that having sodium polystyrenesulfonate (PSS) present in the cathodal chamber of the iontophoresis system resulted in significant changes in the transport behavior of the HMS. In particular, the magnitude of

electroosmosis (one of the principal driving mechanisms of the iontophoretic transport for ionic and nonionic molecules) in constant current iontophoresis experiments appeared to increase considerably compared to baseline experiments. In the present and subsequent studies, iontophoretic permeability coefficients for the same set of permeants as those used in the baseline experiments have been determined under conditions in which varying concentrations of sodium PSS were present in the cathodal chamber of iontophoresis experiments which were conducted at the same current density as in the baseline studies. Although several investigators have previously reported results of experiments showing the iontophoresis-enhanced delivery of oligonucleotides and other moderately high molecular weight polyvalent ions,[9-12] the primary aim of the present study was to investigate changes that occur in the transport of nonionic permeants from the anodal chamber with the concomitant transport of an oligomeric polyanion (Mp > 1000 Daltons) from the cathodal chamber.

The following experimental strategy was used to quantify the changes in the transport behavior of the HMS when an oligomeric polyanion (PSS) was transported during low current density DC reverse iontophoresis extraction of nonionic permeants: (i) investigate the transport of PSS molecules across the HMS; (ii) measure the iontophoretic permeability coefficients of nonionic probe permeants and assess changes in the transport behavior of HMS when sodium PSS is present in the cathodal chamber; (iii) estimate the effective pore radius (*Rp*) based on the ratio of nonionic probe permeant permeability coefficients; and (iv) evaluate changes in the electrical properties of the HMS with varying concentrations of sodium PSS present in the cathodal chamber during

iontophoresis. All of the data collected in these experiments were compared with results of baseline experiments.

3.2 Materials and Methods

3.2.1 Materials

[^{3}H] raffinose (Raff) was obtained from American Radiolabeled Chemicals (St. Louis, MO). [^{14}C] Mannitol (Mann) and [^{3}H] mannitol were obtained from Perkin Elmer Life Sciences (Boston, MA). [^{14}C] Urea was obtained from Moravek Biochemicals (Brea, CA). Radiolabeled chemicals had an advertised purity of ≥ 98%. The purity of radiolabeled compounds was verified via HPLC before and after selected experiments. The diffusion coefficient and molecular radius of the radiolabeled permeants were previously determined in baseline experiments (see Table 3.1 for physical parameters reported with baseline studies). Chemicals used to prepare buffer and polyelectrolyte solutions were reagent grade and purchased from Sigma-Aldrich Company (St. Louis, MO), unless otherwise specified. Solutions were prepared using deionized water that was purified using a Milli-Q® filtration system (resistivity > 10 MΩ·cm: Millipore Corp., Billerica, MA). 0.1 M ionic strength phosphate buffered saline (PBS: 0.013 M total phosphate; 0.077 M NaCl) with 50 mg/L gentamicin added as a preservative was prepared and adjusted to pH 7.4. Liquid silver paint was obtained from Ladd Research Industries (Williston, VT). Silver foil and other laboratory supplies were obtained from VWR Inc. (West Chester, PA).

Table 3.1. Properties of radiolabeled permeants used for iontophoresis experiments.

Permeant	MW	D (10^{-6} cm^2/s)	r (Å)[a]
[^{14}C]-Urea	60	18 ± 1	2.5
[^{14}C]-Mannitol	182	8.9 ± 0.1	4.1
[^{3}H]-Raffinose	505	5.8 ± 0.4	5.9

[a] See Chapter 2 for details of diffusion coefficient experiments and radius calculations.

Sodium PSS calibration standard (Mp = 1370, Mw = 1430 and Mn = 1200) was obtained from American Polymer Standards (Mentor, OH). This particular sodium PSS calibration standard was selected because of its high water solubility (> 140 mg/mL), high molecular weight, and availability as a calibration standard having a relatively narrow polydispersity (Mw/Mn = 1.2) compared to other readily available commercial polymers. Solutions containing sodium PSS were prepared by mixing an appropriate amount of dry sodium PSS powder with purified water. For the highest concentration of sodium PSS (137 mg/mL) investigated, it was necessary to adjust the pH of the PSS solutions to pH 7 using a 50% w/w solution of NaOH (typically < 30 μL was required to neutralize 2 mL of the highest concentration sodium PSS solutions).

3.2.2 Solution conductance and viscosity determinations

The solution conductivity and relative viscosity of PBS and sodium PSS solutions were measured. The solution conductance was determined using a conductivity meter (Oakton WD-35607; Fisher Scientific, Pittsburgh, PA) at room temperature. Meter calibration was carried out using KCl calibration standards.

The relative viscosity of solutions was determined using an Ostwald viscometer (Fisher Scientific). The viscosity of sodium PSS solutions was determined at 27°C relative to water using the following relationship:

$$\eta_1 = \frac{\rho_1 t_1}{\rho_{H_2O} t_{H_2O}} \eta_{H_2O} \tag{3.1}$$

where ρ, t, and η are the density, flow time and viscosity of the solutions, respectively. Values for the density and viscosity of water at 27°C were 0.9956 g/mL and 0.8513 cp, respectively.[13]

3.2.3 HMS iontophoresis experiments with sodium PSS in the cathodal chamber

The cotransport of PSS during reverse iontophoresis experiments required some modifications to the setup compared to the experimental setup employed in baseline studies conducted with equal concentrations of PBS on both sides of the membrane. After sacrificing the animals (female hairless mice, strain SKH1-hr, at least 12 weeks old from Charles River, Wilmington, MA; all experiments were reviewed and approved by the Institutional Animal Care and Use Committee at the University of Utah), sections of skin were removed from the abdomen. HMS samples were placed between the two halves of the diffusion cell (volume of each half cell = 2 mL; diffusional area = 0.95 cm^2) and allowed to equilibrate with PBS on both sides of the membrane for 1.5 hours. Pre-equilibration with PBS on both sides of the membrane was performed to ensure that the initial resistance (R_{init}) was measured under conditions similar to those of the baseline experiments. To determine R_{init} of the HMS sample, 100 mV was applied across the sample and the resulting current was measured using a four-electrode potentiostat system (JAS Instrument Systems Inc., Salt Lake City, UT). Ohm's law was then used to calculate R_{init} of the membrane. Only those HMS samples with $R_{init} \geq 25$ k$\Omega \cdot cm^2$ after equilibration were used for the iontophoresis experiments. After measuring the initial resistance of the membrane, the PBS solution was removed from the half cell facing the stratum corneum

(cathodal chamber). The cathodal chamber was then rinsed repeatedly with purified water for 30 minutes. At the end of the rinse period, the selected sodium PSS solution was added to the cathodal chamber and the iontophoresis experiment was conducted.

The most significant modification made to the original experimental setup was the inclusion of a salt bridge (see Figure 3.1). The salt bridge prevented the intrusion of chloride ions produced at the cathodal electrode into the cathodal chamber. In previous experiments, the salt bridge was not necessary with PBS in both the cathodal and anodal chamber because the amount of chloride produced by the cathode was a small fraction compared to the bulk chloride (77 mM chloride concentration) in the PBS solution. In the present experiments, a salt bridge (site h), a 4-inch segment of Tygon® tubing filled with a solidified mixture containing 10 mg/mL of Type V agarose and 1 mg/mL of sodium PSS, was used to separate the location of the painted Ag/AgCl electrode (site i) from the cathodal chamber which contained the sodium PSS solution. A silver foil electrode (0.3 cm × 4 cm; site c) was attached to the constant current device and placed in the anodal chamber (the half cell facing the epidermis side of the HMS and containing PBS). The painted Ag/AgCl electrode (site i) was placed in a small beaker containing a solution of 1 mg/mL sodium PSS. The silver foil and Ag/AgCl electrodes were used to apply a constant current density of 0.11 ± 0.01 mA/cm^2 across the HMS. Additional silver foil electrodes were placed on each side of the HMS (sites d and e) and connected to a voltmeter (site b). These additional electrodes were used to monitor the voltage and current across the membrane throughout the experiment. The voltage and current across

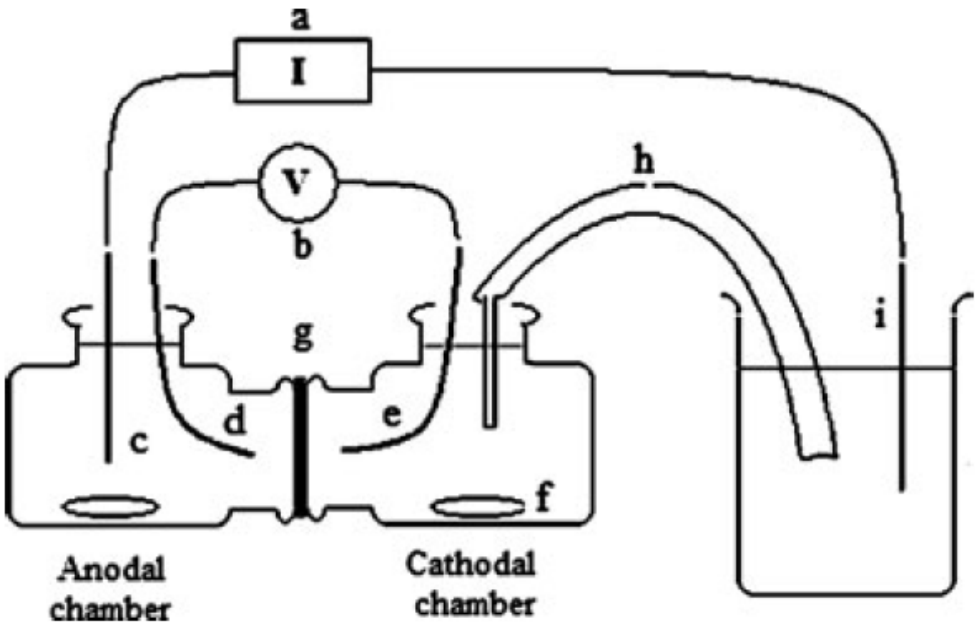

Figure 3.1. Schematic representation of iontophoresis experimental setup used for hairless mouse skin (HMS) experiments: (a) constant current power supply, (b) voltmeter used to monitor voltage drop across membrane, (c) silver foil electrode connected to constant current device and placed in the anodal chamber, (d) silver foil electrode placed on the dermis side of HMS and connected to a voltmeter, (e) silver foil electrode placed on the stratum corneum side of HMS and connected to voltmeter, (f) magnetic stir bar used to maintain constant stirring, (g) side-by-side glass diffusion cell, (h) salt bridge containing a mixture of 1 mg/mL PSS and 10 mg/ml Type V agarose with one end in the cathodal chamber and the other in a small beaker containing sodium PSS solution, and (i) painted Ag/AgCl electrode connected to the constant current device and placed in the beaker containing a solution of 1 mg/mL sodium PSS.

the membrane were monitored throughout the steady-state period of the experiments and used to calculate the steady-state resistance of the membrane, $R_{s\text{-}s}$. Constant stirring was maintained with magnetic stir bars on each side of the membrane. The entire diffusion cell assembly along with the beaker containing the Ag/AgCl electrode was submersed in a constant temperature water bath. The temperature of the bath was maintained at 37 ± 1°C.

Iontophoresis experiments were conducted using pairs of radiolabeled nonionic permeants. The anodal chamber was filled with the premixed solution of PBS containing trace amounts (0.25-1.0 μCi/mL) of the radiolabeled probe permeants and the cathodal chamber was filled with sodium PSS solutions of varying concentration. The pairing of trace permeants allowed for the calculation of effective pore radius values for each HMS experiment (explained below). Samples were taken from the receiver chamber and donor chamber for up to 6 hours. Receiver samples were replaced by an equivalent volume of fresh sodium PSS. All samples were mixed with 10 mL of liquid scintillation cocktail (Ultima Gold™, PerkinElmer Waltham, MA) and were assayed by liquid scintillation counting (Packard TriCarb™ Model 1900TR Liquid Scintillation Analyzer, PerkinElmer, Waltham, MA) using a dual counting protocol. After analysis by liquid scintillation counting, the following equation was used to calculate the experimental permeability coefficient (*P* or *P*-value):

$$P = \frac{1}{AC_D}\frac{\Delta Q}{\Delta t} \tag{3.2}$$

where A is the area of the membrane, C_D is the concentration of the permeant of interest in the donor chamber, and $\Delta Q/\Delta t$ is the slope of the receiver cumulative amount vs. time plot (only the steady-state region where $R^2 > 0.98$ was used to calculate the permeability coefficients). The permeability coefficient of a permeant refers to the flux normalized by the concentration of permeant in the donor chamber ($P = J/C_D$). The linear region of the receiver cumulative amount versus time plot generally consisted of data collected when $t \geq 2$ hours.

3.2.3.1 Two-stage HMS iontophoresis experiments

The purpose these experiments was to investigate whether significant irreversible damage to the HMS occurred as a result of exposure to sodium PSS solutions compared to control experiments where only PBS is present on both sides of the membrane throughout the iontophoresis experiments. To answer this question iontophoresis experiments were conducted under conditions similar to those described above; however, in the two-stage experiments the iontophoresis portion of the experiment (Stage I) ended after 2 hours, when the solution in the cathodal chamber was replaced with fresh PBS and passive diffusion experiments (Stage II) were continued for an additional 8 hours. Experiments were conducted under two conditions: 1) with varying concentrations of sodium PSS in the cathodal chamber during Stage I and then with PBS on both sides of the membrane during Stage II; or 2) with PBS in the anodal and cathodal chambers during both Stages I and II. Two-stage experiments were conducted with [^{14}C] mannitol as the nonionic probe permeant.

3.2.4 Theoretical considerations

For nonionic permeants, Eq 3.3 can be used to describe the steady-state flux of permeants across the HMS.[14]

$$J_{nonionic} = \varepsilon' \left[-HD\frac{dC}{dx} \pm WvC \right] \tag{3.3}$$

where ε' is effective porosity of the membrane (the effective porosity of the membrane is defined by $\varepsilon' = \varepsilon / \tau$, where ε is the porosity and τ is the tortuosity of the membrane), H is the hindrance factor for diffusion through a pore, D is the diffusion coefficient of the permeant in bulk media, C is the concentration at a given location in the membrane, W is the hindrance factor for transport through a pore driven by convective solvent flow, and v is the average velocity of the convective solvent flow. Both W and H are functions of the pore radius, Rp, and the permeant radius, r. The hindrance factors W and H have been discussed in relation to the baseline studies (see Chapter 2) and related information regarding the derivation and various forms of the equations can be found in the literature.[15] In order to calculate the effective pore size of the pathway utilized by nonionic permeants, we assume that the passive flux component of the steady-state flux is much less than the electroosmosis component, i.e. $HD\left(\frac{dC}{dx}\right) << WvC$, when this is true taking the ratio of nonionic permeant pair P-values results in the following equation:

$$\frac{P_{nonionic,1}}{P_{nonionic,2}} = \frac{W_1}{W_2} \tag{3.4}$$

The assumption that the electroosmotic flux of nonionic permeants is much greater that the passive flux component will be discussed later.

3.2.5 Analyses of PSS sample solutions using capillary electrophoresis

A capillary electrophoresis system (CE; P/ACE System 5500, Beckman Coulter, Fullerton, CA) was used to confirm the transport of PSS across the HMS. CE separations were performed by applying a potential of 15.0 kV across a coated neutral CE capillary (eCAP^{TM}; 50 μm ID; 50 cm to window; 57 cm total length). Before use, the capillary was rinsed with filtered PBS solution. Samples were injected into the capillary using hydrodynamic injection with a pressure of 0.5 psi for 20 seconds. Prior to injection, all samples were filtered using a standard HVLP-type hydrophilic syringe filter with a 5 μm pore size. Samples containing benzyl alcohol (used as an electroosmotic flow marker to assess the integrity of the neutral capillary coating) and salicylic acid (reference compound) were analyzed at 254 nm. Samples containing PSS were analyzed at 214 nm. CE separations were carried out at 27°C. Separations of PSS standard solutions were conducted using 0.02 M ionic strength PBS as the background electrolyte. Eq. 3.5 was used to calculate the electromobility (μ) of the individual peaks of the CE separations.

$$\mu = \frac{L_t L_w}{V}\left(\frac{1}{t_{mig}} - \frac{1}{t_{ref}}\right) + \mu_{ref} \tag{3.5}$$

where L_t is the total length of the capillary, L_w is the length of the capillary to the window, V is the applied voltage, t_{mig} is the migration time, t_{ref} and μ_{ref} are the migration time and electromobility of salicylic acid, respectively.

3.2.6 Verification of PSS transport across HMS

Iontophoresis experiments were conducted with 137 mg/mL sodium PSS in the cathodal chamber (i.e., the donor chamber which faced the stratum corneum side of the membrane) without radiolabeled permeants in the system. The purpose of this analysis was to provide semi-quantitative permeability coefficients and to demonstrate that a portion of the electric current applied to the HMS was carried by high molecular weight PSS oligomers. The experimental setup and protocol for the PSS flux experiments were similar to those described for the probe permeant experiments with a few slight modifications. One difference was that PSS transport experiments were conducted over a 16 hour period with samples collected from the receiver chamber at 10, 12, 14 and 16 hours. The extended duration of the PSS flux experiments allowed for sufficient accumulation of PSS in the receiver chamber and ensured that PSS flux has reached steady-state. Because the length of the experiments was extended, the salt bridges were replaced every 6 hours to ensure that chloride ions did not accumulate in the cathodal chamber.

The collected samples were analyzed using the CE method described above and the permeability coefficients of the individual PSS oligomers were calculated using Eq. 3.2 under the assumption that the peak area under the curve (AUC) values were proportional to the concentration of individual PSS oligomers in the collected sample.

Because the iontophoresis experiments with sodium PSS were conducted with 0.1 M PBS in the anodal chamber, 0.1 M PBS was used as the background electrolyte during CE analysis of samples collected from the donor and receiver chambers. The permeability coefficient for each of the individual PSS species was calculated based on the flux of the PSS species (in terms of AUC/cm^2/s) into the receiver chamber divided by the concentration of the same PSS species in the donor chamber (see Eq. 3.2). The result was the calculated permeability coefficient for each of the peaks found in the CE separation of samples taken from the donor and receiver chambers.

3.3 Results

3.3.1 Examination of bulk solution properties

The results of the solution conductance and viscosity experiments with sodium PSS solutions are shown in Table 3.2. Viscosity measurements were performed at 27°C. The viscosity of 1.37 mg/mL and 13.7 mg/mL PSS solutions was the same order of magnitude to that of PBS at 27°C. The viscosity of the 137 mg/mL PSS solution was noticeably higher than the viscosity of all other solutions used in this study. As expected, the conductivity of sodium PSS solutions increased as the concentration of PSS increased. The conductivity of the 13.7 mg/mL PSS solution was similar to that of 0.1 M PBS solutions and the rank order of conductivity measurements of sodium PSS solutions was also reflected in the rank order of the steady state resistance ($R_{s\text{-}s}$) measured during the HMS iontophoresis experiments with probe permeants. The deviation from linearity of the PSS solution conductivity with respect to the concentration of

Table 3.2. Viscosity and conductivity measurements for PBS and PSS solutions.

Solution	Solution Conductance (mS)[a]	Solution Viscosity (cp)[b]
PBS	9.0	0.85
PSS		
1.37 mg/mL	0.6	0.84
13.7 mg/mL	4.3	0.90
137 mg/mL	31.5	1.36

[a] Solution conductance measurements were performed at ambient temperature.
[b] Viscosity measurements were performed at 27°C.

sodium PSS is consistent with the decreasing electromobility of the PSS oligomers with increasing PSS concentration as reported by Cottet et al.[16]

3.3.2 CE analyses of sodium PSS solutions

Figure 3.2 shows a typical CE separation of a 0.6 mg/mL sodium PSS standard solution. The separation was performed with 0.02 M PBS as the background electrolyte to allow for direct comparison to the results obtained by Cottet et al.[16,17] The peak numbers shown in Figure 3.2 reflect the degree of polymerization for each of the PSS oligomers. Because the sodium PSS standards were obtained from the same commercial source, peak numbers were assigned based on a comparison of the electromobility values shown in Table 3.3 versus those obtained by Cottet et al. under similar capillary electrophoresis conditions.[16] Differences in the electromobility values observed in the current experiments compared to those reported by Cottet et al. ranged from 4 – 8%. The observed disparity was likely a result of differences in separation conditions used for CE experiments such as the composition of the background electrolyte, the type of capillary used, and the configuration of the electrophoresis equipment. Also shown in Table 3.3 are the effective charge (z_{eff}), Stokes-Einstein radius (R_{SE}), hydrodynamic radius (r), and diffusion coefficient (D) of the PSS oligomers. The z_{eff}, R_{SE}, and D of the individual PSS oligomers were interpolated from data reported by Böhme and Scheler.[18]

Capillary electrophoresis was also used to analyze the PSS oligomers in the solutions taken from the donor and receiver chambers in the PSS transport experiments with 137 mg/mL sodium PSS. Figure 3.3 shows a CE separation of representative samples taken from the donor and receiver chambers during PSS flux experiments. Of the

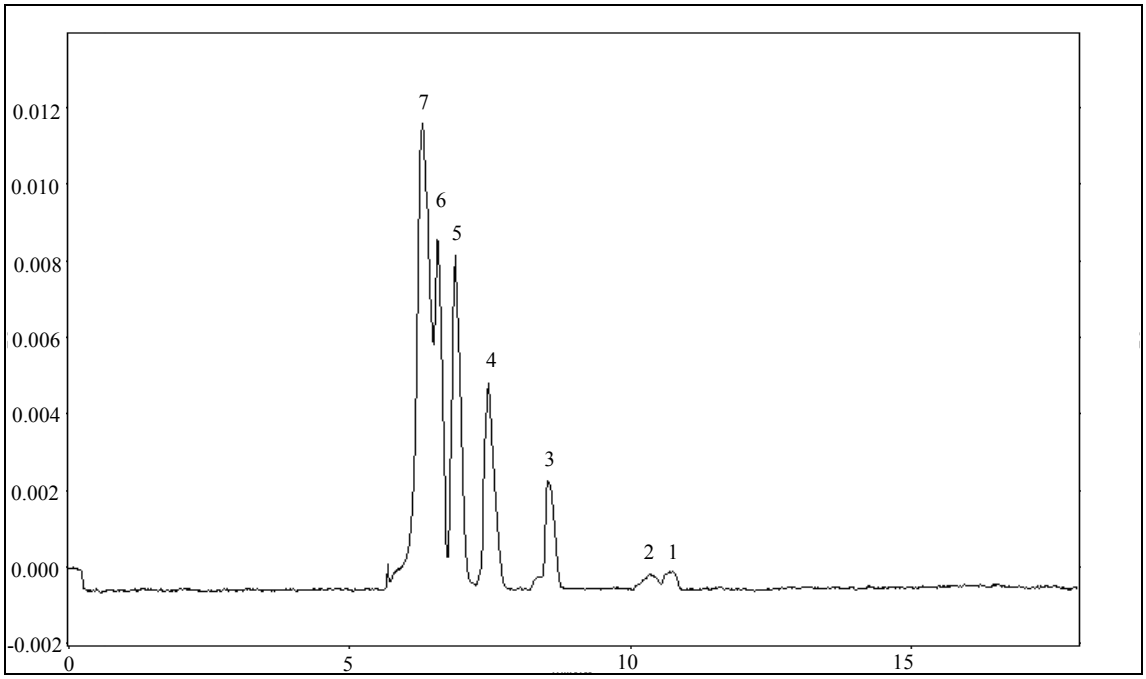

Figure 3.2. Capillary electrophoresis separation of 0.6 mg/mL PSS standard. Coated neutral capillary, 50 μm ID, 57 cm total length (detector, 50 cm); electrolyte 0.02 M PBS buffer; applied voltage, 15 kV; hydrodynamic injection, 0.5 psi for 20 s; temperature, 27°C. Peak numbering reflects the charge of the PSS fragment based on a comparison of the electromobility values for the individual PSS peaks with those reported by Cottet et al. (see Table 3.3).[16] The units of the abscissa are minutes. The units of the ordinate are absorbance units.

Table 3.3. Electromobility measurements, physical properties, and experimental permeability coefficients of the PSS oligomers.

N [a]	μ (10^{-4} $cm^2V^{-1}sec^{-1}$)[b]	μ (10^{-4} $cm^2V^{-1}sec^{-1}$)[c]	z_{eff} [d]	R_{SE} (Å)[d]	r (Å)[d]	D ($\times10^{-6}$ cm^2/s)[e]	P_{exp} ($\times10^{-7}$ cm/s)
3	4.1	3.8	-2.5	3.7	4.2	8.9	2.2 ± 1.5
4	4.7	4.4	-3.2	4.7	5.0	7.0	3.2 ± 1.1
5	5.0	4.7	-3.9	5.6	5.9	5.8	3.2 ± 2.5
6	5.1	4.9	-4.5	6.6	6.8	5.0	--
7	5.3	5.1	-5.1	7.4	7.5	4.4	1.8 ± 0.5

[a] The assigned number of repeat units corresponds to the degree of polymerization, N.
[b] Values from Cottet et al.[16] (0.02 M ionic strength, borate buffer at pH 9.0, 27°C)
[c] Experimental electromobility values calculated from CE migration time data and Eq. 3.5. (0.02 M ionic strength, phosphate buffer at pH 7.4, 27°C)
[d] z_{eff} and R_{SE} values were estimated from Böhme and Scheler[18]; r was calculated from R_{SE} using Eq. 2.2 and Eq. 2.3.
[e] The diffusion coefficient, D, was calculated from the R_{SE} value using Eq. 2.2.

six peaks shown in the separation of the donor sample (see Figure 3.3), only four of the peaks appeared in measureable amounts in the receiver chamber. The experimental permeability coefficients of the four major peaks of the receiver sample shown in Figure 3.3 are reported in the final column of Table 3.3. The greater ionic strength of the conducting electrolyte in these experiments resulted in lower resolution between the peaks of the CE separation. The experimental apparent permeability coefficient, $P_{exp,app}$, was also calculated by combining all of the PSS peaks. Using this approach, $P_{exp,app}$ was found to be 2.3×10^{-7} cm/s $\pm$ 1.3×10^{-7} cm/s.

3.3.3 Iontophoresis experiments with nonionic permeants

Table 3.4 shows the results of iontophoresis experiments with sodium PSS in the cathodal chamber and with the nonionic permeants in the anodal chamber. The particular design of the experiments with the nonionic permeants was chosen to maximize obtaining information of interest with regard to the enhanced reverse transdermal iontophoresis (extraction) of nonionic permeants. The data are the initial HMS resistance (R_{init}), the steady-state resistance of HMS during iontophoresis ($R_{s\text{-}s}$), the permeability coefficients ($P_{nonionic}$) of urea, mannitol, and raffinose (calculated using Eq. 3.2), and *Rp* calculated from the mean of $P_{nonionic,1}/P_{nonionic,2}$ ratios and using Eq. 3.4. The data in the parenthesis of the last column show the upper and lower limits of *Rp* estimates which have been calculated based on the upper and lower limits of the 95% confidence interval (CI) of mean $P_{nonionic,1}/P_{nonionic,2}$ values. Although the $R_{s\text{-}s}$ of the HMS changed with varying concentrations of sodium PSS in the cathodal chamber, the mean permeability

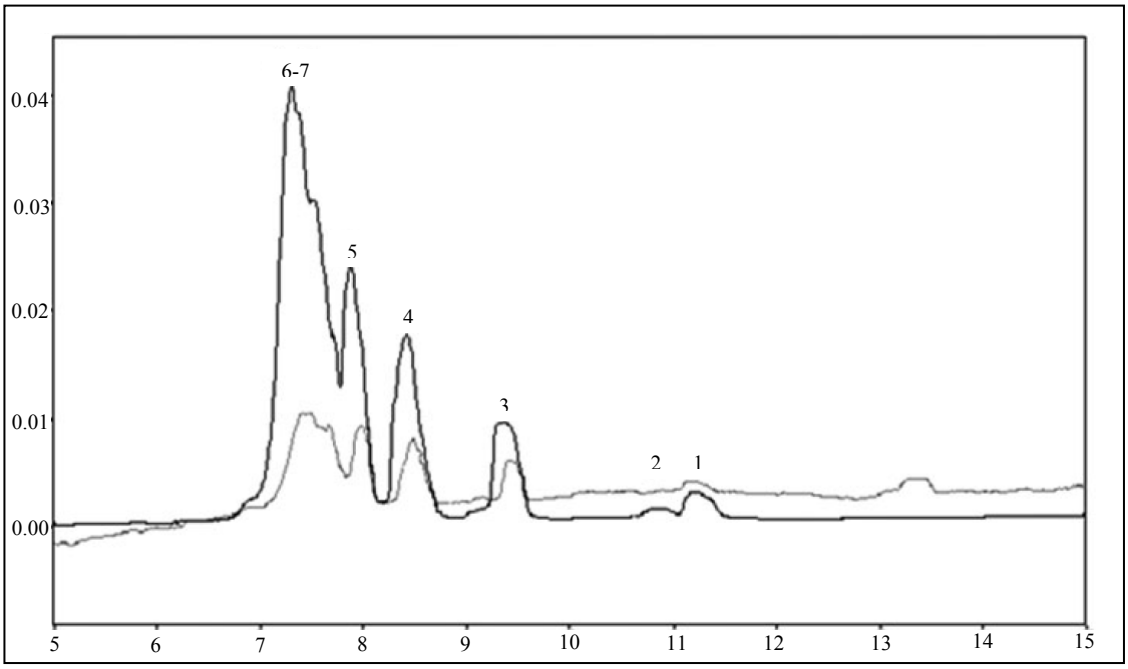

Figure 3.3. Capillary electrophoresis separation of samples collected from extended HMS iontophoresis experiments with 137 mg/mL sodium PSS solution in the cathodal chamber and PBS in the anodal chamber. Coated neutral capillary, 50 μm ID, 57 cm total length (50 cm to detector); electrolyte 0.1 M PBS buffer; applied voltage, 15 kV; hydrodynamic injection, 0.5 psi for 20 s; temperature, 27ºC. Light gray line represents samples taken from the receiver chamber at 10 hours. The solid black line represents samples taken from donor chamber at 10 hours. The units of the abscissa are minutes. The units of the ordinate are absorbance units.

Table 3.4. Summary of data (mean ± SD) from nonionic probe permeant iontophoresis experiments with sodium PSS in the cathodal chamber and with the probe permeant in the anodal chamber.

PSS conc. (mg/mL)	Permeant Pair	Number of Exp. (n)	R_{init} (kΩ·cm^2)	$R_{s\text{-}s}$ (kΩ·cm^2)	$P_{nonionic,1}$ (10^{-7} cm/s) [a]	$P_{nonionic,2}$ (10^{-7} cm/s) [a]	*Rp* (Å)
1.37	Urea:Mann	4	100 ± 86	8 ± 2	13 ± 1	7.5 ± 0.5	9.1 (8.6, 9.9)
	Urea:Raff	4	73 ± 42	7.0 ± 0.9	16 ± 2	6 ± 2	11 (9, 14)
	Mann:Raff	6	82 ± 42	9 ± 1	8 ± 1	7 ± 1	27 (24, 31)
13.7	Urea:Mann	3	101 ± 87	4.4 ± 0.2	12 ± 1	9 ± 1	12 (10, 15)
	Urea:Raff	6	99 ± 83	4.5 ± 0.7	12 ± 2	8 ± 2	15 (14, 17)
	Mann:Raff	3	102 ± 86	5 ± 1	8 ± 2	7 ± 3	24 (15, ∞)
137	Urea:Mann	4	72 ± 64	3.2 ± 0.5	13 ± 2	8 ± 2	9.7 (8.8, 11.3)
	Urea:Raff	3	88 ± 68	4 ± 1	12.9 ± 0.1	7 ± 1	13 (11, 22)
	Mann:Raff	7	100 ± 106	4 ± 1	9 ± 2	8 ± 2	20 (16, 29)

[a] $P_{nonionic,1}$ and $P_{nonionic,2}$ are the first and the second probe permeant, respectively, given in column 2.

coefficients of nonionic permeants were not significantly different from each other for the different PSS concentrations investigated (ANOVA; $p > 0.05$).

Figure 3.4 presents the permeability coefficients for the nonionic probe permeants plotted against their respective diffusion coefficients. The baseline data have also been included to illustrate the enhancements observed for the nonionic permeant permeability coefficients relative to the baseline experiments with PBS in both the anodal and cathodal compartments (see Chapter 2). Up to a fourfold enhancement for urea and up to a sixfold enhancement for both raffinose and mannitol were observed. Given these large enhancement values relative to the baseline results, it may be concluded that the present experiments with the nonionic probe permeants were essentially under convective flow limiting conditions. Figure 3.4 also illustrates that the nonionic permeant fluxes were relatively insensitive to the PSS concentration over the range of the PSS concentrations investigated.

Table 3.5 shows the results of two-stage experiments. The results include the mean permeability coefficients (mean ± SD for n = 3 experiments) for Stage I and Stage II of the experiments , the initial resistance (R_{init}) and experimental resistance (R_{exp}) measured during the experiments [Note: R_{exp} is different from $R_{s\text{-}s}$, since, given the short duration of Stage I in the experiments, it was not possible to determine whether the experiments had reached steady-state. R_{exp} is the last resistance measurement taken at the end of Stage I.]. For comparison, the mean permeability coefficients of [^{14}C]-mannitol were also reported earlier in Table 3.4 (data from the mannitol: raffinose pairs). With the exception of experiments with

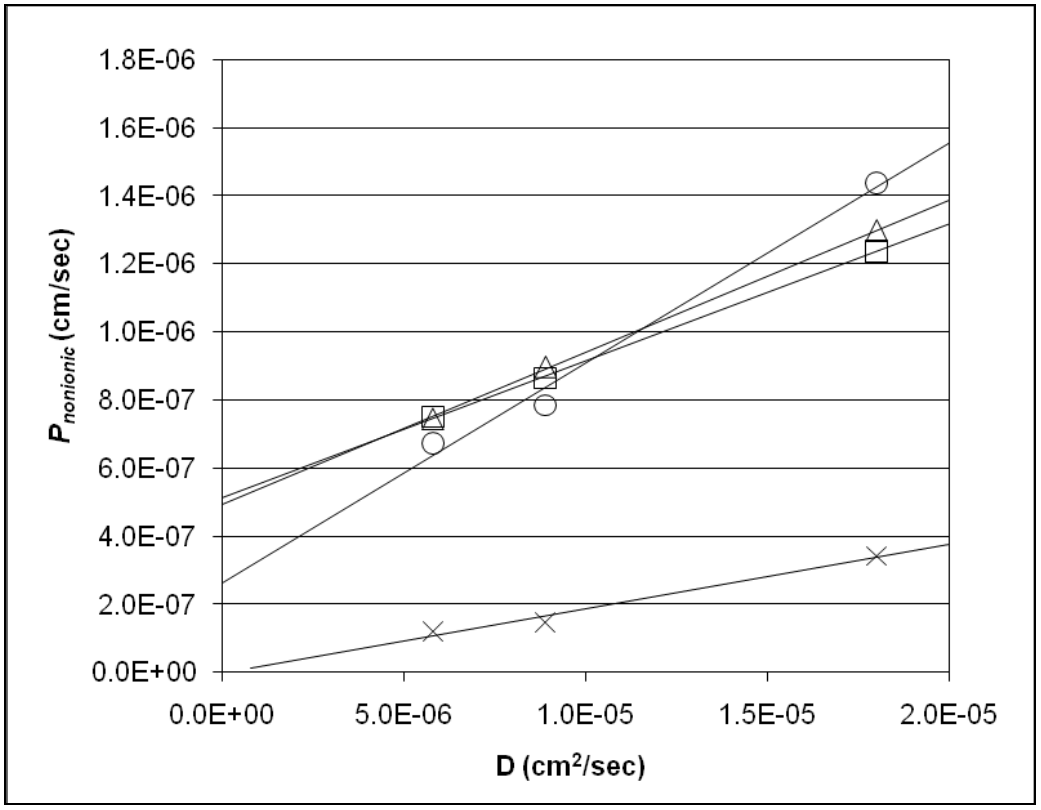

Figure 3.4. Experimental permeability coefficients of nonionic permeants plotted versus their respective diffusion coefficients. The different symbols indicate 1.37 mg/mL (○), 13.7 mg/mL (Δ), and 137 mg/mL (□) sodium PSS in cathodal chamber. Data from baseline studies with PBS in both the anodal and cathodal chamber (×) are also shown.

Table 3.5. Permeability coefficients (mean ± SD) of [^{14}C] mannitol during Stage I and Stage II of the two-stage experiments.

Cathodal solution [a]	R_{init} (kΩ·cm^2)	R_{exp} (kΩ·cm^2)	$P_{mann,Stage\ I}$ (10^{-7} cm^2/s)	$P_{mann,Stage\ II}$ (10^{-7} cm^2/s)
PBS	30 ± 17	4.4 ± 0.6	2.3 ± 0.4	1.8 ± 0.3
1.37 mg/mL PSS	25 ± 20	6.7 ± 0.5	6.5± 1.8	2.0 ± 0.3
13.7 mg/mL PSS	38 ± 31	3.8 ± 1.0	4.8± 1.0	2.1 ± 0.5
137 mg/mL PSS	29 ± 23	2.6 ± 0.6	6.7± 3.6	2.3 ± 0.9

[a] The cathodal solution refers to the solution in the cathodal chamber during Stage I of the experiments.

PBS in both chambers (compare data from mannitol: raffinose pair reported in Table 2.4), the permeability coefficients reported in Table 3.5 were consistently lower than those measured in earlier studies. The most likely reason for this is that the iontophoresis stage of the experiments was not long enough to obtain true steady-state permeability coefficients. The hypothetical passive permeability coefficient for mannitol that was calculated based on the ionic permeant data from Chapter 2 is 5.7×10^{-8} cm/s (see section 2.3.3 for a description of the method used to obtain the passive permeability coefficient of mannitol) which is about a factor of three lower than the $P_{mann,Stage\ II}$ value reported for the current system. A possible explanation for differences in the permeability coefficients of [^{14}C]-mannitol can be seen in the experimental resistance measurements of the HMS samples used in the two-stage experiments: $R_{exp} = 4.4 \pm 0.6$ kΩ·cm^2 for two-stage experiments compared to overall mean ± SD of $R_{s\text{-}s}$ from Table 3.4 which was 6.2 ± 1.5 kΩ·cm^2. The lower resistance of HMS samples used in the two-stage experiments may indicate that these membranes had a higher porosity compared to that of HMS samples used in the experiments summarized in Table 3.4.

3.4 Discussion

3.4.1 Iontophoretic transport of PSS oligomers across HMS

Although the principle focus of the current studies was to investigate the effect that the cotransport of oligomeric polyanions has on the iontophoresis of nonionic permeants, CE analysis of samples from the receiver and donor chambers provide data for estimating permeability coefficients of the PSS oligomers transported into and across the HMS under the low current DC iontophoresis conditions investigated in this study.

The appearance of PSS in the receiver chamber provides direct evidence that under the iontophoretic conditions investigated in the current study, PSS oligomers were transported into and across the HMS membrane.

3.4.2 Consideration of factors contributing to the iontophoretic enhancement of the nonionic permeants

3.4.2.1 Changes in the electrical properties of HMS

Consistent with the conductivity of the bulk PSS solutions (see Table 3.2), $R_{s\text{-}s}$ values decreased as the concentration of PSS in the system increased. As all of the experiments were conducted under constant current conditions, decreases in the value of $R_{s\text{-}s}$ (calculated based on the observed voltage drop across the HMS during iontophoresis experiments) indicated that the applied voltage required for maintaining constant current decreased as the concentration of sodium PSS in the cathodal chamber was increased. The mean ± SD of $R_{s\text{-}s}$ for HMS with 1.37, 13.7, and 137 mg/mL PSS in the cathodal chamber was 7.7 ± 1.7, 4.4 ± 0.9, and 3.3 ± 1.0 $k\Omega \cdot cm^2$, respectively. In the baseline studies the mean ± SD of the $R_{s\text{-}s}$ was 6.4 ± 1.5 $k\Omega \cdot cm^2$ (see Chapter 2). The average voltage drop across the HMS in the baseline experiments was comparable to (1.37 mg/mL) or less than (13.7 mg/mL and 137 mg/mL) the values for the PSS cases; consequently, changes in the electric field, per se, across the HMS would not appear to explain the enhanced fluxes in the PSS experiments.

3.4.2.2 Possible irreversible damage to HMS from exposure to sodium PSS solution

Changes in the resistance of the membrane during iontophoresis experiments may be evidence of permanent damage caused by exposure of the stratum corneum to sodium PSS solutions in the cathodal chamber. Since resistance measurements alone were not enough to answer the question of whether irreversible damage was being done to the HMS by exposing the stratum corneum to sodium PSS solutions, two-stage iontophoresis and passive permeability experiments were conducted. The results summarized in Table 3.5 show that the differences among the mean passive permeability coefficients measured during Stage II of the experiments appear to be within the experimental scatter of the data for all of the various solutions that were present in the cathodal chamber (i.e., varying concentrations of sodium PSS or PBS) during Stage I of the experiments. As one might expect, the largest difference among $P_{mann,Stage\ II}$ values was for experiments with PBS in the cathodal chamber compared to experiments with 137 mg/mL PSS in the cathodal chamber during Stage I of the experiments. Although the mean $P_{mann,Stage\ II}$ values are consistently higher for experiments with PSS in the cathodal chamber during Stage I, the largest difference was only about 28%, suggesting that there may be an increase in the porosity of HMS samples that were exposed to sodium PSS during Stage I of the experiments compared to HMS samples that had PBS on both sides of the membrane throughout the experiment. Even if the observed increase of 28% were a direct indication that the porosity of the HMS has increased by the same amount, this increase is not sufficient to explain the sixfold increase in the iontophoretic permeability coefficients of nonionic probe permeants when sodium PSS is present in the cathodal chamber.

3.4.2.3 Changes in the effective pore radius, *Rp*

The values of *Rp* calculated from nonionic permeant data provide additional insight into the effect that the cotransport of oligomeric polyanions had on the transport pathways available to the nonionic probe permeants. Compared to the baseline experiments with HMS (baseline *Rp* values calculated based on the mean ratio of permeability coefficients for nonionic probe permeants ranged from 7 – 15 Å) *Rp* values calculated in the current experiments based on the mean permeability coefficient ratios for nonionic probe permeant pairs ranged from 9 – 27 Å when sodium PSS was in the cathodal chamber. Using the maximum value of *Rp* measured from nonionic permeant data collected from the baseline experiments (15 Å) and the current experimental conditions (27 Å) the hindrance factor *W* (see Eqs 2.6, 2.8 and 2.9) for raffinose increases from 0.5 to 0.8, respectively. Given the fact that *W* increases by only 60%, the sixfold increase in the permeability of raffinose cannot be explained by the increase in the observed *Rp* values alone.

3.4.2.4 Changes in the percentage of active pores for electroosmosis

A conclusion from the baseline experiments (Chapter 2) was that the pathways utilized by the nonionic permeants during iontophoresis, that is, pathways with negative pore surface charge, were likely only a fraction of the total pathways that were available for charged permeant transport during iontophoresis (note: the charged permeants should be capable of utilizing all of the pathways within the limits prescribed by the hindrance factor). This point of view is consistent with the HMS studies by Pikal and Shah.[19-21] It would follow from the present results that if a higher percentage of the pores than in the

baseline study were utilized by the nonionic probe permeants in the present PSS experiments, this may contribute towards both an enhancement of the electroosmotic flux and a larger effective pore size for transport (note: it was also shown in the baseline studies that the pore sizes deduced with iontophoresis data employing ionic permeants generally yielded larger pore sizes than when nonionic permeants were employed). In the next chapter experiments with ionic probe permeants will be conducted to test whether changes in the effective pore radii for pathways utilized by charged permeants are observed when sodium PSS is present in the cathodal chamber.

3.4.2.5 Possible contribution of pore surface charge density (σ)

Any significant adsorption of the PSS oligomer ions at the pore-solution interface may increase σ relative to the baseline study σ value, this leading to enhanced electroosmosis velocities.[22-24] Adsorption of PSS ions in pores that were uncharged or positively charged in the baseline experiments may lead to an increase in the percentage of active pores for electroosmosis (discussed above). Taken together with a possible increase of σ in the already negatively charged pores may be a possible explanation for both the electroosmotic flux enhancement and the larger pore sizes deduced in the present study. However, if PSS oligomer adsorption and a significantly increased σ in the presence of solution PSS were to be important, the constancy of the $P_{nonionic}$ values over a 100-fold range of sodium PSS concentration (see Table 3.4) would seem to be surprising.

Hirvonen and Guy have studied the effect of delivering anionic and cationic polypeptides across HMS via iontophoresis.[25] These investigators showed that increasing the concentration of cationic polypeptide in the iontophoresis system resulted in the

suppression of electroosmosis. The authors hypothesize that the suppression of electroosmosis occurs as a result of the cationic polypeptide interacting with the negatively charged surface resulting in neutralization of the negative surface charge of the membrane. Hirvonen and Guy also investigated the effect of delivering polyanionic peptides and concluded that the largest electroosmosis enhancement observed was about threefold when compared to their baseline studies. They concluded that the most significant change in electroosmosis resulted from the delivery of polyvalent cations, which resulted in a sixfold decrease in the magnitude of electroosmosis. The results of the present experiments show that a sixfold increase in the magnitude of electroosmosis is also possible when polyvalent anions are cotransported during iontophoresis of nonionic permeants.

3.4.3 Iontophoretic delivery of oligomeric polyanions and other potential applications

In practice, the findings described in this report may have applications in the field of reverse iontophoresis and iontophoretic delivery of moderately-sized polyvalent anionic molecules. In addition to the significant enhancement in the iontophoresis of nonionic permeants, the introduction of polyvalent anions into the cathodal chamber of the iontophoresis system resulted in a significant decrease in the voltage required to maintain a constant current density. As a result, the current approach could also be used as a method to decrease the power requirements needed to maintain a constant current density over extended periods of time. Similar behavior has also been observed in experiments using heat separated human epidermal membrane (HEM) as the model

membrane. Preliminary experiments conducted with HEM have shown that the permeability coefficients of raffinose increase by as much as tenfold when a 1.37 mg/mL solution of sodium PSS was placed in the cathodal chamber during constant current DC iontophoresis experiments (data not published).

3.5 Conclusions

The current study examined the changes in the transport properties of HMS during the delivery of PSS oligomers and its effect on the iontophoretic extraction of nonionic permeants. Compared to baseline iontophoresis experiments with PBS on both sides of the membrane, the permeability coefficients of nonionic probe permeants increased up to sixfold when sodium PSS solutions were in the cathodal chamber (the chamber facing the stratum corneum of the HMS) of the iontophoresis system. Although the applied voltage needed to maintain constant current decreased with increasing PSS concentration, permeability coefficients for nonionic probe permeants increased to a constant level independent of the concentration of PSS in the cathodal chamber and independent of the applied voltage required to maintain constant current. The results of the present iontophoresis studies with PSS and the nonionic permeants provide important information related to the convective flux of permeants in HMS that will be added to the database of knowledge used in the analyses of subsequent studies that characterize the transport of low molecular weight ionic permeants under the same conditions of sodium PSS in the cathodal chamber.

3.6 References

1. Wascotte V, Delgado-Charro MB, Rozet E, Wallemacq P, Hubert P, Guy RH, Preat V 2007. Monitoring of urea and potassium by reverse iontophoresis in vitro. Pharm Res 24(6):1131-1137.

2. Leboulanger B, Aubry JM, Bondolfi G, Guy RH, Delgado-Charro MB 2004. Lithium monitoring by reverse iontophoresis in vivo. Clin Chem 50(11):2091-2100.

3. Delgado-Charro MB, Guy RH 2003. Transdermal reverse iontophoresis of valproate: a noninvasive method for therapeutic drug monitoring. Pharm Res 20(9):1508-1513.

4. Potts RO, Tamada JA, Tierney MJ 2002. Glucose monitoring by reverse iontophoresis. Diabetes Metab Res Rev 18 Suppl 1:S49-53.

5. Rao G, Glikfeld P, Guy RH 1993. Reverse iontophoresis: development of a noninvasive approach for glucose monitoring. Pharm Res 10(12):1751-1755.

6. Benjamin BF, Cornbleet T 1954. Cutaneous sodium and potassium determined by reverse iontophoresis. J Invest Dermatol 23(4):287-292.

7. Tierney MJ, Tamada JA, Potts RO, Jovanovic L, Garg S 2001. Clinical evaluation of the GlucoWatch biographer: a continual, non-invasive glucose monitor for patients with diabetes. Biosens Bioelectron 16(9-12):621-629.

8. Leboulanger B, Guy RH, Delgado-Charro MB 2004. Reverse iontophoresis for non-invasive transdermal monitoring. Physiol Meas 25(3):R35-50.

9. Liu J-C, Sun Y 1994. Transdermal delivery of proteins and peptides by iontophoresis: Development, challenges, and opportunities. Drugs Pharm Sci 62(DRUG PERMEATION ENHANCEMENT):247-272.

10. Li SK, Ghanem AH, Teng CL, Hardee GE, Higuchi WI 2001. Iontophoretic transport of oligonucleotides across human epidermal membrane: a study of the Nernst-Planck model. J Pharm Sci 90(7):915-931.

11. Hoogstraate AJ, Srinivasan V, Sims SM, Higuchi WI 1994. Iontophoretic enhancement of peptides: behavior of leuprolide versus model permeants. J Control Release 31(1):41-47.

12. Hinsberg WHMC-V, Verhoef JC, Bodde HE 1994. Transdermal iontophoresis of peptides and proteins: transport kinetics and electrical skin properties. Drug Targeting Delivery 3(DRUG ABSORPTION ENHACEMENT):199-220.

13. Lide DR editor 1990. CRC handbook of chemistry and physics. 71st ed.: CRC Press (Taylor & Francis, Manhattan, New York, NY).

14. Li SK, Ghanem AH, Peck KD, Higuchi WI 1998. Characterization of the transport pathways induced during low to moderate voltage iontophoresis in human epidermal membrane. J Pharm Sci 87(1):40-48.

15. Deen WM 1987. Hindered transport of large molecules in liquid-filled pores. A I Ch E Journal 33(9):1409-1425.

16. Cottet H, Gareil P, Theodoly O, Williams CE 2000. A semi-empirical approach to the modeling of the electrophoretic mobility in free solution: application to polystyrenesulfonates of various sulfonation rates. Electrophoresis 21(17):3529-3540.

17. Cottet H, Gareil P 2000. From small charged molecules to oligomers: a semiempirical approach to the modeling of actual mobility in free solution. Electrophoresis 21(8):1493-1504.

18. Böhme U, Scheler U 2007. Hydrodynamic size and electrophoretic mobility of poly(styrene sulfonate) versus molecular weight. Macromolecular Chemistry and Physics 208(19-20):2254-2257.

19. Pikal M 1990. Transport mechanisms in iontophoresis. I. A theoretical model for the effect of electroosmotic flow on flux enhancement in transdermal iontophoresis. Pharm Res 7(2):118-126.

20. Pikal M 1990. Transport mechanisms in iontophoresis. III. An experimental study of the contributions of electroosmotic flow and permeability change in transport of low and high molecular weight solutes. Pharm Res 7(3):222-229.

21. Pikal M, Shah S 1990. Transport mechanisms in iontophoresis. II. Electroosmotic flow and transference number measurements for hairless mouse skin. Pharm Res 7(3):213-221.

22. Pikal M 2001. The role of electroosmotic flow in transdermal iontophoresis. Adv Drug Deliv Rev 46:281-305.

23. Sims SM, Higuchi WI, Srinivasan V 1991. Interaction of electric field and electro-osmotic effects in determining iontophoretic enhancement of anions and cations. Int J Pharm 77:107-118.

24. Sims SM, Higuchi WI, Srinivasan V, Peck KD 1993. Ionic partition coefficients and electroosmotic flow in cylindrical pores: comparison of the predictions of the Poisson-Boltzmann equation with experiment. J Colloid and Interfacial Sci 155:210-220.

25. Hirvonen J, Guy RH 1998. Transdermal iontophoresis: modulation of electroosmosis by polypeptides. J Control Release 50:283-289.

CHAPTER 4

IONTOPHORESIS OF SMALL IONS WITH COTRANSPORT OF POLYSTYRENE SULFONATE OLIGOMERS

4.1 Introduction

The iontophoretic delivery and extraction of small charged molecules across the epidermal membrane has been studied extensively by various authors.[1-8] In previous studies we have shown that the cotransport of polystyrene sulfonate (PSS) increased the cathodal flux of nonionic molecules across hairless mouse skin (HMS) by up to six times the rate observed in baseline studies where the media in both the cathodal and anodal chambers was 0.1 M ionic strength phosphate buffered saline (PBS) (see Chapter 3). The purpose of the current study is to investigate the effect that the cotransport of PSS has on the fluxes of small anionic and cationic probe permeants using HMS as the model membrane. Understanding the effect that the cotransport of polymeric anions has on the transport properties of skin may lead to new approaches to enhance and better control the delivery and/or extraction of therapeutically relevant molecules across the skin.

The following strategy was used to quantify changes in the transport of small ionic permeants during HMS iontophoresis experiments with PSS in the cathodal chamber: (i) measure the iontophoretic permeability coefficients of anionic and cationic probe permeants and compare these to baseline results with the same; (ii) evaluate the effect that changes in the concentration of sodium PSS in the cathodal chamber have on

the flux of small anions and cations; (iii) use theoretical Nernst-Planck calculations to investigate the concentration profiles, flux profiles and electrical potential gradients for an idealized pore pathway having similar transport characteristics as those obtained for HMS in the previous studies; and (iv) use theoretical Nernst-Planck calculations to compare theoretical and experimental permeability coefficients for the transport of the small ions in this system.

4.2 Materials and Methods

4.2.1 Materials

Radiolabeled permeants [^{14}C] Salicylate (SA), [^{3}H] taurocholate (TC), [^{36}Cl] isotopic chlorine, [^{14}C] tetraethylammonium (TEA) bromide, and [^{3}H] tetraphenylphosphonium (TPP) bromide were obtained from American Radiolabeled Chemicals (St. Louis, MO). [^{22}Na] isotopic sodium was obtained from Perkin Elmer Life Sciences (Boston, MA). Radiolabeled chemicals had an advertised purity of $\geq$ 98%. The purity of the radiolabeled compounds was verified via HPLC before and after selected experiments. The diffusion coefficient and molecular radius of the isotopic and radiolabeled permeants were previously determined in baseline experiments (see Chapter 2 for details). Chemicals used to prepare buffer and polyelectrolyte solutions were reagent grade and purchased from Sigma-Aldrich Company (St. Louis, MO), unless otherwise specified. Solutions were prepared using deionized water that was filtered using a Milli-Q® filtration system (Resistivity > 10 MΩ·cm: Millipore Corp., Billerica, MA). 0.1 M ionic strength phosphate buffered saline (0.013 M total phosphate; 0.077 M NaCl) with 50 mg/L gentamicin added as a preservative was prepared and the solution

pH was adjusted to pH 7.4. Liquid silver paint was obtained from Ladd Research Industries (Williston, VT). Silver foil and other laboratory supplies were obtained from VWR Inc. (West Chester, PA).

Sodium polystyrenesulfonate calibration standard (sodium PSS; Mp=1370, Mw=1430 and Mn=1200) was obtained from American Polymer Standards (Mentor, OH). Solutions containing sodium PSS were prepared by mixing an appropriate amount of dry sodium PSS powder with deionized water. For the highest concentration of sodium PSS (137 mg/mL) investigated, it was necessary to adjust the pH of the PSS solutions to pH 7 using a 50% w/w solution of NaOH (typically < 30 μL was required to neutralize 2 mL of the highest concentration sodium PSS solutions).

4.2.2 HMS iontophoresis experiments with sodium PSS in the cathodal chamber

After sacrificing the animals, sections of skin were removed from the abdomen of female hairless mice (strain SKH1-hr, ≥ 12 weeks old from Charles River, Wilmington, MA). HMS samples were placed between the two halves of the diffusion cell (volume of each half cell = 2 mL; diffusional area = 0.95 cm^2) and allowed to equilibrate with PBS on both sides of the membrane for 1.5 hours. To determine the initial resistance of the HMS, R_{init}, 100 mV was applied across the sample and the resulting current was measured using a four-electrode potentiostat system (JAS Instrument Systems Inc., Salt Lake City, UT); Ohm's law was then used to calculate R_{init} of the membrane. Only those HMS samples with $R_{init} \geq 25\ k\Omega \cdot cm^2$ after equilibration were used for the iontophoresis experiments. After measuring the initial resistance of the membrane, the PBS solution

was removed from the half cell facing the stratum corneum (cathodal chamber), and the stratum corneum side of the membrane and the cathodal chamber were rinsed repeatedly with deionized water for 30 minutes. At the end of the rinse period, the selected sodium PSS solution was added to the cathodal chamber and the iontophoresis experiments were conducted. The entire diffusion cell assembly was submersed in a constant temperature water bath. The temperature of the bath was maintained at 37 ± 1ºC. See Figure 3.1 for a full description of the experimental setup used. As in experiments with nonionic probe permeants, a salt bridge was used to separate the chamber that the cathode was placed in from the chamber containing sodium PSS solutions.

Iontophoresis experiments were conducted using anionic or cationic probe permeant pairs. Probe permeants were grouped in pairs of anionic or cationic permeants in an effort to minimize the number of experiments required. In the case of experiments with cationic permeant pairs the anodal chamber was filled (2.0 mL) with the pre-mixed solution of PBS containing trace amounts (0.25 – 1.0 μCi/mL) of the isotopic or radiolabeled probe permeant pairs and the cathodal chamber was filled (2.0 mL) with a selected sodium PSS solution. When experiments with anionic permeant pairs were conducted, the cathodal chamber was filled with a pre-mixed sodium PSS solution containing trace amounts (0.25 – 1.0 μCi/mL) of the isotopic or radiolabeled anionic probe permeant pairs while the anodal chamber was filled with PBS. A constant current of 0.11 ± 0.01 mA/cm^2 was applied to the HMS using a constant current iontophoresis device (Phoresor II Auto, Model PM 850, Iomed, Inc., Salt Lake City, UT) via silver foil and Ag/AgCl electrodes placed in the anodal and cathodal chambers. The ‘donor’

chamber refers to the half cell containing the isotopic or radiolabeled probe permeant pair, while the other half cell becomes the 'receiver'; therefore the designation of the donor and receiver chambers depended on whether the probe permeant was cationic or anionic. In a typical iontophoresis experiment, samples were taken from the receiver chamber and donor chamber for up to 6 hours. Receiver samples were replaced by an equivalent volume of fresh PBS or sodium PSS solution depending on the permeant pair being investigated. All samples were mixed with 10 mL of scintillation cocktail (Ultima Gold™, PerkinElmer, Waltham, MA) and were assayed by liquid scintillation counting (Packard TriCarb™ Model 1900TR Liquid Scintillation Analyzer, PerkinElmer, Waltham, MA) using a dual counting protocol. After radio scintillation counting, the following equation was used to calculate the experimental permeability coefficient ($P_{ion,exp}$) of the ionic permeants.

$$P_{ion,\exp} = \frac{1}{AC_D}\frac{\Delta Q}{\Delta t} \tag{4.1}$$

where A is the area of the membrane (A = 0.95 cm^2 for all of the experiments), C_D is the concentration of the permeant in the donor chamber, and $\Delta Q/\Delta t$ is the slope of the receiver cumulative amount vs. time plot (only the steady-state region where r-squared > 0.98 was used to calculate $P_{ion,exp}$). $P_{ion,exp}$ can be regarded as the flux ($J_{ion,exp}$) normalized by the concentration of permeant in the donor chamber ($P_{ion,exp} = J_{ion,exp}/C_D$). The linear region of the receiver cumulative amount vs. time plot generally consisted of data collected when $t \geq$ 2 hours. The voltage across the membrane was monitored throughout

the experiments. Voltage measurements recorded in the linear region of the cumulative amount of permeant vs. time plot were averaged and compared to the theoretical voltage from theoretical Nernst-Planck calculations.

4.2.3 Theoretical considerations

The modified Nernst-Planck model (MNP), has been used previously to analyze the steady-state fluxes of ionic and nonionic permeants across HMS under low to moderate voltage iontophoresis conditions (see Chapter 2). The following equation was used for theoretical Nernst-Planck calculations.

$$J_{ion,theor} = \varepsilon' \left\{ -HD\left[\frac{dC}{dx} + \frac{CzF}{RT}\frac{d\psi}{dx} \right] \pm WvC \right\} \tag{4.2}$$

where ε' is effective porosity of the membrane ($\varepsilon' = \varepsilon/\tau$, with ε is defined as the fraction of the total membrane area available for transport and τ is the tortuosity of the pathway), H is the hindrance factor for simultaneous diffusion and electromigration, D is the diffusion coefficient of the permeant in the bulk media, C is the concentration at a given location in the membrane, z is the charge of the ion, F is Faraday's constant, R is the universal gas constant, T is temperature, ψ is the electric potential, W is the hindrance factor for permeant transport driven by convective solvent flow, and v is the velocity of the convective solvent flow. Both W and H are functions of the effective pore radius (Rp) and the permeant radius (r). The hindrance factors W and H have been discussed extensively in the literature and related information regarding their derivation and various forms of the equations can be found in the literature.[9] In previous studies the integrated

form of Eq. 4.2 has been used to calculate *Rp* of transport pathways available to both ionic and nonionic permeants during transdermal iontophoresis (see Chapter 2).

In order to use Eq. 4.2 as a basis for calculating *Rp* in the baseline HMS study with 0.1 M PBS in both the anodal and cathodal chambers, it was sufficient to assume that the potential gradient was constant across the pore pathway. This greatly simplified the calculations as the integrated form of Eq. 4.2 may be employed in this case (see Chapter 2). Li et. al recently conducted transscleral iontophoresis experiments employing rabbit eye tissues and investigated the situation where both the ions and their concentrations in the two chambers were different.[10] In their theoretical analysis employing Eq. 4.2, these authors were able to assume that $WvC \approx vC$ as (a) the average pore size for the sclera is quite large compared to that of the stratum corneum and (b) v was determined experimentally using mannitol as a nonionic probe and the two probe ions in their study were salicylate and tetraethylammonium, both possessing sizes comparable to mannitol.

In the present case, the situation is, in one sense, similar to that of Li et al., i.e. an asymmetric system. However, it importantly differs in that the assumption of $WvC \approx vC$ was not tenable both because of the small pore size of the stratum corneum and the wide range of permeant sizes. Following is a description of the methods used to create the computer model that would allow for the theoretical analysis of the iontophoresis system described above.

4.2.3.1 Computer modeling of ion transport in an aqueous pore pathway

In order to model the transport of ions in the pore pathways of the epidermal membrane we have adapted a computer modeling approach that has been used previously to model capillary electrophoresis (CE), a common electrophoretic separation technique used in analytical chemistry. The model used was originally developed for use with COMSOL Multiphysics® software (Comsol, Inc., Burlington, MA).[11] In order to apply the CE model to the transport pathways available to ions in HMS some simplifying assumptions were made regarding the pore pathway of the epidermal membrane. First, the length of the capillary was equated to the thickness of the stratum corneum of HMS (assumed to be 15 μm; values given in the literature range from 10 – 25 μm[6,12,13]) and the pathway was treated as a right, circular cylinder with the hindered transport parameter, H in Eq. 4.2, used for both the electrophoretic and the diffusive transport of ions in the pore pathway. Second, a single representative pore was used to model the transport pathway of ions across the membrane. The current density in the pore was calculated by dividing the experimental current density of 0.11 mA/cm^2 (which was also the same as that in the baseline experiments) by the effective porosity ($\varepsilon' = 2.1 \times 10^{-5}$; the effective porosity was determined previously in baseline experiments; see Chapter 2). The calculated current density of the pore was 5.26×10^3 mA/cm^2, which was held constant for all of the theoretical Nernst-Planck calculations. Third, in order to reduce the total number of ions in the system and to avoid the added complexity of including ionization constants in the model, phosphate ions were excluded from the theoretical calculations. As sodium and

chloride ions account for most of the ions making up the PBS solution in the anodal chamber, 90 mM sodium chloride was used to represent PBS in the anodal chamber for all of the theoretical Nernst-Planck calculations and the calculations conducted for 1 mM, 10 mM, or 100 mM sodium PSS in the cathodal chamber (corresponding to 1.37 mg/mL, 13.7 mg/mL, and 137 mg/mL sodium PSS, respectively; calculated based on the reported peak molecular weight of the polymer). The concentration of probe permeants in the Nernst-Planck calculations was an arbitrarily chosen low value of 10^{-3} mM. Table 4.1 shows the relevant transport parameters for each of the trace permeant ions used in the theoretical Nernst-Planck calculations. The ^{36}Cl and the ^{22}Na parameters of Table 4.1 were also used for the "cold" sodium and chloride ions in the theoretical Nernst-Planck calculations. Finally, since the sodium PSS solution was composed of a mixture of PSS oligomers of varying lengths and concentrations, the theoretical Nernst-Planck calculations were performed with PSS oligomers treated as a single species having an effective charge (z_{eff}) of -7 and a hydrodynamic radius equal to that of the heptamer (see Table 3.3).

4.2.3.2 Determination of Wv to be used in Eq. 4.2

As mentioned above (section 4.2.3) the condition, $WvC \approx vC$, would not be tenable in the present situation. It was therefore decided to obtain estimates of Wv for each of the ions by using the transport data from previously conducted experiments with nonionic permeants (see Chapter 3) and finding by interpolation the nonionic permeant Wv value that would correspond to that of the permeant ion of interest. For nonionic

Table 4.1. Relevant transport parameters for the permeant ions used in theoretical Nernst-Planck calculations.

Permeant ion	z_{eff}	D (10^{-6} cm^2/s)	r (Å)[a]	Wv (10^{-2} cm/s)[b]		
				100 mM PSS	10 mM PSS	1 mM PSS
^{36}Cl	-1	28.0	1.9	8.2	7.7	9.7
[^{14}C]-Salicylate	-1	12.7	3.2	5.1	4.9	5.2
[^{3}H]-Taurocholate	-1	5.7	6.1	3.6	3.6	3.0
PSS heptamer	-7	4.4	7.5	2.9	2.9	2.0
^{22}Na	+1	17.6	2.5	6.1	5.8	6.7
[^{14}C]-TEA	+1	11.8	3.4	4.9	4.7	4.9
[^{3}H]-TPP	+1	4.9	6.9	3.4	3.4	2.7

[a] The solute radius shown in the table, r, was calculated using Eq. 2.3 where R_{SE} is the Stokes-Einstein radius calculated from Eq. 2.2.

[b] Wv was calculated at each sodium PSS concentration investigated from plot of $P_{nonionic}$ versus the respective diffusion coefficients of the nonionic permeant investigated previously (see Chapter 3).

permeants, the flux is

$$J_{nonionic} = \varepsilon' \left[-HD\frac{dC}{dx} \pm WvC \right] \tag{4.3}$$

Since the transport of nonionic permeants was found to be enhanced up to sixfold relative to baseline studies, it was assumed that $HD\frac{dC}{dx} << WvC$ in Eq. 4.3. As the concentration of the nonionic permeant in the membrane is expected to be relatively constant across the membrane (except near the interface of the receiver compartment) and equal to the concentration in donor compartment, i.e. $C_i \approx C_D$ in Eq. 4.3, Wv was obtained by using the relationship,

$$Wv = \frac{P_{nonionic}}{\varepsilon'} \tag{4.4}$$

where $P_{nonionic} \approx J_{nonionic}/C_D$. In the previous study (Chapter 3) the permeability coefficients of nonionic permeants were plotted versus their respective diffusion coefficients (see Figure 3.4) and this plot was used to interpolate for the $P_{nonionic}$ value corresponding to that of the ionic probe permeant of interest (i.e. the $P_{nonionic}$ value of the hypothetical nonionic permeant having the same diffusivity as that of an ionic permeant of interest). Eq. 4.4 was then used, along with the effective porosity, to calculate the value of $W_i v_i$ for each of the ionic probe permeants used in the present study. Values of $W_i v_i$ for each of the ions in the system are shown in Table 4.1.

4.2.3.3 Calculation of permeability coefficient from Nernst-Planck theory

One of the main purposes of the theoretical Nernst-Planck calculations was to find the appropriate effective pore radius where the theoretical calculations would be in best agreement with the results obtained from iontophoresis experiments with ionic permeants. In order to compare the theoretical permeability coefficient, $P_{ion,theor}$, with the experimental permeability coefficient, $P_{ion,exp}$, the following equation was used to calculate , $P_{ion,theor}$:

$$P_{ion,theor} = \frac{\varepsilon' J_{ion,theor}}{C_D} \tag{4.5}$$

where $J_{ion,theor}$ is the theoretical flux of the ion from Nernst-Planck calculations. Calculating $P_{ion,theor}$ using the method above allowed for direct comparison of the theoretical Nernst-Planck calculations with experimental results.

4.2.3.4 Calculation of the theoretical and experimental transference numbers of the sodium ion and PSS

Comparing the theoretical and experimental transference numbers of the sodium ion and PSS provided an opportunity for direct comparison of the relative experimental and theoretical fluxes of the current determining ions in the system. The theoretical transference numbers ($t_{ion,theor}$) of the sodium ion and PSS were calculated from the theoretical flux values taken from calculations with 100 mM sodium PSS in the cathodal chamber. The following equation was used to calculate $t_{ion,theor}$.

$$t_{ion,theor} = \frac{|z_i| J_i}{\sum_j |z_j| J_j} \tag{4.6}$$

where J_i is the flux of the ionic species i, J_j is the flux of the ionic species j in the system, z_i and z_j represent the charges of the ions in the system.

Eq. 4.7 was used to calculate the experimental transference number ($t_{ion,exp}$).

$$t_{ion,\exp} = P_{ion,\exp} C_D \frac{|z_{eff}| F}{I_{total}} \tag{4.7}$$

The experimental permeability coefficient of the PSS was calculated based on the experimental permeability coefficient of the combined hexamer and heptamer peaks (1.8×10^{-7} cm/s; data presented in Chapter 3). In order to calculate $t_{ion,exp}$ for the sodium ion, the experimental permeability coefficient of the ^{22}Na ion was used under the assumption that the flux behavior of the trace permeant was representative of the cold sodium ion in the system.

4.3 Results

4.3.1 The electric field in the pores and the behavior of the electric current determining ions from theoretical Nernst-Planck calculation results

Figure 4.1(a – d) shows the potential gradient as a function of position from theoretical Nernst-Planck calculations with Rp = 12.5 Å, 15 Å, 30 Å, and 60 Å and with 100 mM, 10 mM, and 1 mM sodium PSS in the cathodal chamber. Figure 4.1(a – d)

shows that the potential gradient varies significantly as a function of position in the pore pathway. However, except for the region very close to the anodal chamber/membrane interface, the potential gradient in the region comprising around 50 – 80% of the left side (i.e., the anodal side of the membrane) is quite constant (i.e., flat) and, except for the smallest pore size case, the potential gradient values are relatively independent of the sodium PSS concentration in the cathodal chamber. At the two membrane interfacial regions, the potential gradient patterns are quite different. At the anodal chamber/membrane interfacial region, except for the smallest pore size case, there is a sharp three-to-fivefold increase in the potential gradient in going from the plateau (flat) region to the interface, the increases in each case being essentially independent of the sodium PSS concentration in the cathodal chamber. A contrasting behavior is seen at the cathodal chamber/membrane interfacial region: as this interfacial region is approached (from left to right in Figure 4.1) the potential gradient changes are strongly dependent on the sodium PSS concentration in the cathodal chamber; for example, in the Rp = 30 Å cases, there is a threefold decrease, a twofold increase, and a seventeenfold increase in the potential gradient in going from the plateau region to the cathodal chamber/membrane interface for the 100 mM, the 10 mM, and the 1 mM sodium PSS cases, respectively. This difference in the potential gradient patterns that is observed between the two interfacial regions may be responsible for the transport behavior differences between the anionic probe permeants and the cationic probe permeants, as will be discussed later. That the potential gradient values in the plateau regions, except for the smallest Rp case, are relatively independent of the sodium PSS concentration in the cathodal chamber, is helpful in later discussions assessing the interplay among the three variables: potential

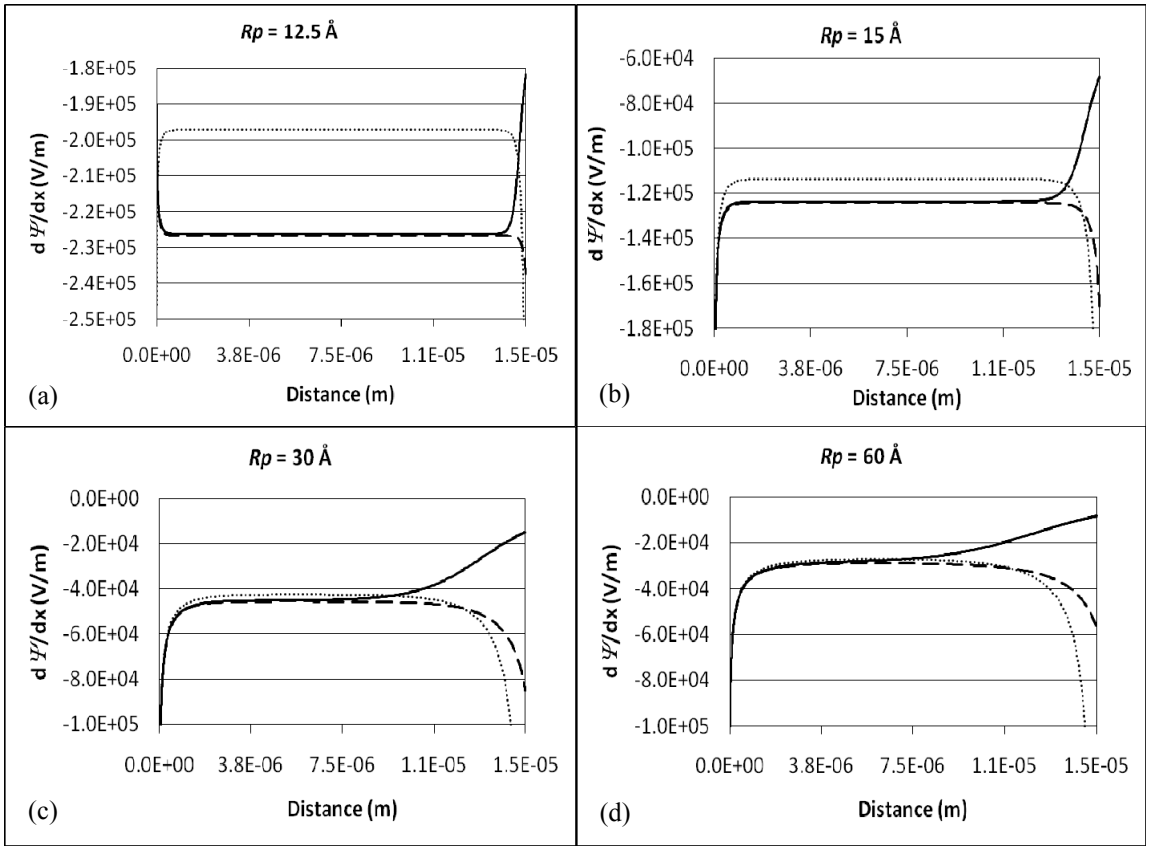

Figure 4.1. Simulated potential gradients plotted as a function of position in the pore with 1 mM (dotted line), 10 mM (dashed line), and 100 mM sodium PSS (solid line) in the cathodal chamber. In all of the theoretical Nernst-Planck calculations 90 mM NaCl was in the anodal chamber. The plots show the results of calculations with (a) *Rp* = 12.5 Å, (b) *Rp* = 15 Å, (c) *Rp* = 30 Å, and (d) *Rp* = 60 Å.

gradient, probe permeant concentration, and flux components (i.e. diffusive, electrophoretic, and convective flux components).

Figures 4.2, 4.3, and 4.4 show the concentration profiles of the sodium, PSS, and chloride ions in the pores, respectively. Interestingly but not surprisingly, over the hundredfold range of PSS concentrations in the cathodal chamber the concentration of the main conducting ions (sodium and PSS) in the midregion of the membrane (from about 30% to 70% of the total path length) remained relatively flat (i.e., constant) and relatively independent of the sodium PSS concentration in the cathodal chamber. Figure 4.4 shows that, except near the anodal chamber/membrane interface, the concentration of chloride ions was negligible over most of the length of the pore pathway.

The diffusive, convective, and electrophoretic components of the fluxes of the dominant current determining ions, sodium and PSS, are shown in Figures 4.5 – 4.10. Plots of the flux components of the current determining ions showed that the diffusive component was negligible over most of the pore path length for all of the calculations. The consistent transport behavior of sodium ion and PSS over the range of sodium PSS concentrations investigated was not surprising given the consistency of the potential gradients (see Figure 4.1) and the concentration profiles (see Figures 4.2 – 4.4) over most of the pore path length.

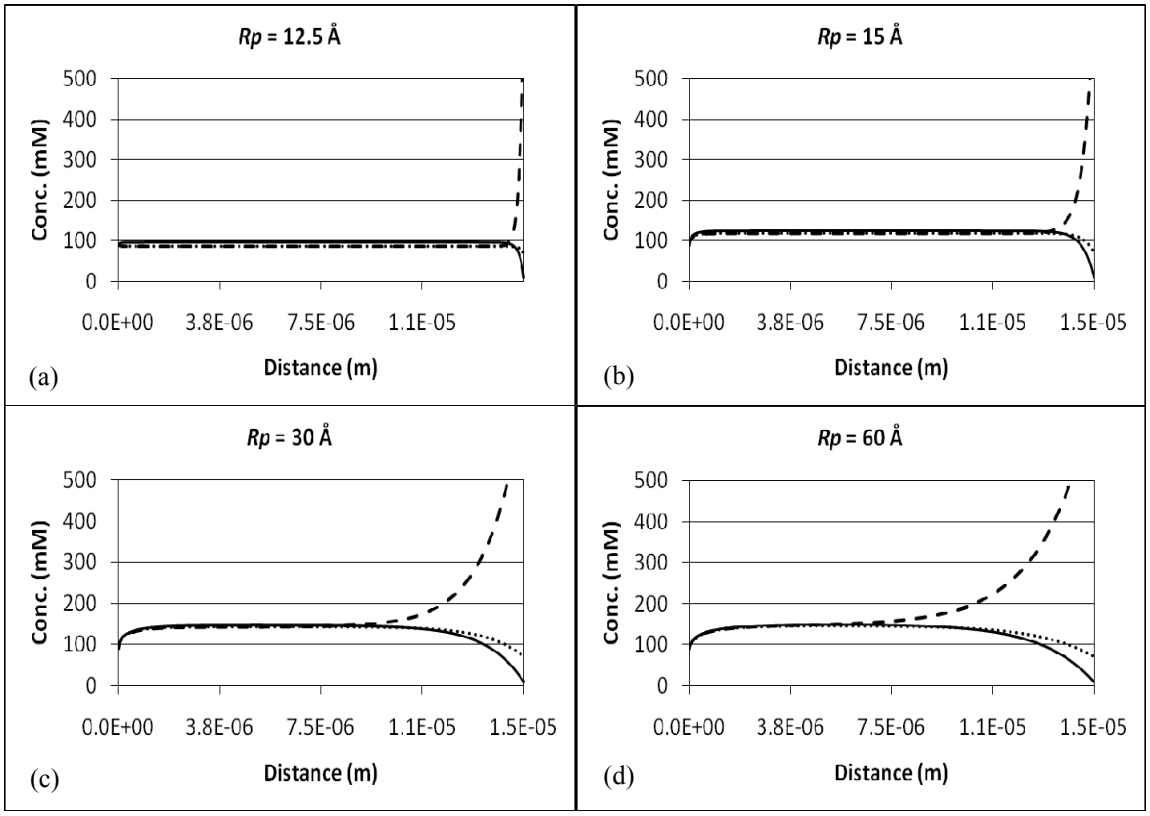

Figure 4.2. Concentration of sodium ion plotted as a function of position in the pore with 1 mM (solid line), 10 mM (dotted line), and 100 mM (dashed line) PSS in the cathodal chamber. The plots show the results of theoretical Nernst-Planck calculations with (a) *Rp* = 12.5 Å, (b) *Rp* = 15 Å, (c) *Rp* = 30 Å, and (d) *Rp* = 60 Å.

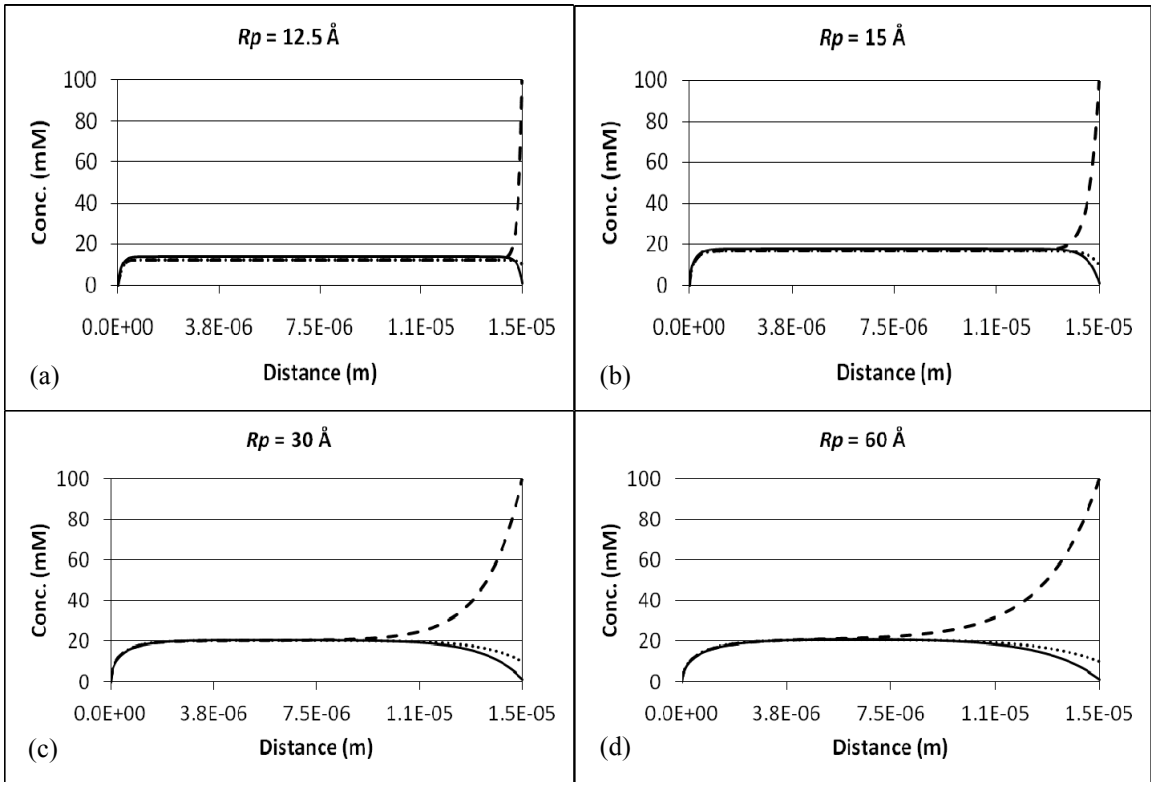

Figure 4.3. Concentration of PSS plotted as a function of position in the pore with 1 mM (solid line), 10 mM (dotted line), and 100 mM (dashed line) PSS in the cathodal chamber. The plots show the results of theoretical Nernst-Planck calculations with (a) *Rp* = 12.5 Å, (b) *Rp* = 15 Å, (c) *Rp* = 30 Å, and (d) *Rp* = 60 Å.

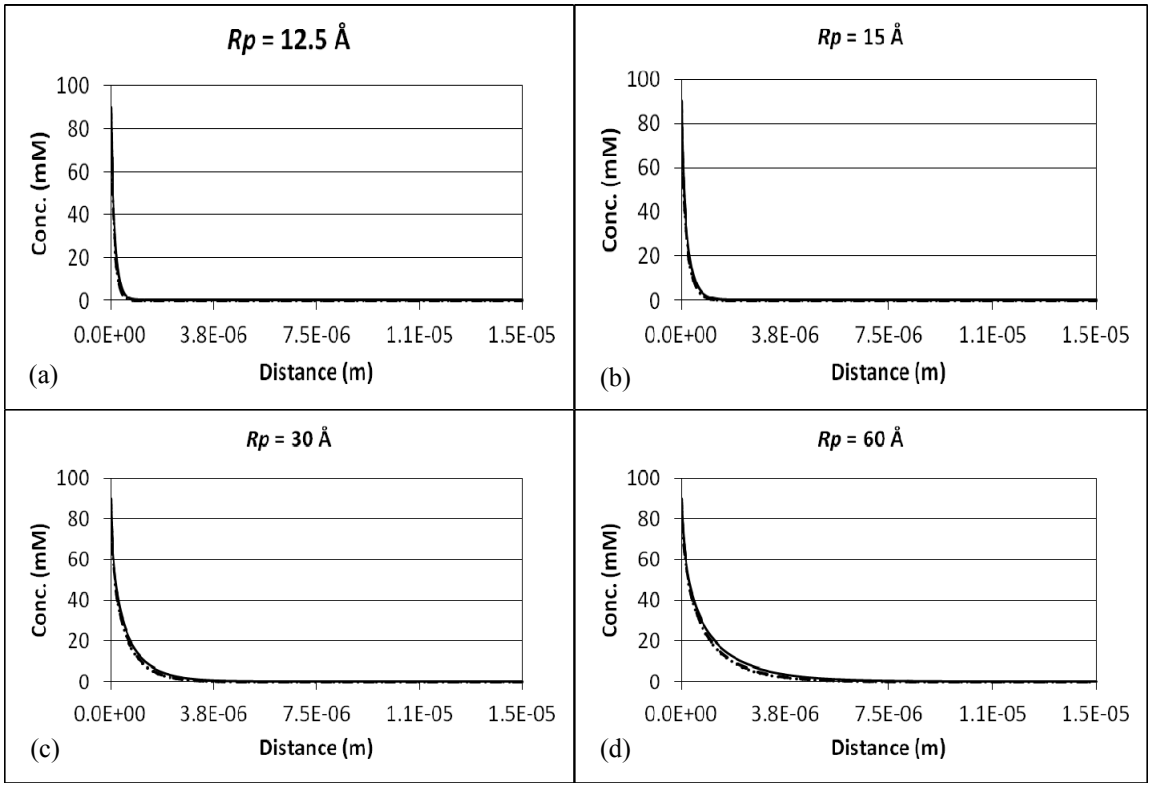

Figure 4.4. Concentration of chloride ion plotted as a function of position in the pore with 1 mM (solid line), 10 mM (dotted line), and 100 mM (dashed line) PSS in the cathodal chamber. The plots show the results of theoretical Nernst-Planck calculations with (a) *Rp* = 12.5 Å, (b) *Rp* = 15 Å, (c) *Rp* = 30 Å, and (d) *Rp* = 60 Å.

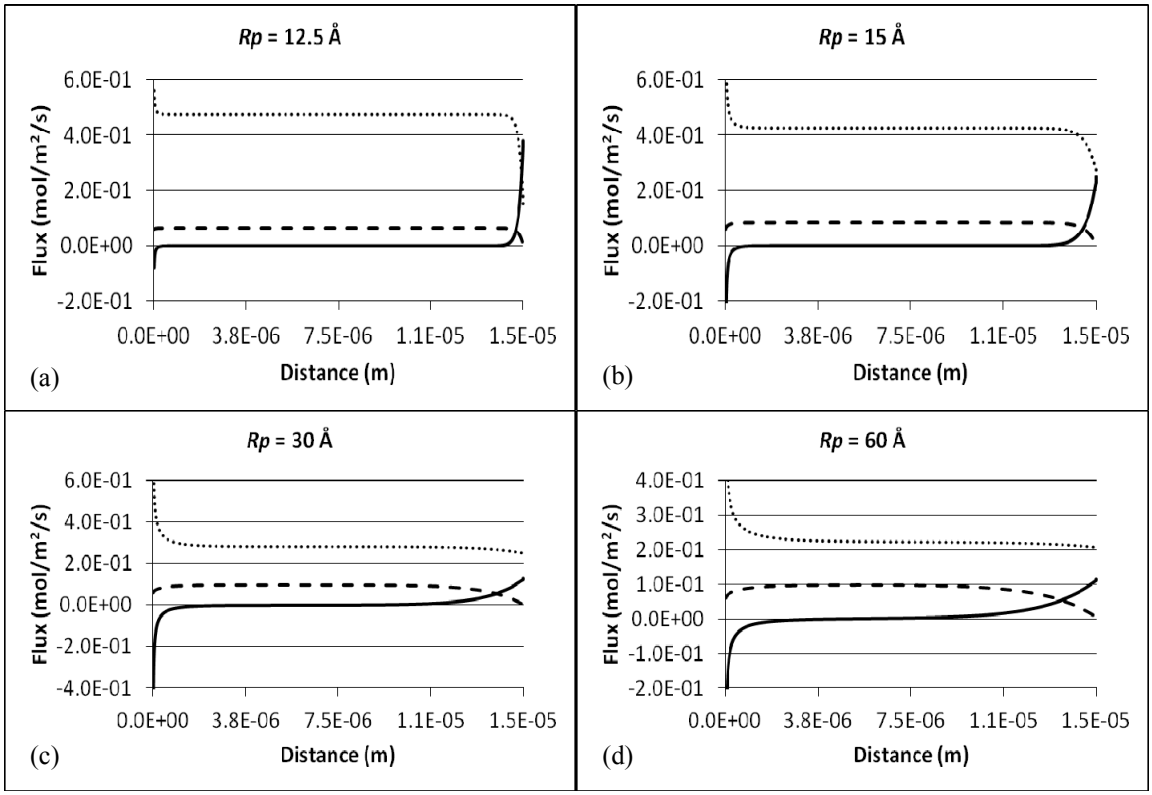

Figure 4.5. Diffusive flux (solid line), convective flux (dashed line), and electrophoretic flux (dotted line) of sodium ion plotted as a function of position in the pore with 1 mM sodium PSS in the cathodal chamber. The plots show the results of theoretical Nernst-Planck calculations with (a) *Rp* = 12.5 Å, (b) *Rp* = 15 Å, (c) *Rp* = 30 Å, and (d) *Rp* = 60 Å.

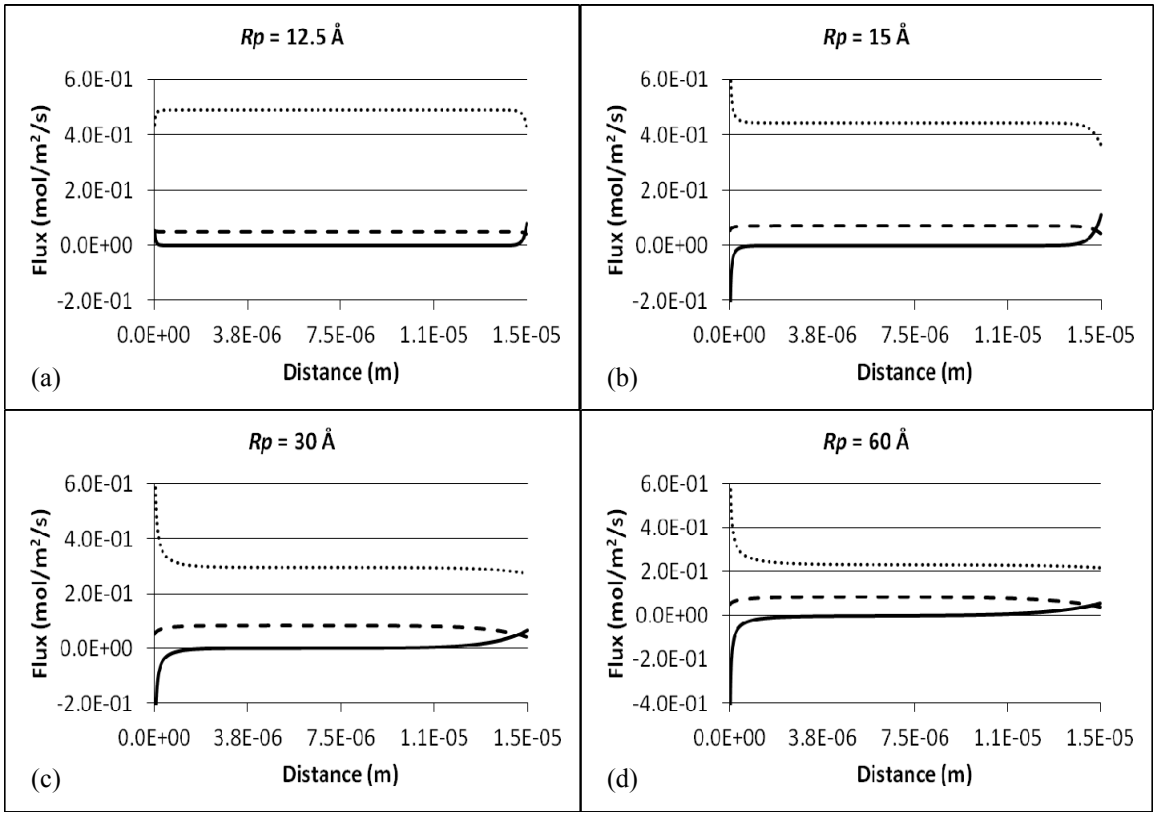

Figure 4.6. Diffusive flux (solid line), convective flux (dashed line), and electrophoretic flux (dotted line) of sodium ion plotted as a function of position in the pore with 10 mM sodium PSS in the cathodal chamber. The plots show the results of theoretical Nernst-Planck calculations with (a) *Rp* = 12.5 Å, (b) *Rp* = 15 Å, (c) *Rp* = 30 Å, and (d) *Rp* = 60 Å.

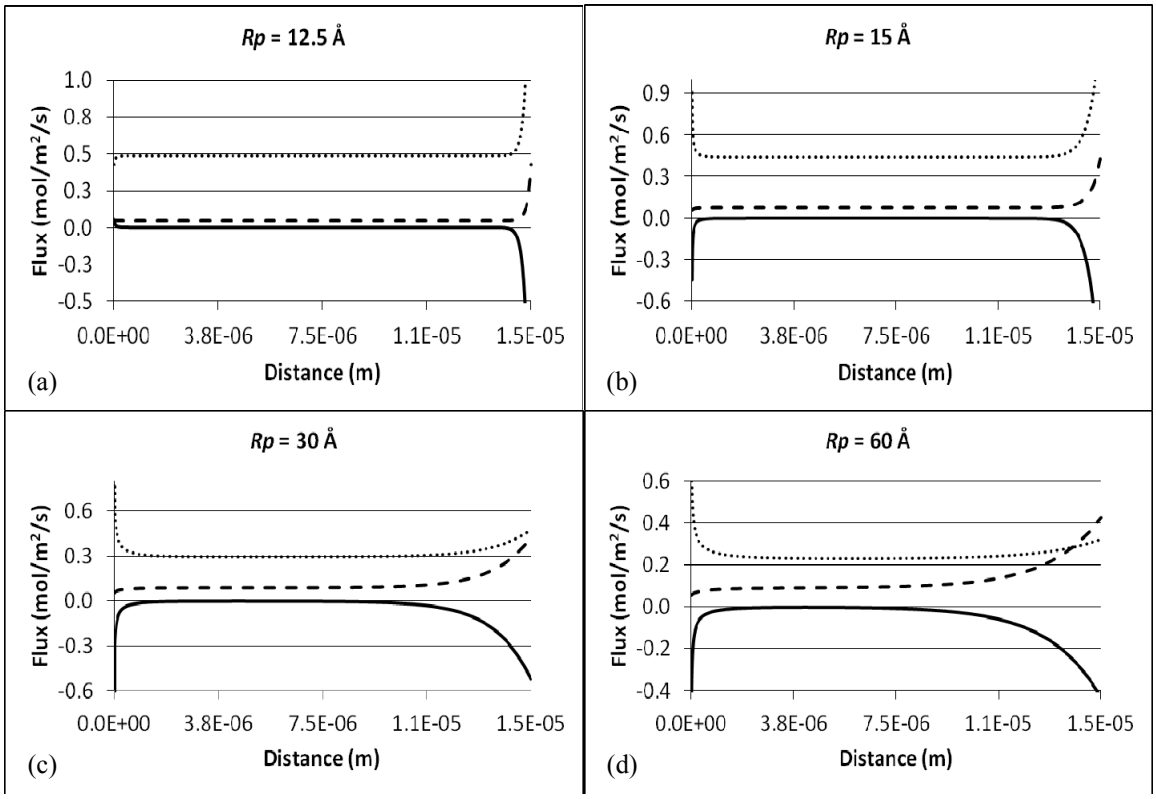

Figure 4.7. Diffusive flux (solid line), convective flux (dashed line), and electrophoretic flux (dotted line) of sodium ion plotted as a function of position in the pore with 100 mM sodium PSS in the cathodal chamber. The plots show the results of theoretical Nernst-Planck calculations with (a) *Rp* = 12.5 Å, (b) *Rp* = 15 Å, (c) *Rp* = 30 Å, and (d) *Rp* = 60 Å.

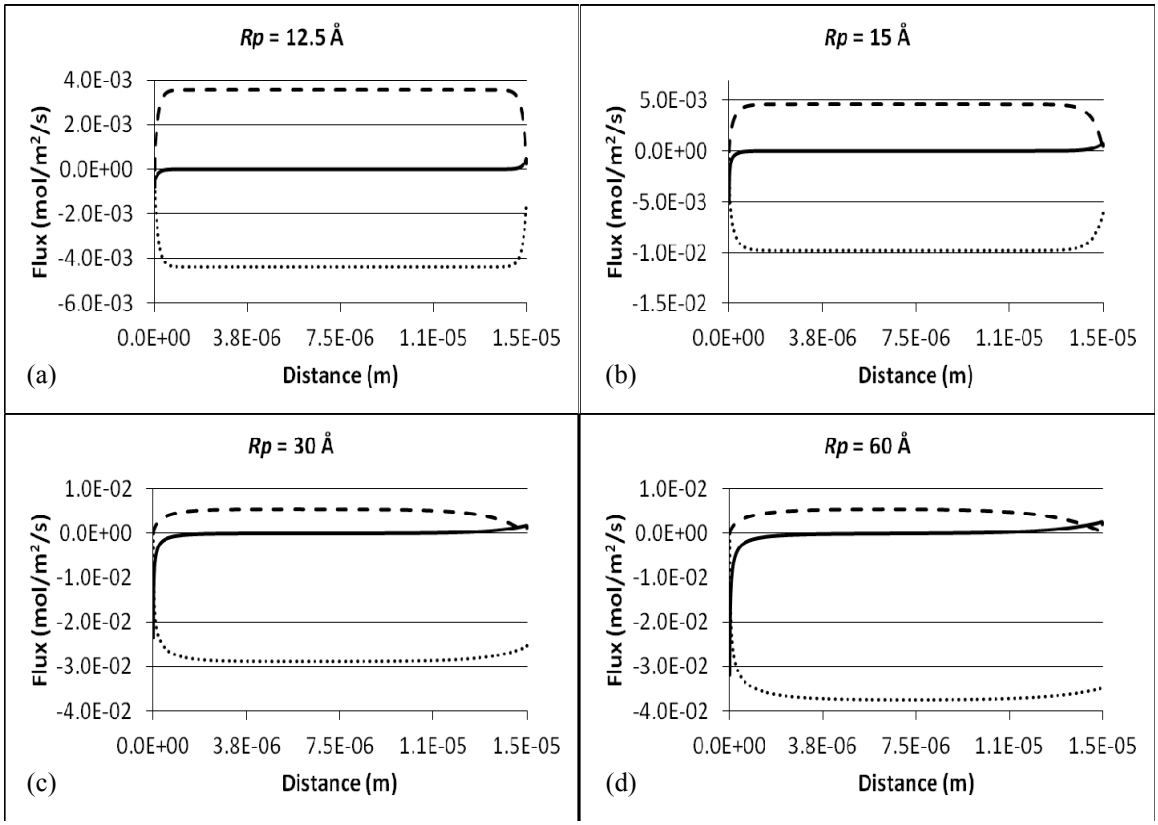

Figure 4.8. Diffusive flux (solid line), convective flux (dashed line), and electrophoretic flux (dotted line) of PSS plotted as a function of position in the pore with 1 mM sodium PSS in the cathodal chamber. The plots show the results of theoretical Nernst-Planck calculations with (a) Rp = 12.5 Å, (b) Rp = 15 Å, (c) Rp = 30 Å, and (d) Rp = 60 Å.

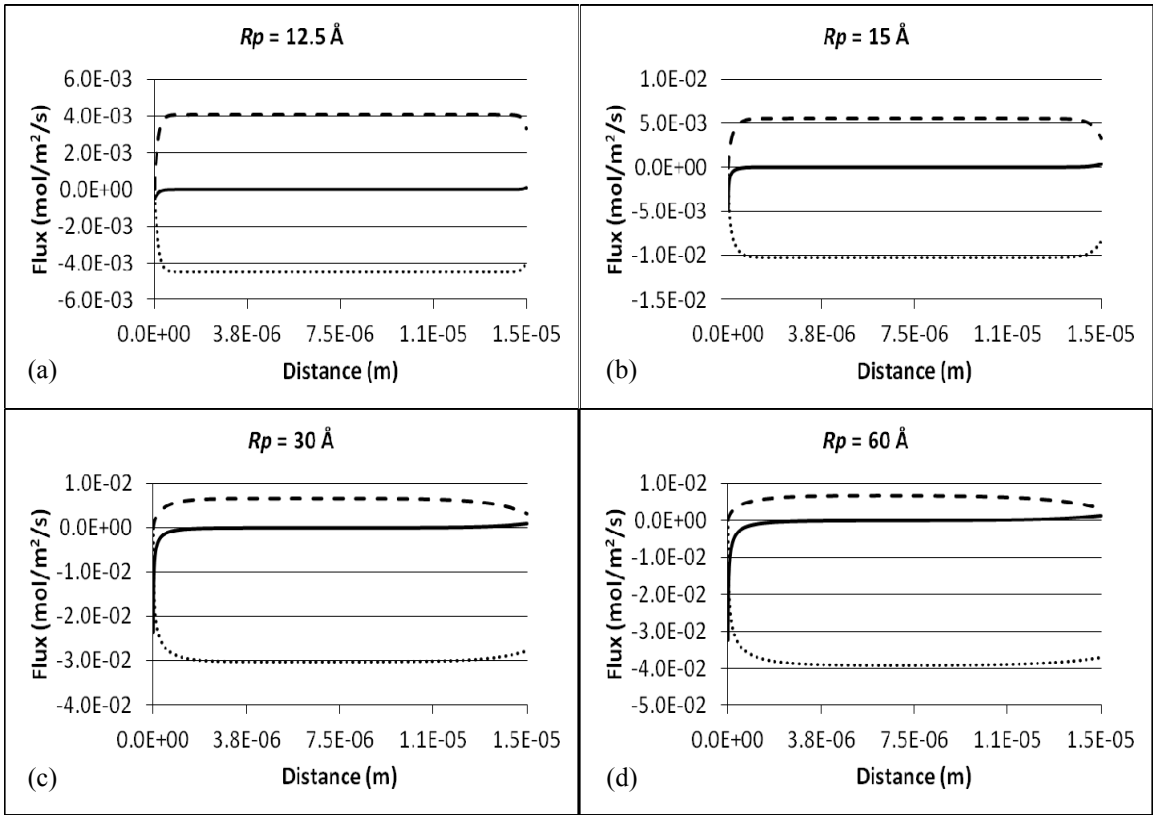

Figure 4.9. Diffusive flux (solid line), convective flux (dashed line), and electrophoretic flux (dotted line) of PSS plotted as a function of position in the pore with 10 mM sodium PSS in the cathodal chamber. The plots show the results of theoretical Nernst-Planck calculations with (a) *Rp* = 12.5 Å, (b) *Rp* = 15 Å, (c) *Rp* = 30 Å, and (d) *Rp* = 60 Å.

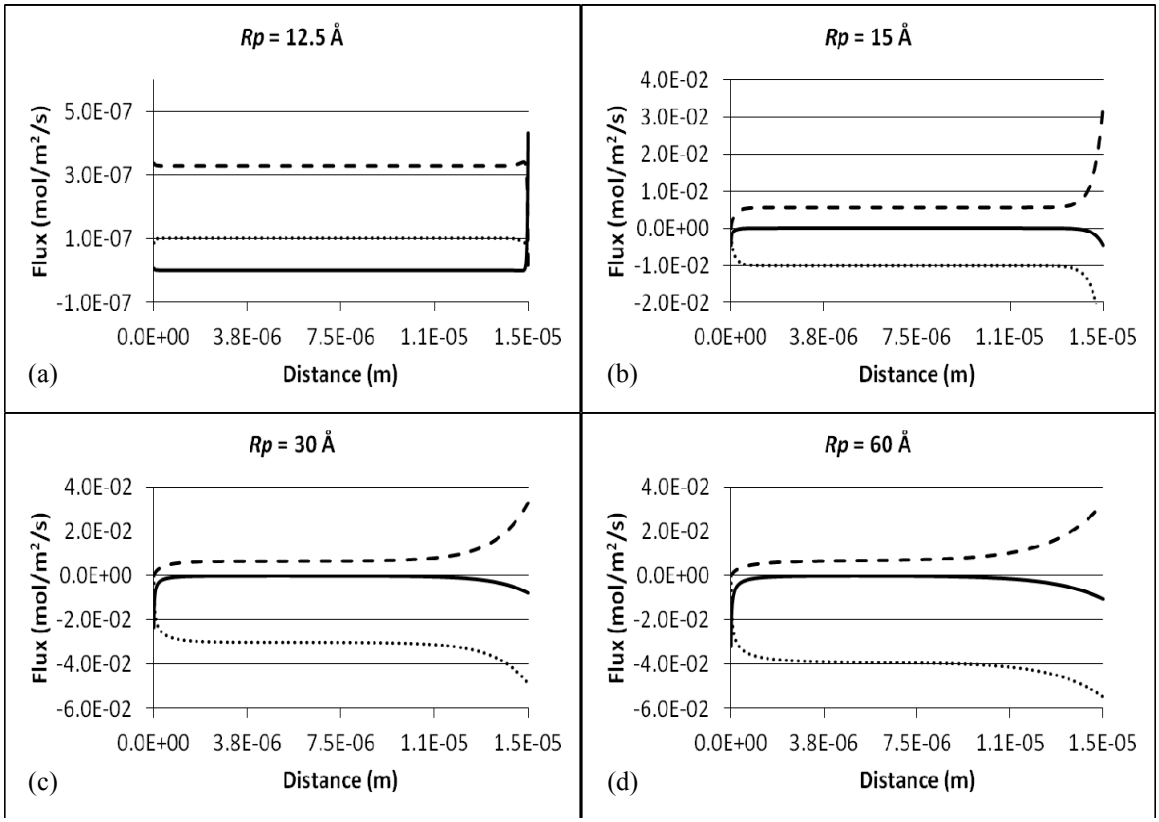

Figure 4.10. Diffusive flux (solid line), convective flux (dashed line), and electrophoretic flux (dotted line) of PSS plotted as a function of position in the pore with 100 mM sodium PSS in the cathodal chamber. The plots show the results of theoretical Nernst-Planck calculations with (a) *Rp* = 12.5 Å, (b) *Rp* = 15 Å, (c) *Rp* = 30 Å, and (d) *Rp* = 60 Å.

4.3.2 Cationic permeants

4.3.2.1 Theoretical results

The concentration profiles of the cationic probe permeants from the theoretical Nernst-Planck calculations are shown in Figures 4.11 – 4.13. The results of theoretical calculations show that the concentrations of the ^{22}Na and TEA ions were essentially superimposable and remained relatively constant over much or most of the pore path length for the three sodium PSS concentrations investigated. The concentrations of the TPP ion were also flat over roughly the same path length and only slightly lower than those of the ^{22}Na and TEA ions. It is important to note that the concentrations of the three cationic probe permeants are relatively independent of the sodium PSS concentration in the cathodal chamber when only the plateau regions are considered.

The diffusive, convective, and electrophoretic components of the fluxes of the cationic probe permeants are shown in Figures 4.14 – 4.22. An important point of interest that can be determined from the plots of Figures 4.14 – 4.22 is the following. For any *Rp* value, both the convective flux and the electrophoretic flux of each cationic probe permeant are relatively independent of the sodium PSS concentration in the cathodal chamber; this is particularly easy to see when only the plateau (flat) regions of the flux profiles are considered: where the potential gradients (Figure 4.1) and the probe permeant concentrations (Figures 4.11 – 4.13) are also in their respective plateau regions. In the plateau regions, the diffusive flux component is essentially zero; therefore, in the plateau regions of the potential gradient and flux component plots the total flux of the probe

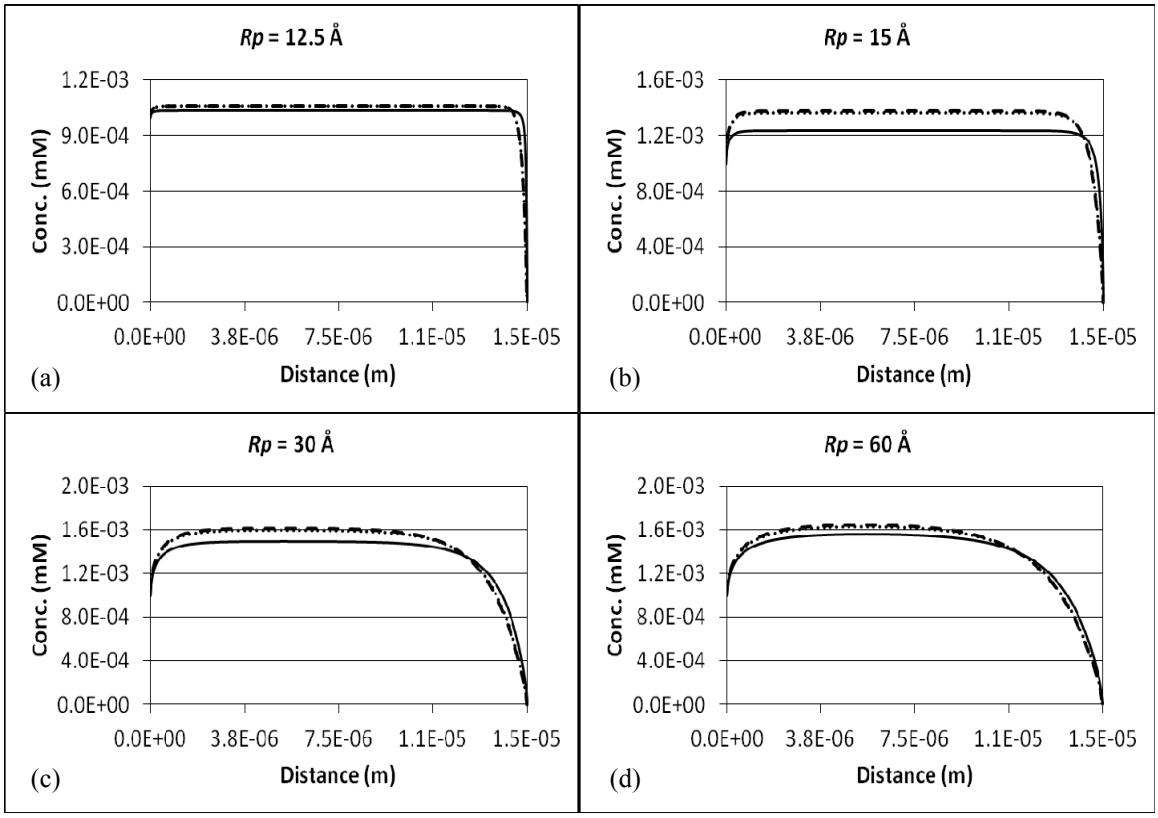

Figure 4.11. Concentrations of the ^{22}Na (dashed line), TEA (dotted line), and TPP (solid line) ions plotted as a function of position in the pore with 1 mM sodium PSS in the cathodal chamber. The plots show the results of theoretical Nernst-Planck calculations with (a) *Rp* = 12.5 Å, (b) *Rp* = 15 Å, (c) *Rp* = 30 Å, and (d) *Rp* = 60 Å.

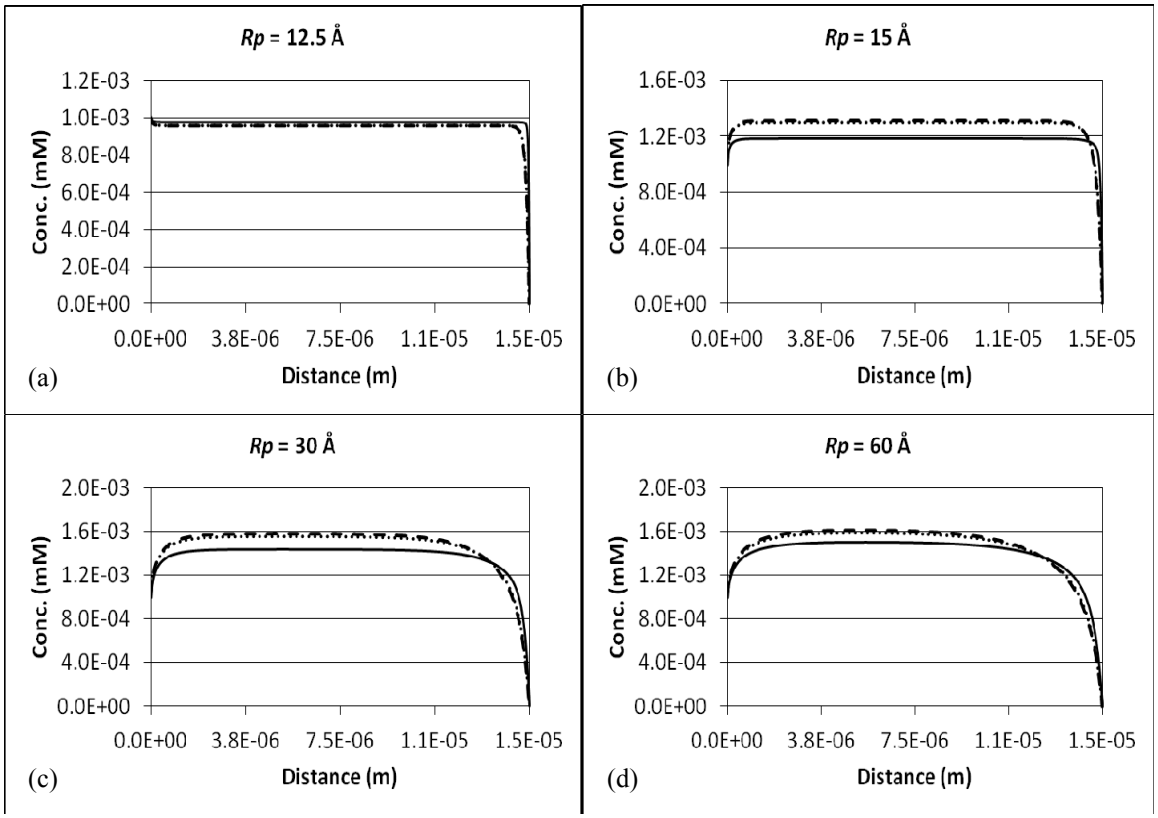

Figure 4.12. Concentrations of the ^{22}Na (dashed line), TEA (dotted line), and TPP (solid line) ions plotted as a function of position in the pore with 10 mM sodium PSS in the cathodal chamber. The plots show the results of theoretical Nernst-Planck calculations with (a) *Rp* = 12.5 Å, (b) *Rp* = 15 Å, (c) *Rp* = 30 Å, and (d) *Rp* = 60 Å.

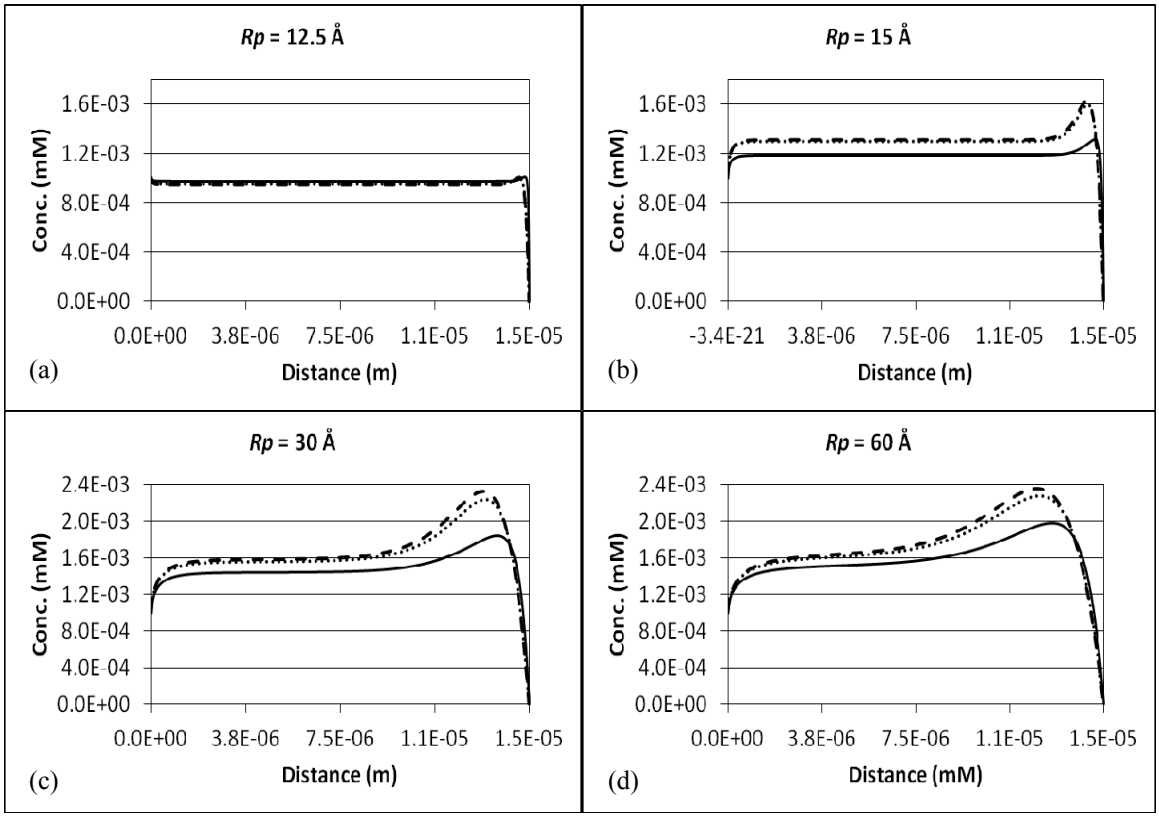

Figure 4.13. Concentrations of the ^{22}Na (dashed line), TEA (dotted line), and TPP (solid line) ions plotted as a function of position in the pore with 100 mM sodium PSS in the cathodal chamber. The plots show the results of theoretical Nernst-Planck calculations with (a) *Rp* = 12.5 Å, (b) *Rp* = 15 Å, (c) *Rp* = 30 Å, and (d) *Rp* = 60 Å.

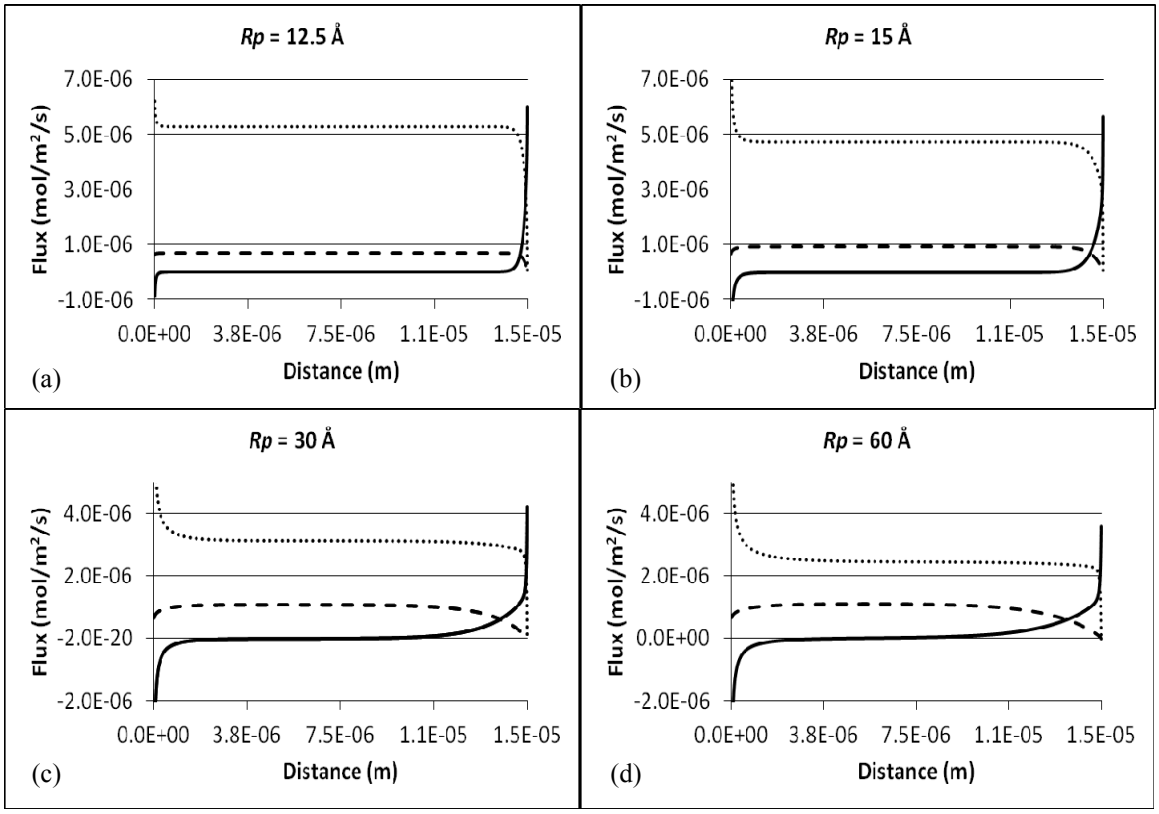

Figure 4.14. Diffusive flux (solid line), convective flux (dashed line), and electrophoretic flux (dotted line) of the ^{22}Na ion plotted as a function of position in the pore with 1 mM sodium PSS in the cathodal chamber. The plots show the results of theoretical Nernst-Planck calculations with (a) *Rp* = 12.5 Å, (b) *Rp* = 15 Å, (c) *Rp* = 30 Å, and (d) *Rp* = 60 Å.

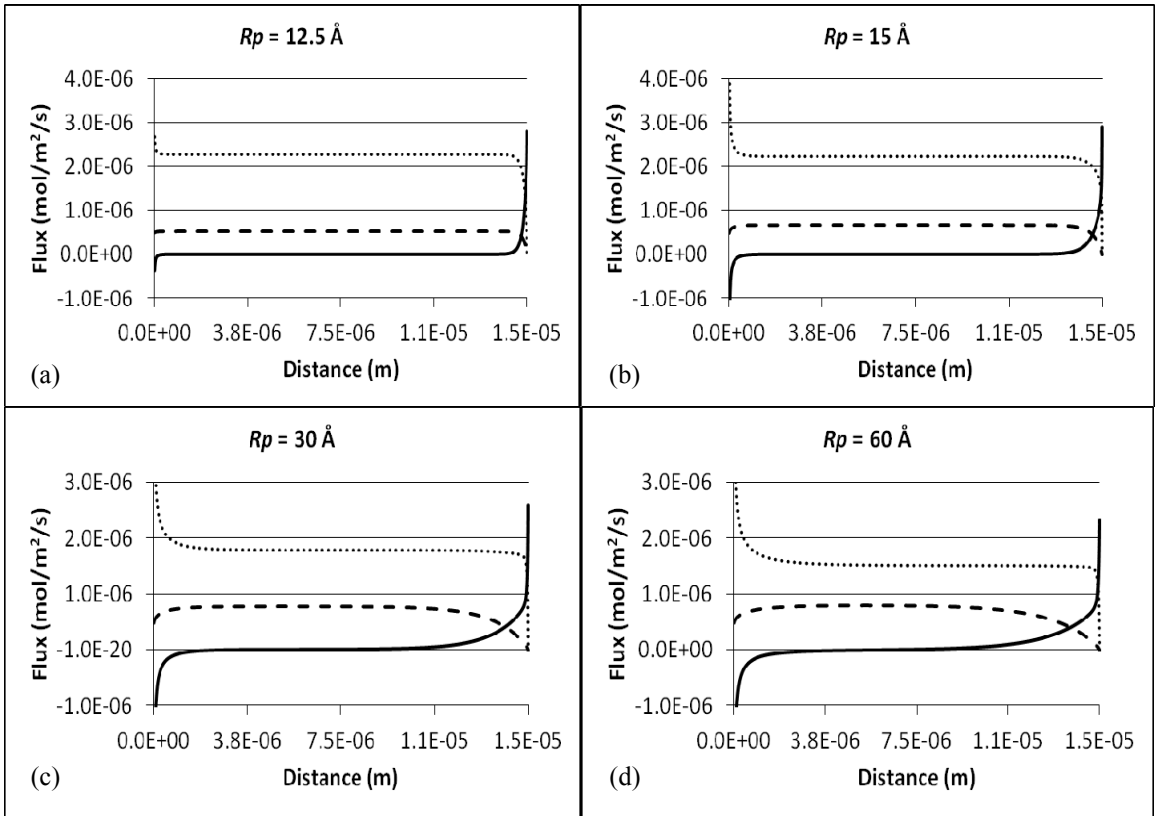

Figure 4.15. Diffusive flux (solid line), convective flux (dashed line), and electrophoretic flux (dotted line) of the TEA ion plotted as a function of position in the pore with 1 mM sodium PSS in the cathodal chamber. The plots show the results of theoretical Nernst-Planck calculations with (a) *Rp* = 12.5 Å, (b) *Rp* = 15 Å, (c) *Rp* = 30 Å, and (d) *Rp* = 60 Å.

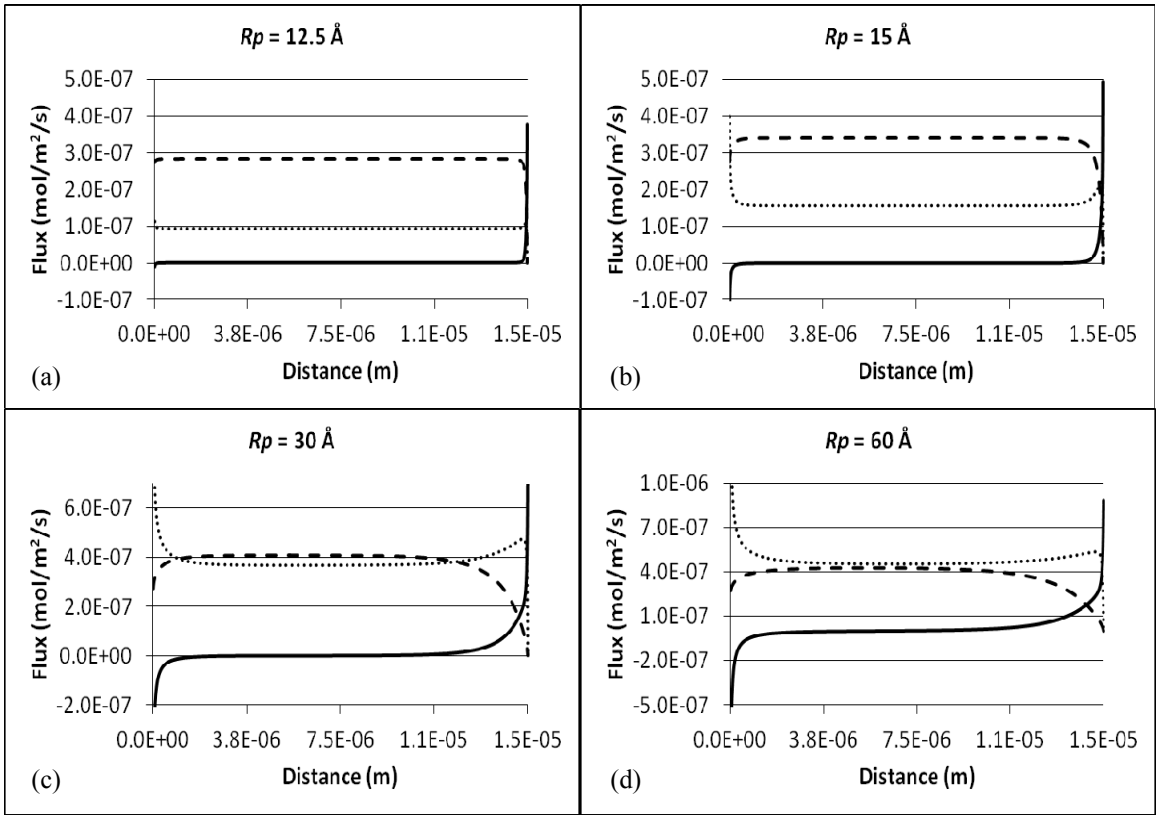

Figure 4.16. Diffusive flux (solid line), convective flux (dashed line), and electrophoretic flux (dotted line) of the TPP ion plotted as a function of position in the pore with 1 mM sodium PSS in the cathodal chamber. The plots show the results of theoretical Nernst-Planck calculations with (a) *Rp* = 12.5 Å, (b) *Rp* = 15 Å, (c) *Rp* = 30 Å, and (d) *Rp* = 60 Å.

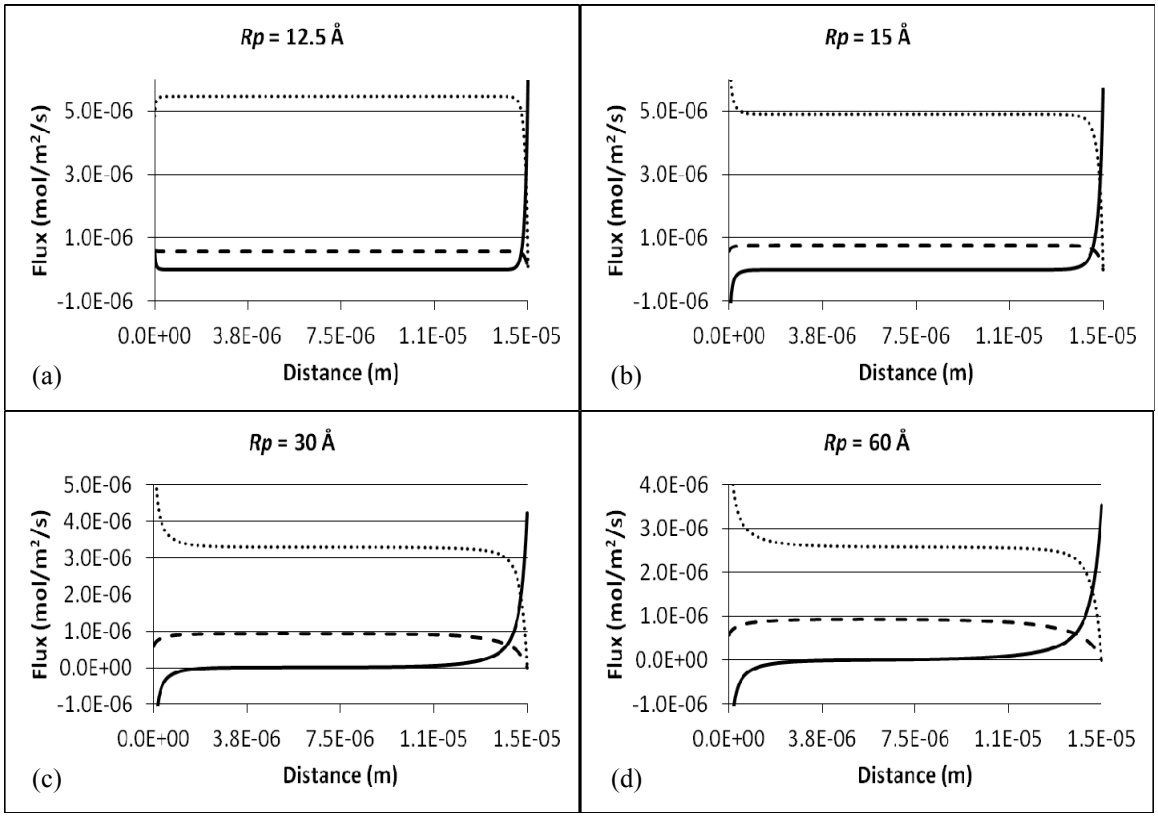

Figure 4.17. Diffusive flux (solid line), convective flux (dashed line), and electrophoretic flux (dotted line) of the ^{22}Na ion plotted as a function of position in the pore with 10 mM sodium PSS in the cathodal chamber. The plots show the results of theoretical Nernst-Planck calculations with (a) *Rp* = 12.5 Å, (b) *Rp* = 15 Å, (c) *Rp* = 30 Å, and (d) *Rp* = 60 Å.

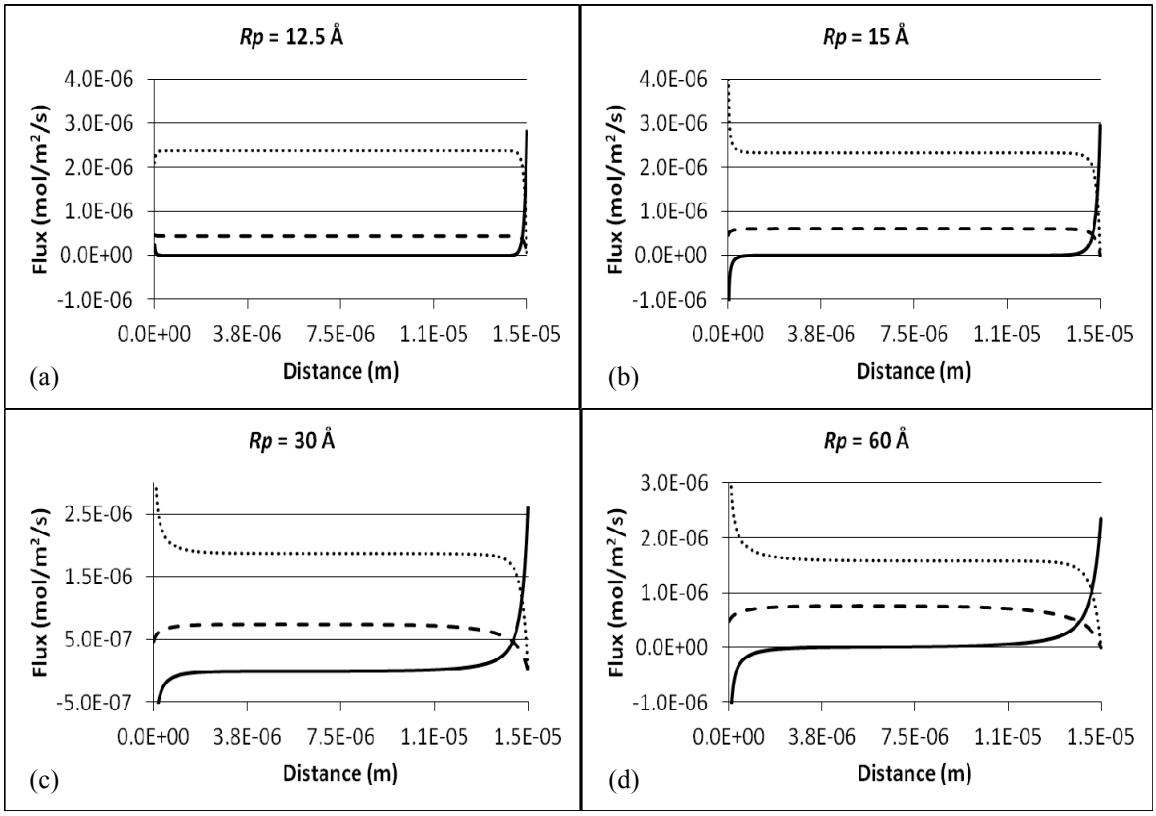

Figure 4.18. Diffusive flux (solid line), convective flux (dashed line), and electrophoretic flux (dotted line) of the TEA ion plotted as a function of position in the pore with 10 mM sodium PSS in the cathodal chamber. The plots show the results of theoretical Nernst-Planck calculations with (a) *Rp* = 12.5 Å, (b) *Rp* = 15 Å, (c) *Rp* = 30 Å, and (d) *Rp* = 60 Å.

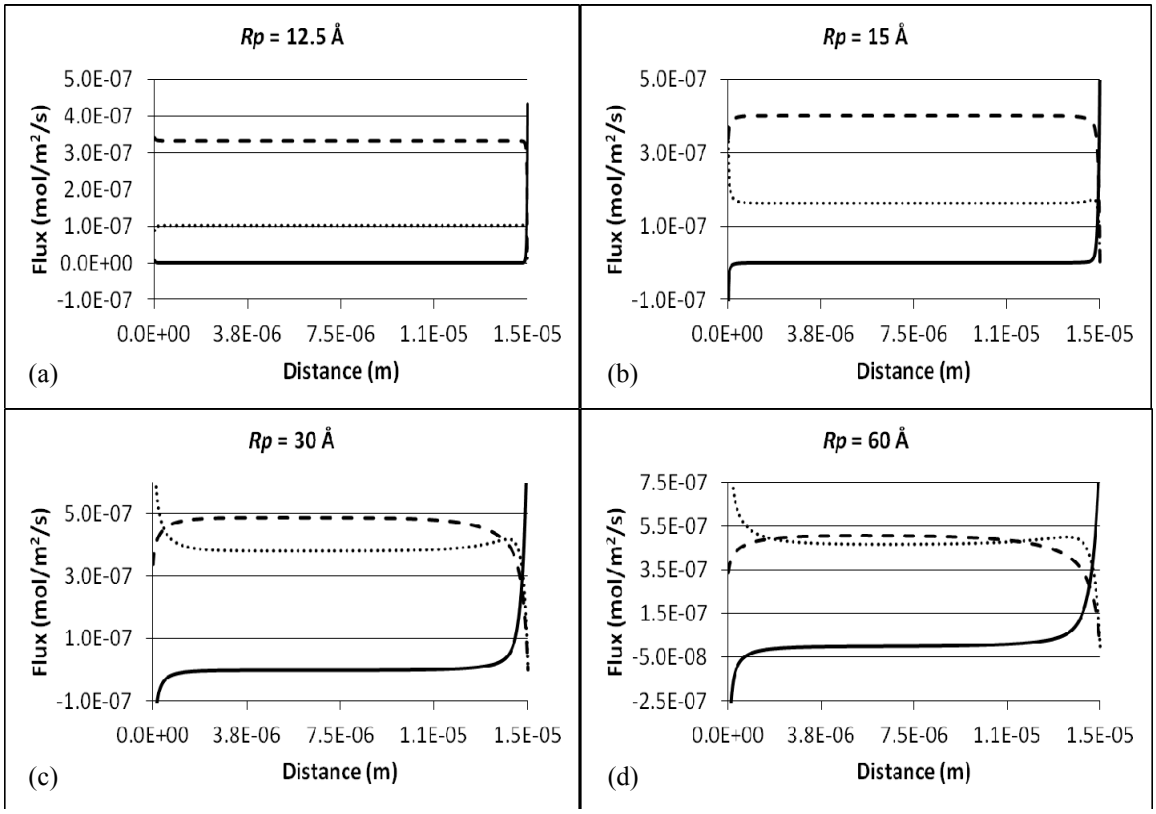

Figure 4.19. Diffusive flux (solid line), convective flux (dashed line), and electrophoretic flux (dotted line) of the TPP ion plotted as a function of position in the pore with 10 mM sodium PSS in the cathodal chamber. The plots show the results of theoretical Nernst-Planck calculations with (a) *Rp* = 12.5 Å, (b) *Rp* = 15 Å, (c) *Rp* = 30 Å, and (d) *Rp* = 60 Å.

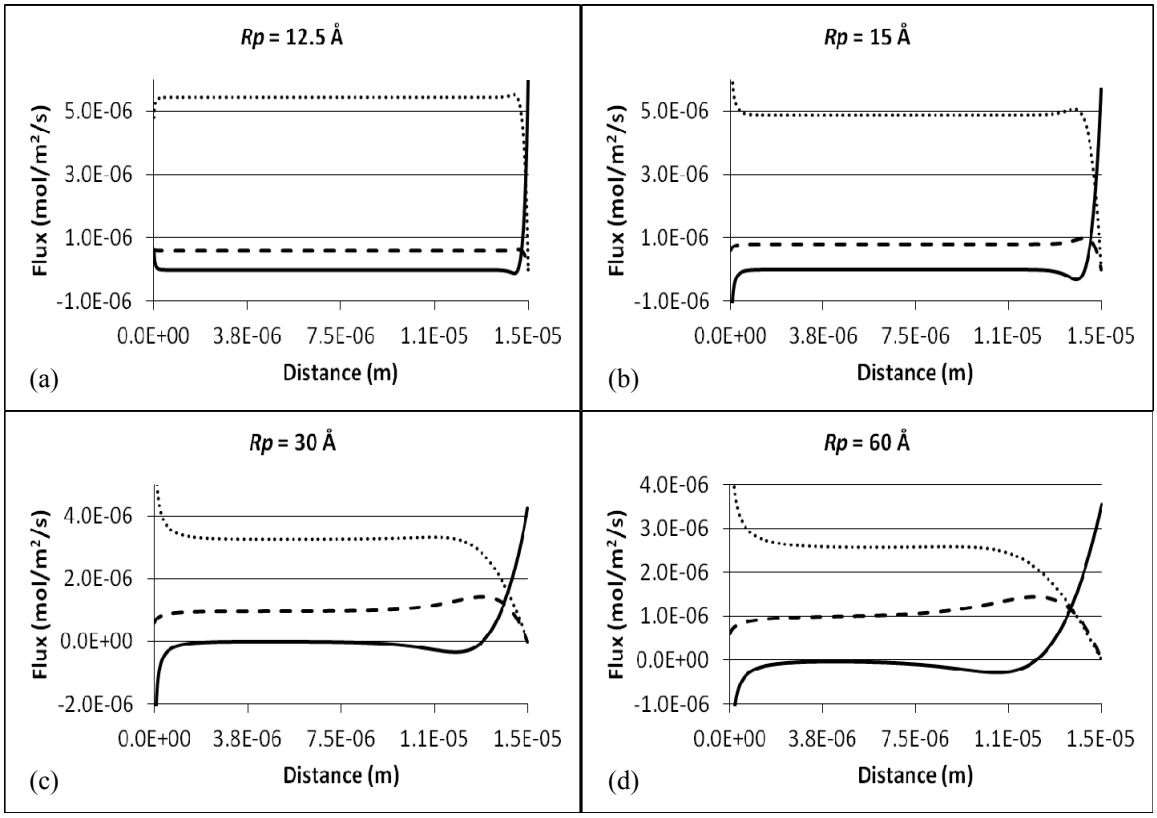

Figure 4.20. Diffusive flux (solid line), convective flux (dashed line), and electrophoretic flux (dotted line) of the ^{22}Na ion plotted as a function of position in the pore with 100 mM sodium PSS in the cathodal chamber. The plots show the results of theoretical Nernst-Planck calculations with (a) *Rp* = 12.5 Å, (b) *Rp* = 15 Å, (c) *Rp* = 30 Å, and (d) *Rp* = 60 Å.

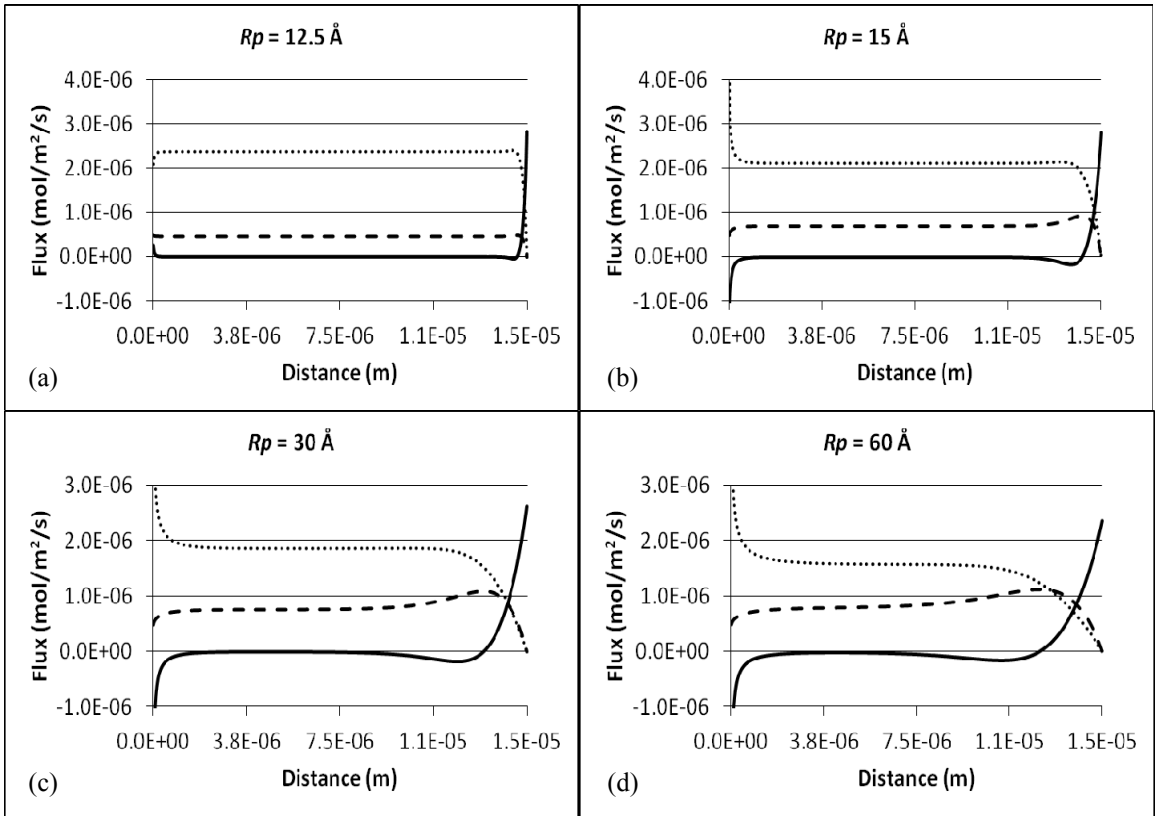

Figure 4.21. Diffusive flux (solid line), convective flux (dashed line), and electrophoretic flux (dotted line) of the TEA ion plotted as a function of position in the pore with 100 mM sodium PSS in the cathodal chamber. The plots show the results of theoretical Nernst-Planck calculations with (a) Rp = 12.5 Å, (b) Rp = 15 Å, (c) Rp = 30 Å, and (d) Rp = 60 Å.

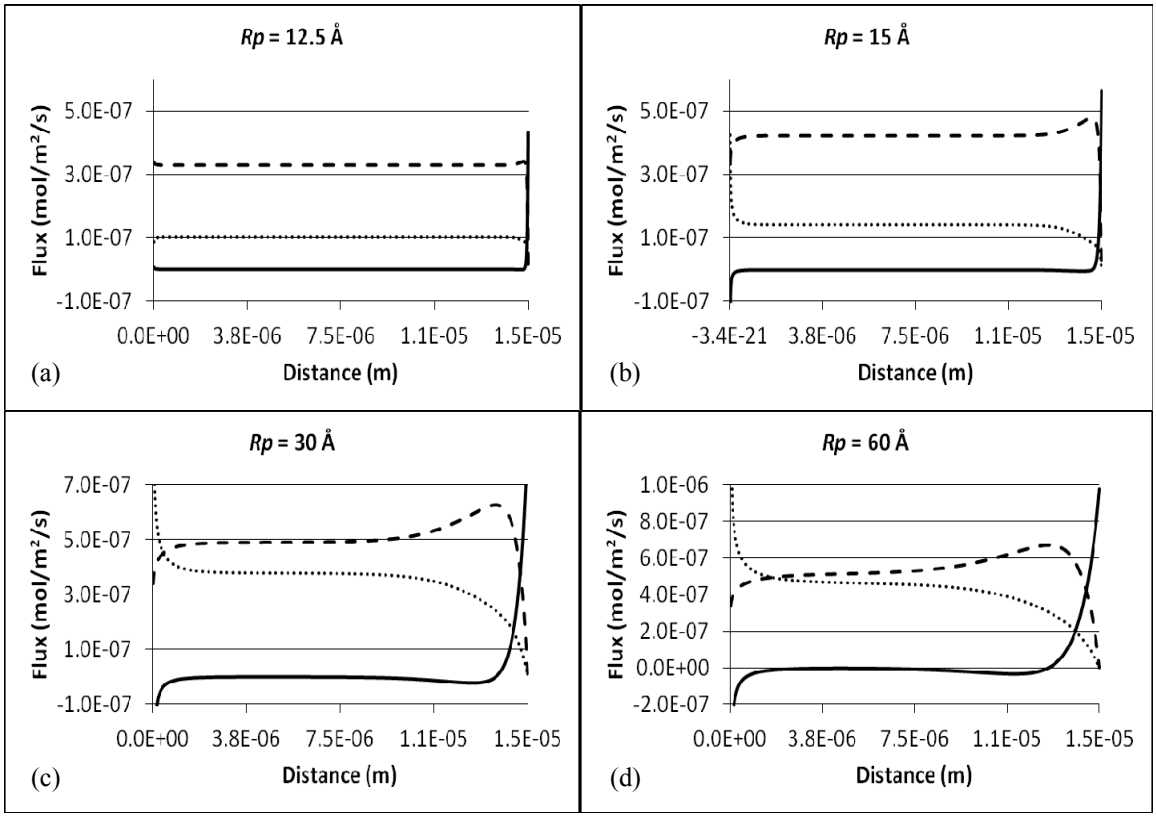

Figure 4.22. Diffusive flux (solid line), convective flux (dashed line), and electrophoretic flux (dotted line) of the TPP ion plotted as a function of position in the pore with 100 mM sodium PSS in the cathodal chamber. The plots show the results of theoretical Nernst-Planck calculations with (a) *Rp* = 12.5 Å, (b) *Rp* = 15 Å, (c) *Rp* = 30 Å, and (d) *Rp* = 60 Å.

permeant, $J_{ion,theor}$, is just equal to the sum of the electrophoretic component and the convective component. One may note from Eq. 4.2 that the convective flux component is proportional to the probe permeant concentration while the electrophoretic flux component is proportional to the product of the potential gradient and the probe permeant concentration, both which are relatively constant in the plateau regions and independent of the sodium PSS concentration in the cathodal chamber.

4.3.2.2 Comparison of $P_{ion,exp}$ and $P_{ion,theor}$ for the cationic probe permeants

Eqs. 4.1 and 4.5 were used to calculate $P_{ion,exp}$ and $P_{ion,theor}$, respectively, for each of the cationic permeants. The $P_{ion,exp}$ and $P_{ion,theor}$ values for the three sodium PSS concentrations in the cathodal chamber are summarized in Tables 4.2 – 4.4. It can be noted that $P_{ion,theor}$ calculated with Eq. 4.5 is relatively insensitive to the choice of Rp. Despite this shortcoming, it can be concluded that the "best" Rp value would be in the vicinity of Rp = 30 Å when considering the results of all three sodium PSS concentrations.

4.3.3 Anionic permeants

4.3.3.1 Theoretical Results

The concentration profiles of the anionic probe permeants from the theoretical Nernst-Planck calculations are shown in Figures 4.23 – 4.25; the corresponding diffusive, convective, and electrophoretic flux component plots are presented in Figures 4.26 – 4.34. It should be helpful at this point to remind the reader that, in the experiments (and in the theoretical calculations), the anionic probe permeants were

Table 4.2. Summary of experimental permeability coefficients ($P_{ion,exp}$) and theoretical permeability coefficients ($P_{ion,theor}$) of the cationic probe permeants with 100 mM sodium PSS in the cathodal chamber. The mean experimental voltage and the voltages from the theoretical Nernst-Planck calculations are also included.

Permeant ion	$P_{ion,exp}$ [a] (10^{-6} cm/s)	$P_{ion,theor}$ (10^{-6} cm/s)			
		Rp = 12.5 Å	*Rp = 15 Å*	*Rp = 30 Å*	*Rp = 60 Å*
^{22}Na	9.7 ± 2.4	13	12	8.9	7.5
TEA	4.6 ± 1.2	5.9	6.2	5.5	4.9
TPP	1.7 ± 0.2	0.9	1.2	1.8	2.0
Voltage (V)	0.4 ± 0.1	3.4	1.8	0.6	0.4

[a] Mean ± S.D. for n ≥ 4 experiments.

Table 4.3. Summary of experimental permeability coefficients ($P_{ion,exp}$) and theoretical permeability coefficients ($P_{ion,theor}$) of the cationic probe permeants with 10 mM sodium PSS in the cathodal chamber. The mean experimental voltage and the voltages from the theoretical Nernst-Planck calculations are also included.

Permeant ion	$P_{ion,exp}$ [a] (10^{-6} cm/s)	$P_{ion,theor}$ (10^{-6} cm/s)			
		Rp = 12.5 Å	*Rp = 15 Å*	*Rp = 30 Å*	*Rp = 60 Å*
^{22}Na	7.8 ± 1.3	13	12	8.8	7.4
TEA	5.8 ± 0.4	5.9	6.2	5.5	4.9
TPP	1.0 ± 0.1	0.9	1.2	2.0	2.1
Voltage (V)	0.5 ± 0.1	3.4	1.9	0.7	0.5

[a] Mean ± S.D. for n ≥ 4 experiments.

Table 4.4. Summary of experimental permeability coefficients ($P_{ion,exp}$) and theoretical permeability coefficients ($P_{ion,theor}$) of the cationic probe permeants with 1 mM sodium PSS in the cathodal chamber. The mean experimental voltage and the voltages from the theoretical Nernst-Planck calculations are also included.

Permeant ion	$P_{ion,exp}$ [a] (10^{-6} cm/s)	$P_{ion,theor}$ (10^{-6} cm/s)			
		Rp = 12.5 Å	*Rp = 15 Å*	*Rp = 30 Å*	*Rp = 60 Å*
^{22}Na	8.8 ± 0.6	13	12	8.8	7.5
TEA	5.4 ± 0.6	5.9	6.1	5.4	4.9
TPP	0.9 ± 0.2	0.8	1.0	1.6	1.9
Voltage (V)	0.9 ± 0.1	3.0	1.8	0.8	0.6

[a] Mean ± S.D. for n ≥ 4 experiments.

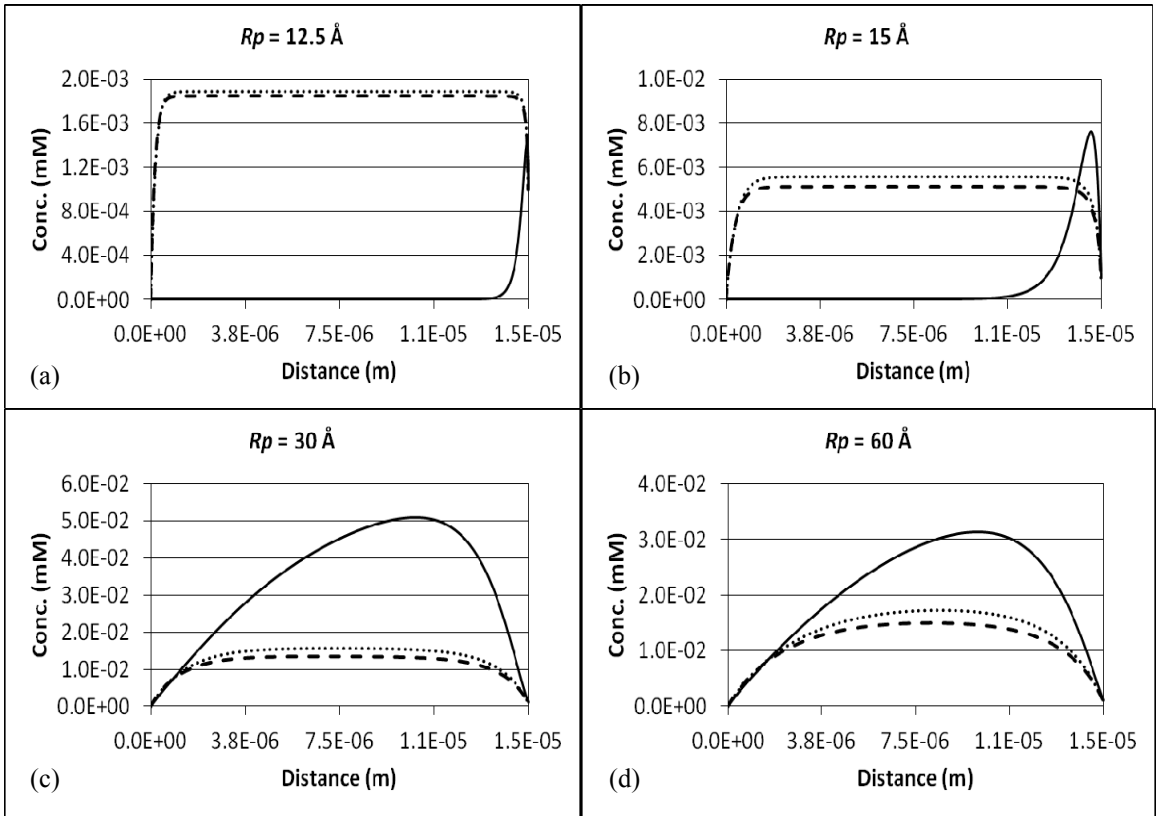

Figure 4.23. Concentration of the ^{36}Cl (dashed line), SA (dotted line), and TC (solid line) ions plotted as a function of position in the pore with 1 mM sodium PSS in the cathodal chamber. The plots show the results of theoretical Nernst-Planck calculations with (a) *Rp* = 12.5 Å, (b) *Rp* = 15 Å, (c) *Rp* = 30 Å, and (d) *Rp* = 60 Å.

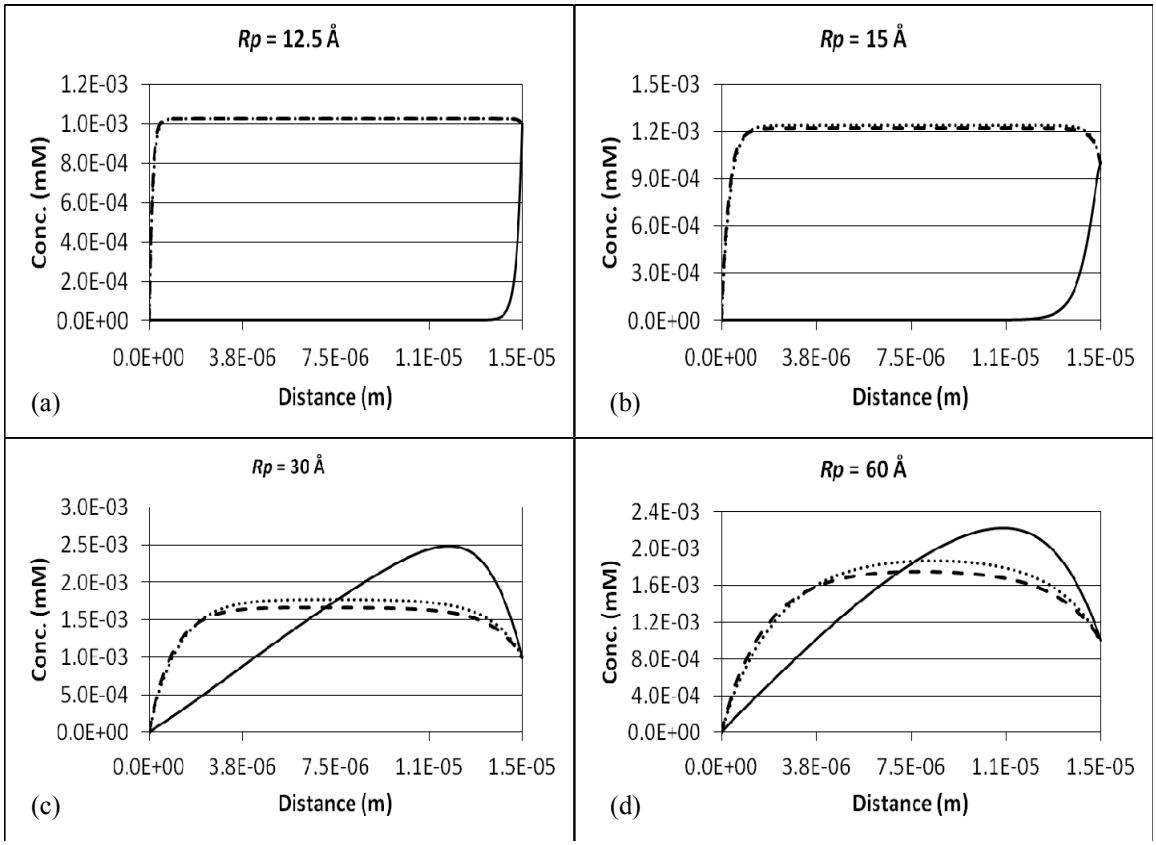

Figure 4.24. Concentration of the ^{36}Cl (dashed line), SA (dotted line), and TC (solid line) ions plotted as a function of position in the pore with 10 mM sodium PSS in the cathodal chamber. The plots show the results of theoretical Nernst-Planck calculations with (a) *Rp* = 12.5 Å, (b) *Rp* = 15 Å, (c) *Rp* = 30 Å, and (d) *Rp* = 60 Å.

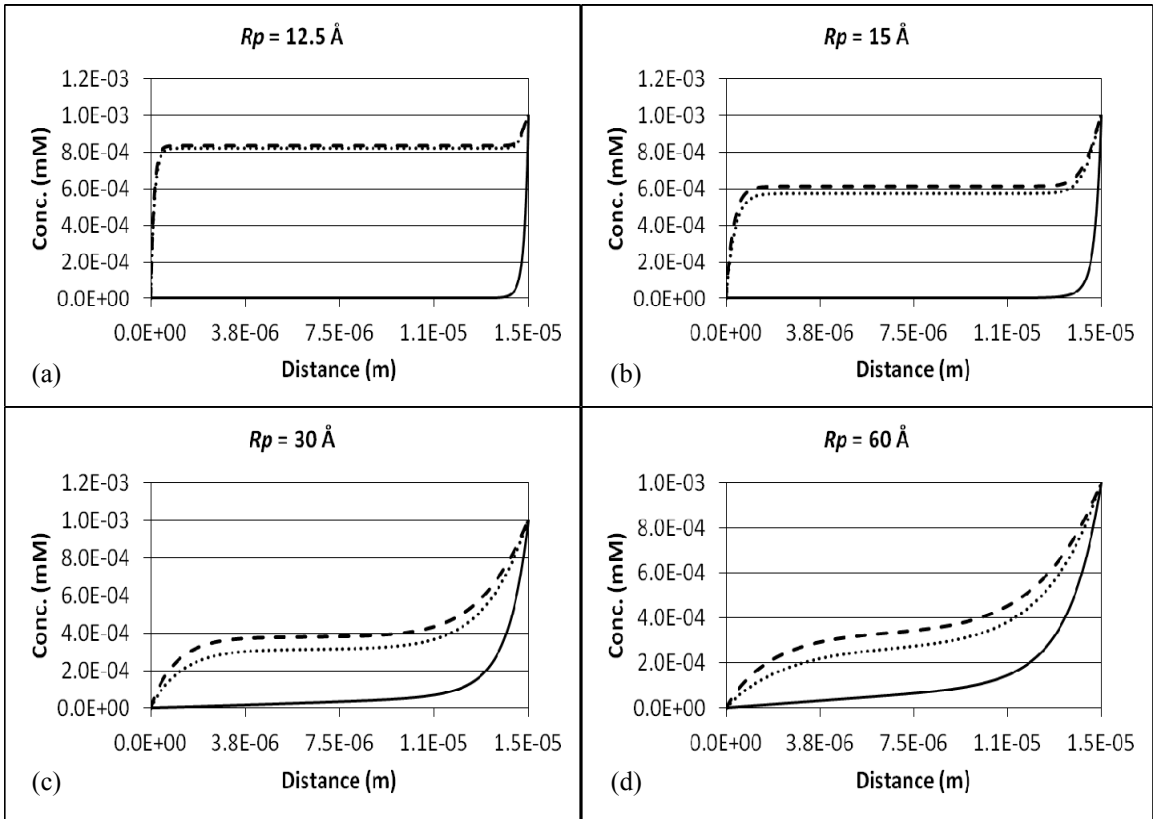

Figure 4.25. Concentration of the ^{36}Cl (dashed line), SA (dotted line), and TC (solid line) ions plotted as a function of position in the pore with 100 mM sodium PSS in the cathodal chamber. The plots show the results of theoretical Nernst-Planck calculations with (a) *Rp* = 12.5 Å, (b) *Rp* = 15 Å, (c) *Rp* = 30 Å, and (d) *Rp* = 60 Å.

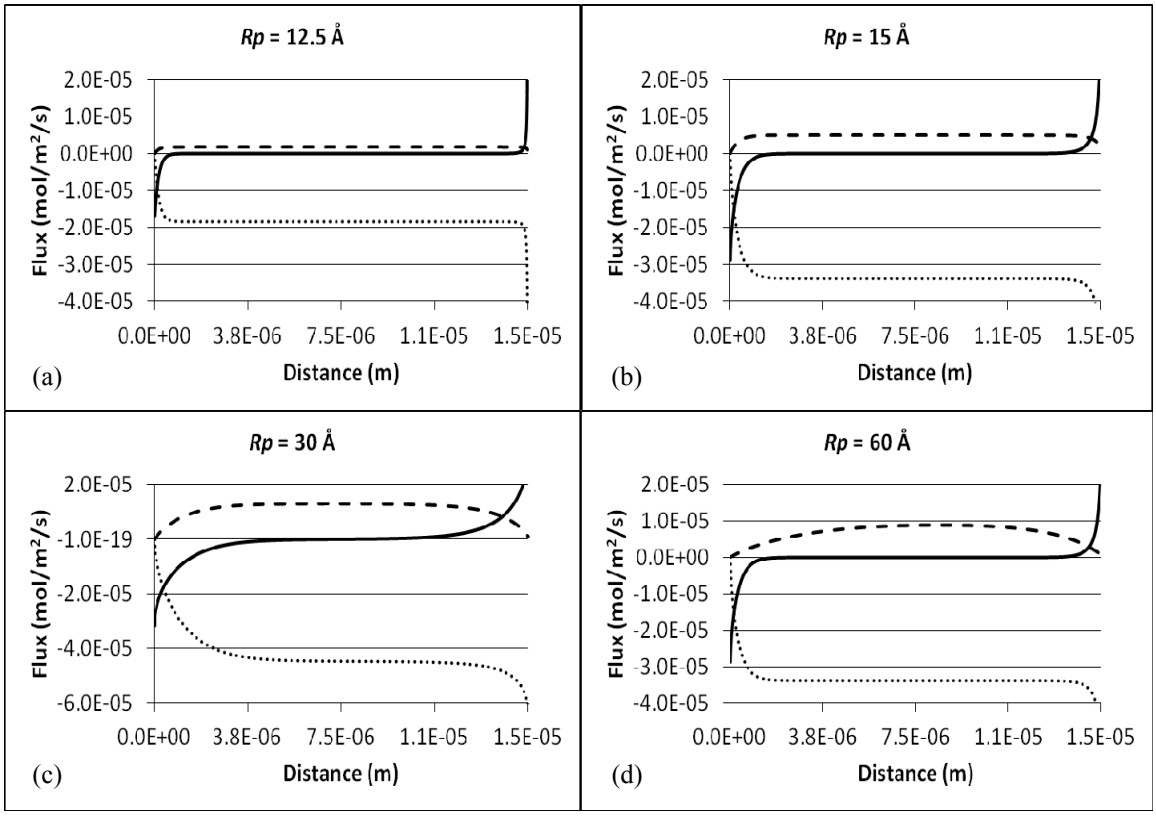

Figure 4.26. Diffusive flux (solid line), convective flux (dashed line), and electrophoretic flux (dotted line) of the ^{36}Cl ion plotted as a function of position in the pore with 1 mM sodium PSS in the cathodal chamber. The plots show the results of theoretical Nernst-Planck calculations with (a) *Rp* = 12.5 Å, (b) *Rp* = 15 Å, (c) *Rp* = 30 Å, and (d) *Rp* = 60 Å.

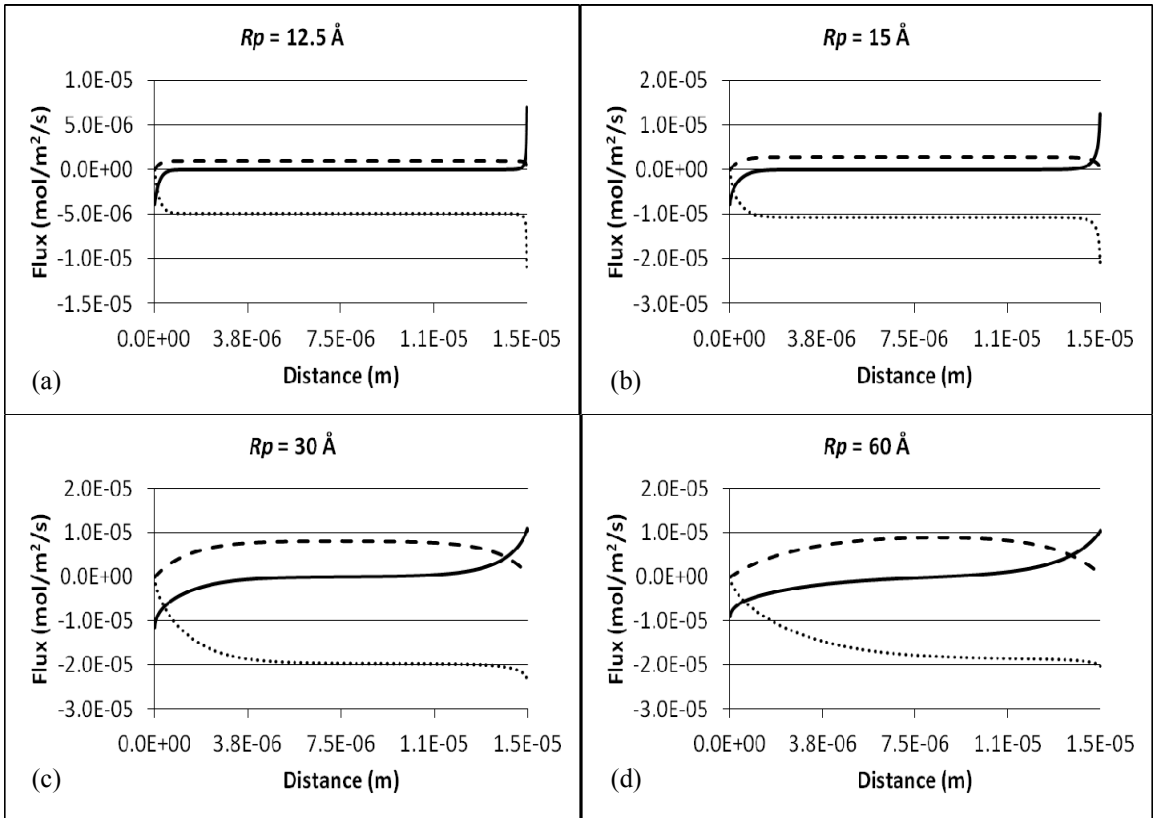

Figure 4.27. Diffusive flux (solid line), convective flux (dashed line), and electrophoretic flux (dotted line) of the SA ion plotted as a function of position in the pore with 1 mM sodium PSS in the cathodal chamber. The plots show the results of theoretical Nernst-Planck calculations with (a) *Rp* = 12.5 Å, (b) *Rp* = 15 Å, (c) *Rp* = 30 Å, and (d) *Rp* = 60 Å.

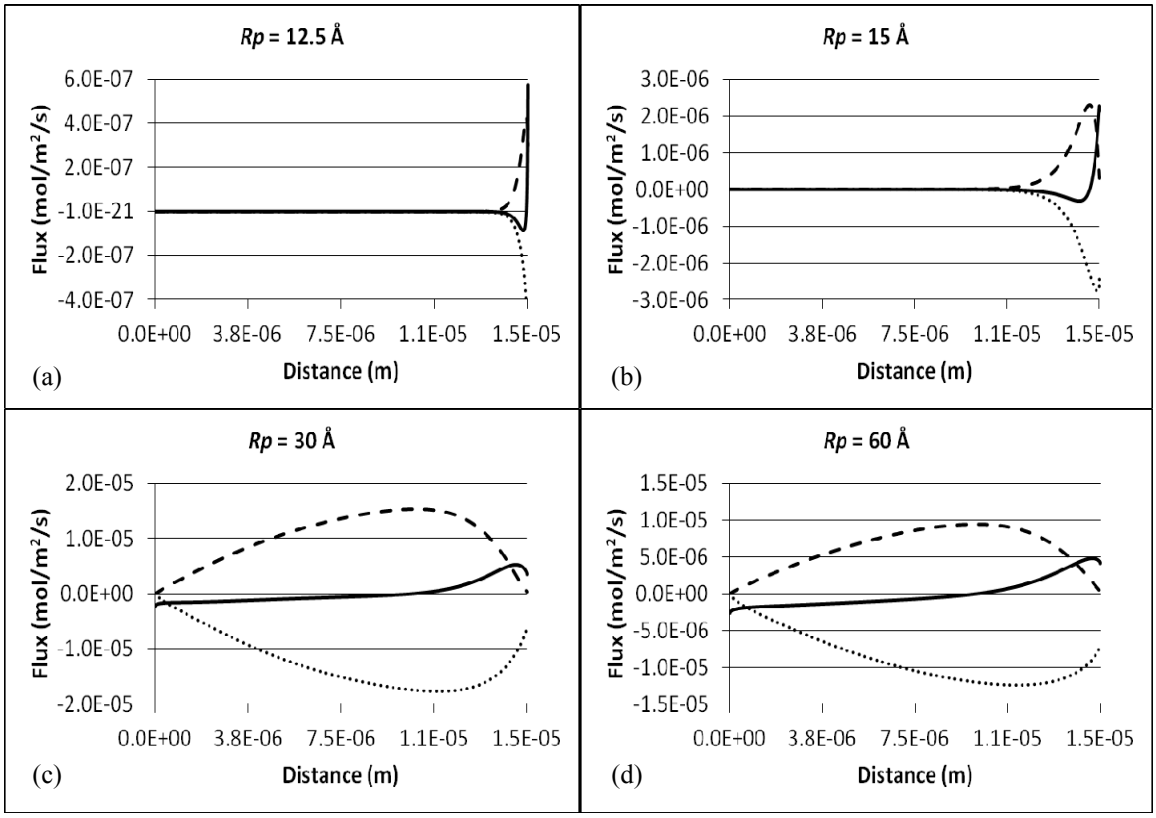

Figure 4.28. Diffusive flux (solid line), convective flux (dashed line), and electrophoretic flux (dotted line) of the TC ion plotted as a function of position in the pore with 1 mM sodium PSS in the cathodal chamber. The plots show the results of theoretical Nernst-Planck calculations with (a) *Rp* = 12.5 Å, (b) *Rp* = 15 Å, (c) *Rp* = 30 Å, and (d) *Rp* = 60 Å.

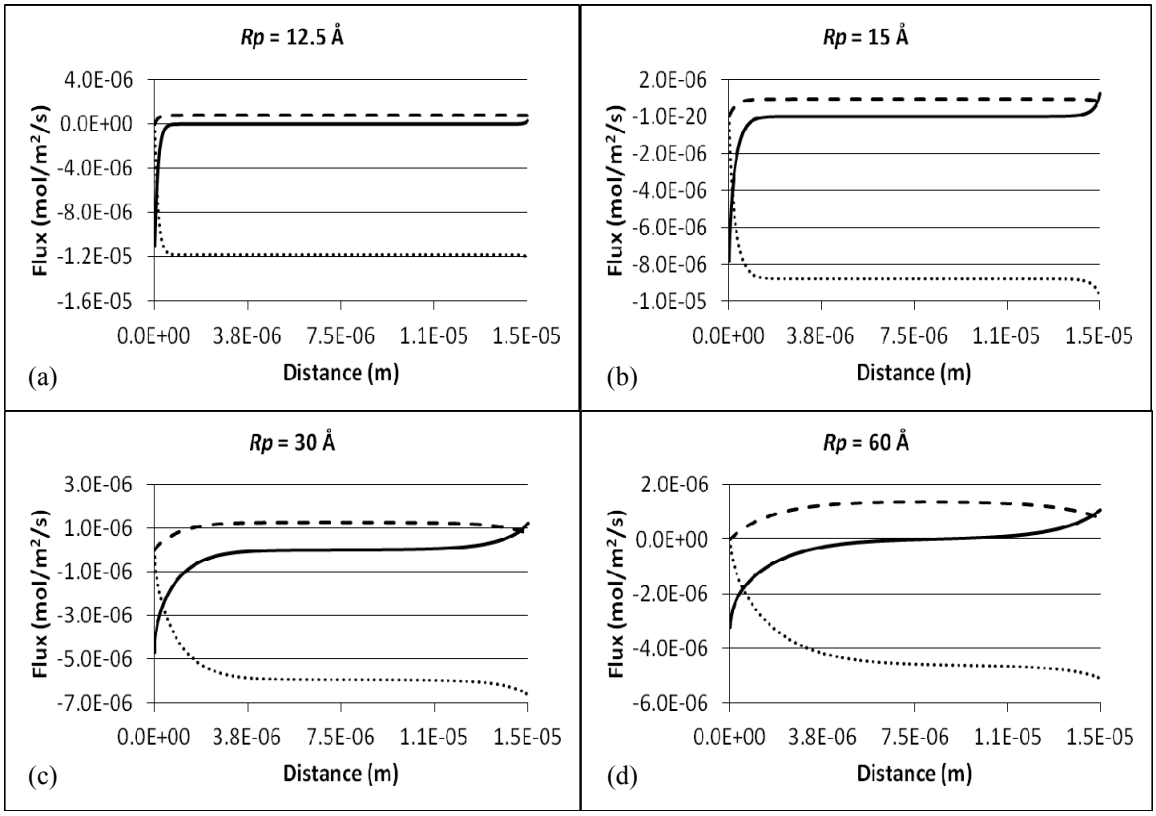

Figure 4.29. Diffusive flux (solid line), convective flux (dashed line), and electrophoretic flux (dotted line) of the ^{36}Cl ion plotted as a function of position in the pore with 10 mM sodium PSS in the cathodal chamber. The plots show the results of theoretical Nernst-Planck calculations with (a) *Rp* = 12.5 Å, (b) *Rp* = 15 Å, (c) *Rp* = 30 Å, and (d) *Rp* = 60 Å.

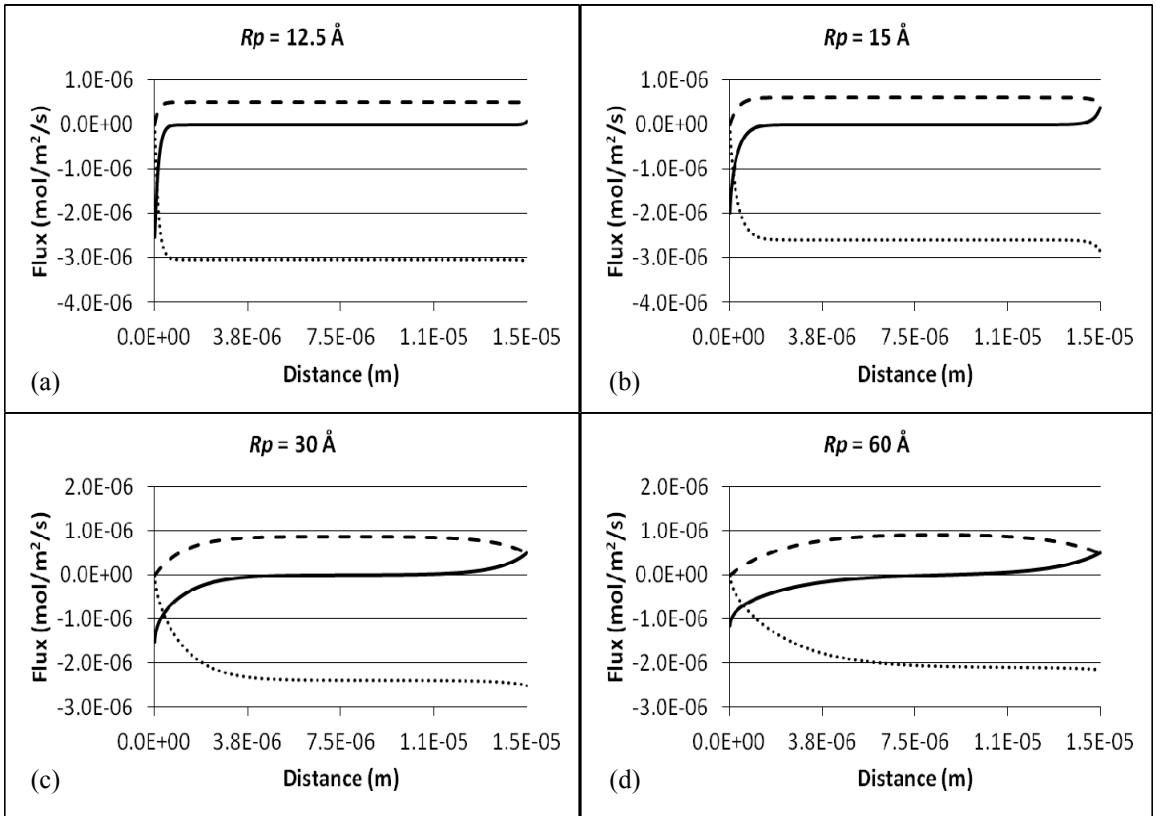

Figure 4.30. Diffusive flux (solid line), convective flux (dashed line), and electrophoretic flux (dotted line) of the SA ion plotted as a function of position in the pore with 10 mM sodium PSS in the cathodal chamber. The plots show the results of theoretical Nernst-Planck calculations with (a) *Rp* = 12.5 Å, (b) *Rp* = 15 Å, (c) *Rp* = 30 Å, and (d) *Rp* = 60 Å.

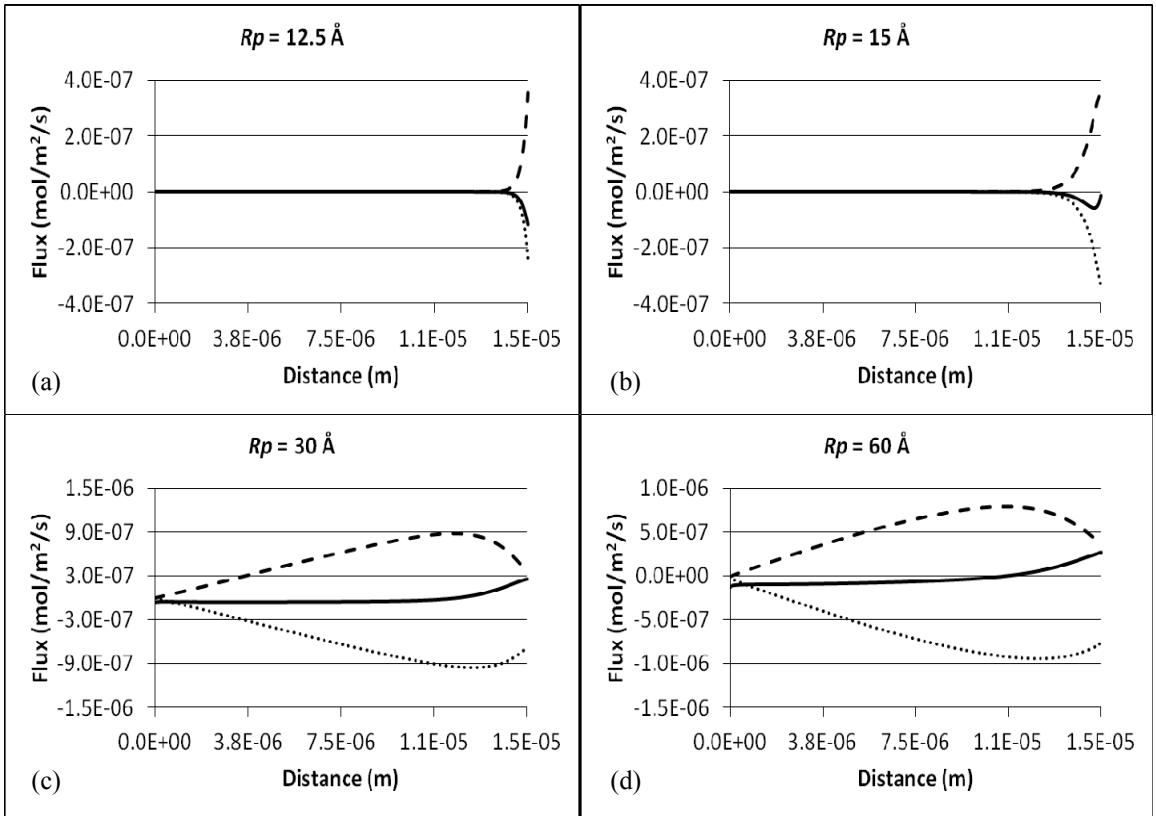

Figure 4.31. Diffusive flux (solid line), convective flux (dashed line), and electrophoretic flux (dotted line) of the TC ion plotted as a function of position in the pore with 10 mM sodium PSS in the cathodal chamber. The plots show the results of theoretical Nernst-Planck calculations with (a) *Rp* = 12.5 Å, (b) *Rp* = 15 Å, (c) *Rp* = 30 Å, and (d) *Rp* = 60 Å.

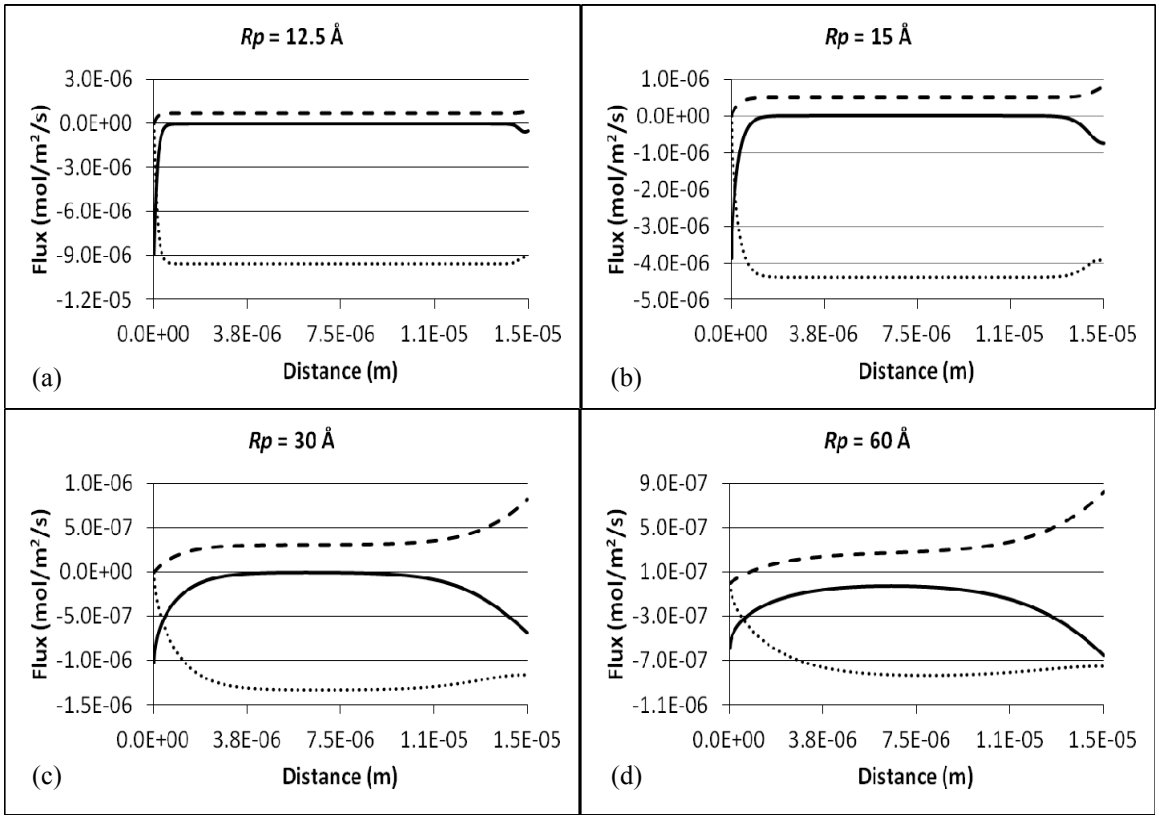

Figure 4.32. Diffusive flux (solid line), convective flux (dashed line), and electrophoretic flux (dotted line) of the ^{36}Cl ion plotted as a function of position in the pore with 100 mM sodium PSS in the cathodal chamber. The plots show the results of theoretical Nernst-Planck calculations with (a) *Rp* = 12.5 Å, (b) *Rp* = 15 Å, (c) *Rp* = 30 Å, and (d) *Rp* = 60 Å.

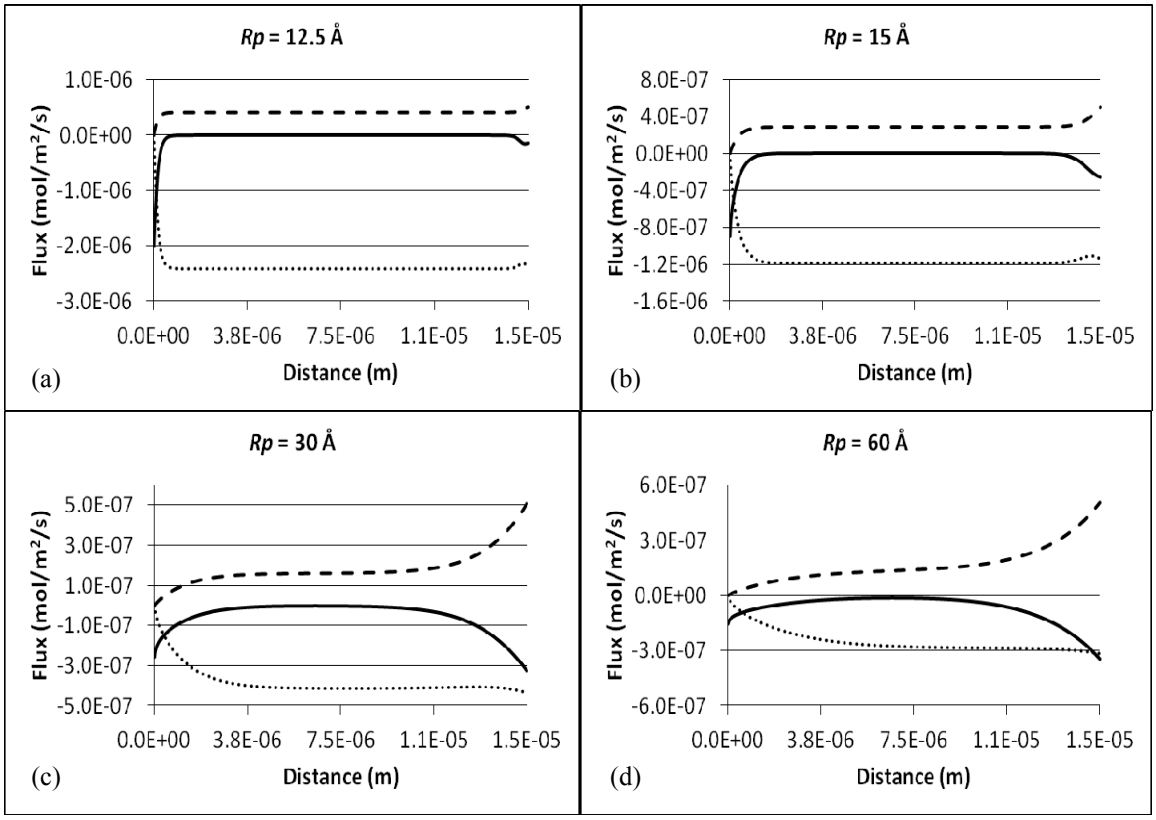

Figure 4.33. Diffusive flux (solid line), convective flux (dashed line), and electrophoretic flux (dotted line) of the SA ion plotted as a function of position in the pore with 100 mM sodium PSS in the cathodal chamber. The plots show the results of theoretical Nernst-Planck calculations with (a) *Rp* = 12.5 Å, (b) *Rp* = 15 Å, (c) *Rp* = 30 Å, and (d) *Rp* = 60 Å.

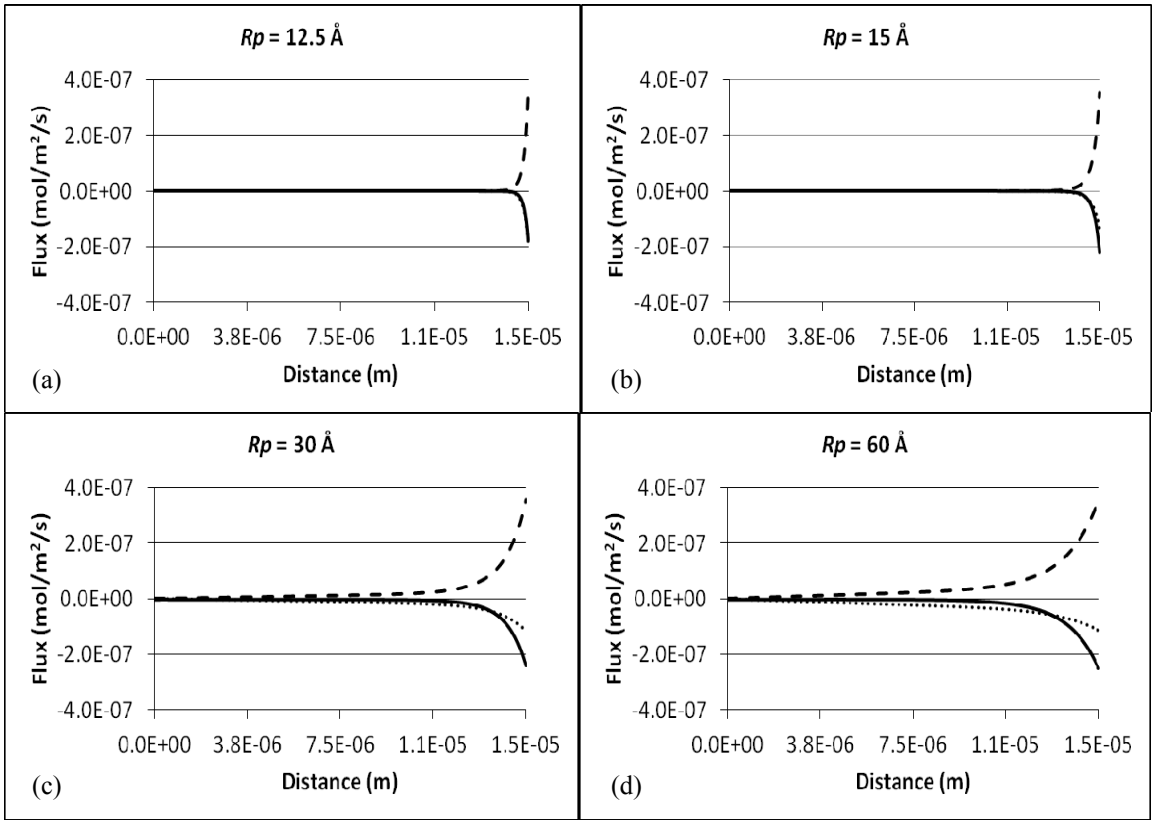

Figure 4.34. Diffusive flux (solid line), convective flux (dashed line), and electrophoretic flux (dotted line) of the TC ion plotted as a function of position in the pore with 100 mM sodium PSS in the cathodal chamber. The plots show the results of theoretical Nernst-Planck calculations with (a) *Rp* = 12.5 Å, (b) *Rp* = 15 Å, (c) *Rp* = 30 Å, and (d) *Rp* = 60 Å.

present (at 10^{-3} mM) in the cathodal chamber together with the sodium PSS, while the cationic probe permeants (also at 10^{-3} mM) were in the anodal chamber in PBS. This difference causes the electrophoretic flux and the convective flux of the probe permeants to be in opposite directions in the case of the anionic probe permeants while being in the same direction in the case of the cationic probe permeants. This difference causes other general pattern differences between the anionic probe permeant behavior and the cationic probe permeant behavior as seen when comparing the plots of Figures 4.11 – 4.22 with those of Figures 4.23 – 4.34: (a) the anionic probe permeant concentrations in the plateau regions (where the potential gradients are relatively independent of the sodium PSS concentration in the cathodal chamber; see Figure 4.1) are strongly dependent on the sodium PSS concentration in the cathodal chamber while, in the case of cationic probe permeants, the probe permeant concentrations in the plateau regions are seen to be relatively independent of the sodium PSS concentration; and (b) the flux components of the anionic probe permeants are seen to vary greatly with the sodium PSS concentration in the cathodal chamber (most easily seen in the plateau regions) while this is not the case for the cationic probe permeants; this anionic probe permeant flux variation with the sodium PSS concentration parallels, semiquantitatively, the concentration variation of the anionic probe permeants mentioned above.

4.3.3.2 Comparison of $P_{ion,exp}$ and $P_{ion,theor}$ for the anionic probe permeants

$P_{ion,exp}$ and $P_{ion,theor}$ values for anionic permeants are summarized in Tables 4.5 – 4.7. The experimental permeability coefficient of the PSS ion was only obtained in experiments with 100 mM sodium PSS in the cathodal chamber (see Chapter 3 for details

Table 4.5. Summary of experimental permeability coefficients ($P_{ion,exp}$) and theoretical permeability coefficients ($P_{ion,theor}$) of the anionic probe permeants and PSS ion with 100 mM sodium PSS in the cathodal chamber. The mean experimental voltage and the voltages from the theoretical Nernst-Planck calculations are also included.

Permeant	$P_{ion,exp}$ [a] (10^{-6} cm/s)	$P_{ion,theor}$ (10^{-6} cm/s)			
		Rp = 12.5 Å	*Rp = 15 Å*	*Rp = 30 Å*	*Rp = 60 Å*
Cl	2.0 ± 0.2	19	8.1	2.1	1.2
SA	0.8 ± 0.3	4.2	1.9	0.5	0.3
TC	0.07 ± 0.02	0	0	0.02	0.01
PSS	0.18 ± 0.05[b]	0.01	0.09	0.49	0.67
Voltage (V)	0.4 ± 0.1	3.4	1.8	0.6	0.4

[a] Mean ± S.D. for n ≥ 4 experiments.
[b] $P_{ion,exp}$ for PSS determined in previous experiments (see Chapter 3 for details of PSS iontophoresis experiments).

Table 4.6. Summary of experimental permeability coefficients ($P_{ion,exp}$) and theoretical permeability coefficients ($P_{ion,theor}$) of the anionic probe permeants and PSS ion with 10 mM sodium PSS in the cathodal chamber. The mean experimental voltage and the voltages from the theoretical Nernst-Planck calculations are also included.

Permeant	$P_{ion,exp}$ [a] (10^{-6} cm/s)	$P_{ion,theor}$ (10^{-6} cm/s)			
		Rp = 12.5 Å	*Rp = 15 Å*	*Rp = 30 Å*	*Rp = 60 Å*
Cl	3.4 ± 0.5	23	16	9.7	6.8
SA	1.2 ± 0.1	5.3	4.1	3.2	2.4
TC	0.15 ± 0.02	0	0	0.12	0.27
PSS	--	0.1	1.0	4.9	6.8
Voltage (V)	0.5 ± 0.1	3.4	1.9	0.7	0.5

[a] Mean ± S.D. for n ≥ 4 experiments.

Table 4.7. Summary of experimental permeability coefficients ($P_{ion,exp}$) and theoretical permeability coefficients ($P_{ion,theor}$) of the anionic probe permeants and PSS ion with 1 mM sodium PSS in the cathodal chamber. The mean experimental voltage and the voltages from the theoretical Nernst-Planck calculations are also included.

Permeant	$P_{ion,exp}$ [a] (10^{-6} cm/s)	$P_{ion,theor}$ (10^{-6} cm/s)			
		Rp = 12.5 Å	*Rp = 15 Å*	*Rp = 30 Å*	*Rp = 60 Å*
Cl	5.9 ± 1.2	35	60	66	47
SA	3.3 ± 1.2	8.1	16	24	19
TC	0.19 ± 0.09	0	0	4.8	5.4
PSS	--	1.7	11	49	67
Voltage (V)	0.9 ± 0.1	3.0	1.8	0.8	0.6

[a] Mean ± S.D. for n ≥ 4 experiments.

of PSS iontophoresis experiments). With the exception of the TC ion, the agreement between $P_{ion,exp}$ and $P_{ion,theor}$ was good with 100 mM sodium PSS in the cathodal chamber *Rp* values between 15 Å and 30 Å; this includes the results with the PSS ion. However the agreement between $P_{ion,exp}$ and $P_{ion,theor}$ was relatively poor for the other two sodium PSS concentrations.

4.4 Discussion

4.4.1 Assumptions in the theoretical calculations

Given the complexity of the current iontophoresis system, some assumptions were required before using the modified Nernst-Planck model in the calculation of theoretical potential gradients, concentration profiles, and flux values. One of the key assumptions was in the treatment of the PSS oligomers that were used as the conducting ions in the cathodal chamber. Our approach was to use the diffusion coefficient, hydrodynamic radius and effective charge of the PSS heptamer species to represent those of the entire population of the PSS oligomers. Previous experimental characterization of sodium PSS solutions was carried out using CE and it was found that the PSS heptamer and hexamer accounted for as much as 80% of the total area under the curve for separations using a CE system with 0.1 M PBS as the background electrolyte (see Chapter 3). To be certain that using a single species of the PSS oligomers did not influence the major conclusions from the results of theoretical Nernst-Planck calculations, additional calculations were performed with the cathodal chamber solution being composed of a mixture of 70% PSS heptamer and 30% PSS tetramer; the results of these calculations did not result in significantly different theoretical voltages and $P_{ion,theor}$ values (data not shown).

Also for practical reasons, the present Nernst-Planck model has ignored considering the importance of pore size distribution within HMS in the treatment of the experimental data. From our baseline study the pore size distribution issue seemed to be relatively unimportant in the analysis of ionic probe permeant data (Chapter 2); however, pore size distribution was apparent in examining the experimental results with the nonionic probe permeants (Chapters 2 and 3).

Pikal et. al have concluded that the available aqueous pore pathways in HMS stratum corneum that are utilized in the transport of ionic and nonionic permeants are likely composed of pores having net positive, negative, or neutral surface charge.[13-15] Earlier baseline studies provide further evidence of such heterogeneity of pore pathways in the HMS (Chapter 2). In the present study and in the baseline study, the viewpoint has been taken that the iontophoretic (convective) transport of nonionic permeants in HMS would be expected to be confined to the charged pores with negatively charged pores overwhelmingly dominating; and the iontophoretic transport of ionic permeants would involve all pores. In both the present study and in the baseline study (Chapter 2), however, in order to have a tractable physical model to be used in the interpretation of the iontophoretic flux data, the assumption has been made that a single pore type may represent the HMS stratum corneum. The consequence of this assumption on the present modeling approach was that the electroosmotic velocity, represented by values of Wv (calculated from the results of earlier iontophoresis experiments with nonionic permeants) would be effectively spread out or averaged across all pores utilized by the ionic permeants. In the baseline study, the convective (i.e., electroosmotic) fluxes were

rather small in most cases compared to the present situation where electroosmosis is seen to be much more important, by four to six fold (see Chapter 3).

4.4.2 Good agreement between theoretical predictions and experimental results with the cationic probe permeants

As discussed previously, one of the major objectives of theoretical Nernst-Planck calculations was to find appropriate values of *Rp* where the theoretical predictions and experimental results were in good agreement. Examination of Tables 4.2 – 4.4 reveals that calculations with pore sizes in the vicinity of 30 Å resulted in theoretical predictions for the voltage and $P_{ion,theor}$ values for the cations that were in good agreement with experimental values. In particular, the agreement between $P_{ion,theor}$ and $P_{ion,exp}$ across all three concentrations of the sodium PSS in the cathodal chamber, was remarkable with the ^{22}Na and TEA ions as the probe permeants (Tables 4.2 – 4.4); with the TPP ion the agreement between $P_{ion,theor}$ and $P_{ion,exp}$ was good for calculations with 100 mM sodium PSS in the cathodal chamber but less so with 10 mM and 1 mM sodium PSS in the cathodal chamber. It can also be noted that the experimental and the theoretical voltages are in good agreement with *Rp* = 30 Å. Overall the agreement between the model predictions at *Rp* = 30 Å and experiments with the cationic probe permeants is very satisfactory.

It is instructive at this point to compare these results with those of the baseline study (Chapter 2) where the medium present in the both the cathodal and anodal chambers was PBS. The *Rp* value deduced in the baseline study was 25 ± 6 Å based on

experiments using the same cationic probe permeants but employing a simpler treatment of the experimental data (i.e, by not directly incorporating the convective contribution to the flux into the Nernst-Planck differential equation as has been done in the present study). In light of the much greater electroosmosis component encountered in the present study, requiring a different calculational procedure, the good agreement between the two studies is quite encouraging.

It is interesting to note that both $P_{ion,exp}$ and $P_{ion,theor}$ for cations are relatively constant and independent of the concentration of sodium PSS in the cathodal chamber. This finding is consistent with the behavior of the potential gradient (Figure 4.1) and the probe permeant concentration profiles (Figures 4.11 – 4.13). As the electrophoretic flux is proportional to the product of the potential gradient and the permeant concentration, as the electroosmotic flux is proportional to the permeant concentration, and as the total flux ($J_{ion,theor}$) is the sum of the electroosmotic flux and the electrophoretic flux in the plateau regions where the diffusive flux is zero, it then follows the $J_{ion,theor}$ should be relatively independent of the sodium PSS concentration in the cathodal chamber because both the potential gradient and the probe permeant concentrations are relatively independent of the sodium PSS concentration in the plateau regions of these plots.

4.4.3 Transference number of electric current determining ions

Table 4.8 shows the theoretical and the experimental transference numbers calculated using Eqs 4.6 and 4.7 for the current determining ions, sodium and PSS. As can be seen these results indicate an *Rp* value in the range of 20 – 30 Å would be

Table 4.8. The theoretical transference number ($t_{ion,theor}$) and experimental transference number ($t_{ion,exp}$) of sodium and PSS.

PSS Conc.	Ion	$t_{ion,exp}$[a]	$t_{ion,theor}$					
			Rp = 12.5 Å	*Rp = 15 Å*	*Rp = 20 Å*	*Rp = 25 Å*	*Rp = 30 Å*	*Rp = 60 Å*
100 mM	Na	0.89 ± 0.22	0.99	0.94	0.91	0.75	0.70	0.59
	PSS	0.08 ± 0.02	0.01	0.06	0.09	0.25	0.30	0.41
10 mM	Na	0.71 ± 0.12	0.99	0.94	0.90	0.75	0.70	0.58
	PSS	--	0.01	0.06	0.10	0.25	0.30	0.42
1 mM	Na	0.81 ± 0.06	0.99	0.93	0.89	0.83	0.70	0.59
	PSS	--	0.01	0.07	0.11	0.17	0.30	0.41

[a] Mean ± S.D. for n ≥ 4 experiments.

consistent with the data, this also supporting our findings with most of the cationic probe permeant data and the 100 mM sodium PSS data with the anionic probe permeants.

4.4.4 Relatively poor agreement between theoretical predictions and experimental results with the anionic probe permeants

The $P_{ion,exp}$ values for the ^{36}Cl ion and the SA ion at 10 mM sodium PSS and at 1 mM sodium PSS are roughly 1.6 and 3.0 times greater, respectively, than at 100 mM sodium PSS; the corresponding $P_{ion,theor}$ values (for Rp = 30 Å), on the other hand , are roughly 5.5 and 40 times greater than at 100 mM sodium PSS. The reason(s) for these discrepancies between $P_{ion,exp}$ and $P_{ion,theor}$ are not apparent. The increased $P_{ion,theor}$ values (at Rp = 30 Å) for the ^{36}Cl and the SA ion at 10 mM and 1 mM sodium PSS do correlate well with higher calculated permeant concentrations (Figures 4.23 – 4.25) in the plateau region; therefore, the theoretical results are internally self-consistent. The reader is reminded that the theoretical results with the cationic probe permeants are also internally self-consistent regarding the relationship between $P_{ion,theor}$ and the model calculated permeant concentrations in the plateau regions. However, in the case the cationic probe permeants, the permeant concentrations in the plateau regions were essentially independent of the sodium PSS concentration in the cathodal chamber, while for the anionic probe permeants they are not. It therefore may be concluded that the discrepancies between $P_{ion,theor}$ and $P_{ion,exp}$ at the lower sodium PSS concentrations, in the case of the anionic permeants, may reside in a defect in the model associated with the significant dependence of the probe permeant concentration (in the plateau region) upon

the sodium PSS concentration. When it is noted that the varying anionic probe permeant concentration correlates with the varying potential gradient patterns in the vicinity of the membrane/cathodal chamber interface, one might conclude that the defect in the model is related to an inability of the anionic probe permeants to respond to the high potential gradients in the vicinity of the membrane/cathodal chamber interface; alternatively, the defect in the model may reside in the inability of the HMS system to generate the high potential gradients at the low sodium PSS concentrations in the first place. Without more work, both experimental and theoretical, it would appear to be difficult in attempting to pinpoint the defect in the current theoretical model.

4.4.5 Influence of enhanced electroosmosis on the experimental and theoretical permeability coefficients of small ions

The results of earlier studies with nonionic probe permeants (Chapter 3) showed that there was as much as a sixfold enhancement of electroosmosis due to the presence of sodium PSS in the cathodal chamber. As one would expect, having the electroosmosis enhanced to such an extent had a significant influence on the flux of small ionic probe permeants as well. For instance, $P_{ion,exp}$ (in units of 10^{-6} cm/s) for the ^{22}Na ion was 9.7 ± 2.4, 7.8 ± 1.3, 8.8 ± 0.6, and 4.6 ± 0.4 for experiments with 100 mM sodium PSS, 10 mM sodium PSS, 1 mM sodium PSS, and 0.1 M PBS in the cathodal chamber, respectively. The approximately twofold enhancement observed in the permeability coefficient of the ^{22}Na ion was also observed for the TEA and TPP ions. As already discussed, since electroosmosis and electrophoresis of the anionic probe permeants are in opposite

directions, a decrease in the permeability coefficients of anionic probe permeants was observed when sodium PSS was in the cathodal chamber. As an example, $P_{ion,exp}$ (in units of 10^{-6} cm/s) for the ^{36}Cl ion was 2.0 ± 0.2, 3.4 ± 0.5, 5.9 ± 1.2, and 5.0 ± 0.3 for experiments with 100 mM sodium PSS, 10 mM sodium PSS, 1 mM sodium PSS, and 0.1 M PBS in the cathodal chamber, respectively. Notice that in the case of anionic probe permeant the changes observed in $P_{ion,exp}$ varied with decreasing sodium PSS concentrations in the cathodal chamber while for cationic probe permeants the enhancement of $P_{ion,exp}$ relative to baseline results remained relatively constant over the range of PSS concentrations investigated. From a practical standpoint the inclusion of PSS oligomer into an iontophoretic device designed to extract cationic and nonionic molecules across the skin could lead to better efficiency of the iontophoretic extraction.

4.5 Conclusions

In the present study we have used a novel strategy to model the transport of small ionic permeants in an iontophoresis system where significant electroosmosis has been observed. By using the transport data from earlier experiments with nonionic permeants to obtain the convective term (Wv) for small ionic probe permeants, theoretical Nernst-Planck calculations were performed to better understand the transport behavior of small ionic probe permeants in iontophoresis experiments with varying concentrations of sodium PSS in the cathodal chamber. The theoretical calculations have confirmed, somewhat surprisingly, that the independence of $P_{ion,exp}$ values for cationic permeants in response to changes in the concentration of sodium PSS in the cathodal chamber are consistent with both the calculated potential gradient and ion concentrations in the pore.

The agreement between $P_{ion,exp}$ and $P_{ion,theor}$ for the cationic probe permeants was good across all of the sodium PSS concentration investigated. Although the agreement between $P_{ion,exp}$ and $P_{ion,theor}$ for anionic probe permeants was not good, except for with 100 mM sodium PSS in the cathodal chamber, the trend of decreasing $P_{ion,theor}$ with increasing concentrations of sodium PSS in the cathodal chamber was consistent with experimental results. As already discussed, more work will be needed to develop a theoretical model that would accurately predict the behavior of small anionic probe permeants when sodium PSS is in the cathodal chamber.

4.6 References

1. Delgado-Charro MB, Guy RH 2003. Transdermal reverse iontophoresis of valproate: a noninvasive method for therapeutic drug monitoring. Pharm Res 20(9):1508-1513.

2. Higuchi WI, Li SK, Ghanem AH, Zhu H, Song Y 1999. Mechanistic aspects of iontophoresis in human epidermal membrane. J Control Release 62(1-2):13-23.

3. Leboulanger B, Guy RH, Delgado-Charro MB 2004. Reverse iontophoresis for non-invasive transdermal monitoring. Physiol Meas 25(3):R35-50.

4. Li SK, Ghanem AH, Peck KD, Higuchi WI 1997. Iontophoretic transport across a synthetic membrane and human epidermal membrane: a study of the effects of permeant charge. J Pharm Sci 86(6):680-689.

5. Luzardo-Alvarez A, Rodriguez-Fernandez M, Blanco-Mendez J, Guy RH, Delgado-Charro MB 1998. Iontophoretic permselectivity of mammalian skin: characterization of hairless mouse and porcine membrane models. Pharm Res 15(7):984-987.

6. Mitragotri S 2003. Modeling skin permeability to hydrophilic and hydrophobic solutes based on four permeation pathways. J Control Release 86:69-92.

7. Prausnitz MR, Bose VG, Langer R, Weaver JC 1993. Electroporation of mammalian skin: a mechanism to enhance transdermal drug delivery. Proc Natl Acad Sci U S A 90(22):10504-10508.

8. Zhu H, Peck KD, Li SK, Ghanem AH, Higuchi WI 2001. Quantification of pore induction in human epidermal membrane during iontophoresis: the importance of background electrolyte selection. J Pharm Sci 90(7):932-942.

9. Deen WM 1987. Hindered transport of large molecules in liquid-filled pores. A I Ch E Journal 33(9):1409-1425.

10. Li SK, Zhang Y, Zhu H, Higuchi WI, White HS 2005. Influence of asymmetric donor-receiver ion concentration upon transscleral iontophoretic transport. J Pharm Sci 94(4):847-860.

11. COMSOL, 2008. Electrophoresis - Transport in a capillary column. http://www.comsol.com/showroom/documentation/model/217/ (last accessed 7/25/2011).

12. Banga AK. 1998. Electrically assisted transdermal and topical drug delivery. ed., Bristol, PA: Tayor & Francis. p 172.

13. Pikal M 1990. Transport mechanisms in iontophoresis. I. A theoretical model for the effect of electroosmotic flow on flux enhancement in transdermal iontophoresis. Pharm Res 7(2):118-126.

14. Pikal M 1990. Transport mechanisms in iontophoresis. III. An experimental study of the contributions of electroosmotic flow and permeability change in transport of low and high molecular weight solutes. Pharm Res 7(3):222-229.

15. Pikal M, Shah S 1990. Transport mechanisms in iontophoresis. II. Electroosmotic flow and transference number measurements for hairless mouse skin. Pharm Res 7(3):213-221.

CHAPTER 5

SUMMARY

5.1 Conclusions

Using the modified Nernst-Planck model as a theoretical framework has provided an opportunity to gain insight into the transdermal iontophoresis of cationic and anionic probe permeants under two conditions: 1) when the electric current determining ions and their concentrations were the same on both sides of the HMS membrane (referred to as baseline conditions); and 2) when the current determining ions in the cathodal and anodal chambers differed significantly, specifically with 90 mM sodium chloride in the anodal chamber and with varying concentrations of sodium polystyrene sulfonate (PSS) in the cathodal chamber. While the first condition is the most common in the majority of in vitro studies, the latter condition is more representative of those encountered in most practical applications of transdermal iontophoresis.

When PSS was the main conducting anion in the cathodal chamber, significant changes in the transport behavior of the probe permeants were observed. The transport of nonionic probe permeants increased up to sixfold and remained constant over the hundredfold range of sodium PSS concentration (i.e., 1.37 mg/mL, 13.7 mg/mL, and 137 mg/mL) in the cathodal chamber. The transport of cationic probe permeants increased by up to threefold and remained constant over the same range of sodium PSS concentrations

investigated while the transport of anionic probe permeants decreased with increasing sodium PSS concentrations in the cathodal chamber.

We have used the Nernst-Planck model to calculate the theoretical permeability coefficients ($P_{ion,theor}$) and to compare these with the experimental permeability coefficients ($P_{ion,exp}$) of the ionic permeants. The results of theoretical calculations showed that the cationic probe permeants behaved in a manner consistent with the theoretical predictions of the Nernst-Planck model for pore sizes of around 30 Å. This was true for all cases under baseline conditions as well as for conditions in which the concentration of sodium PSS in the cathodal chamber varied over a hundredfold range (i.e., from 1 mM to 100 mM). The Nernst-Planck theoretical calculations showed that the electric field profiles (see Figure 4.1) were relatively flat (i.e., constant) for pores around 30 Å and independent of the sodium PSS concentration in the cathodal chamber except near the membrane/cathodal chamber interface. The calculations also showed that the concentration profiles of both the current determining ions (see Figures 4.2 – 4.4) and the cationic probe permeant ions (see Figures 4.11 – 4.13), except near the membrane cathodal chamber interface, did not change significantly in response to changes in the sodium PSS concentration in the cathodal chamber. The relatively invariant ion concentration profiles and the relatively constant electric field profiles help to explain the relatively constant $P_{ion,exp}$ values and the relatively good agreement between $P_{ion,theor}$ and $P_{ion,exp}$ for the cationic probe permeants. The theoretical Nernst-Planck calculations also showed good agreement between the experimental and theoretical transference numbers and the experimental and theoretical voltage drops across the membrane.

In contrast with these results showing good agreement between experiment and theory, with the exception of the theoretical calculations with 100 mM PSS in the cathodal chamber, the $P_{ion,exp}$ and $P_{ion,theor}$ values for the anionic probe permeants differed significantly. While the general trends of decreasing anionic probe permeant transport with increasing concentrations of sodium PSS in the cathodal chamber were consistent, the large variation in the theoretically calculated membrane concentrations of the anionic probe permeants was not consistent with the observed $P_{ion,exp}$ values (see figures 4.23 – 4.25 and Tables 4.5 – 4.7). The disagreement between $P_{ion,exp}$ and $P_{ion,theor}$ for anionic probe permeants is believed to be the result of some of the assumptions made in the theoretical Nernst-Planck calculations. One of the key assumptions of the theoretical Nernst-Planck model calculation was to combine all of the pore pathways into a single pore pathway with uniform charge and size characteristics. The HMS pore pathways are likely heterogeneous as discussed in Chapter 4. One may hypothesize, for example, that the large variations in the electric field at the membrane/cathodal chamber interface (see Figure 4.1) that are responsible for the large variations in the anionic probe permeant concentrations in the membrane pores (see Figures 4.23 – 4.25), as predicted in the theoretical calculations, may not be realized if the pore size distributions are considered in the model. In order to better understand the behavior of the anionic probe permeants further experiments and further theoretical studies will be required (see below).

5.2 Future Work

Further experiments would be helpful to investigate the possible shortcoming of the present theoretical modeling approach as it relates to the calculations of $P_{ion,theor}$ for anionic probe permeants. One possibility is to design experiments using a model membrane having well-characterized pore geometry and uniform surface charge characteristics. For instance, using a synthetic cation exchange membrane to generate experimental transport data with anionic probe permeants and with sodium PSS in the cathodal chamber may provide an opportunity to further test the theoretical Nernst-Planck model for a membrane having more homogeneous pore pathways than those of HMS. Should these results with the synthetic membrane demonstrate the ability of the Nernst-Planck model to appropriately describe the transport behavior of the anionic probe permeants, further theoretical studies may be pursued that would include various pore size distributions in the Nernst-Planck calculations.

We would also like to take a closer look at the transport of the PSS oligomers themselves. In the present studies we conducted PSS transport experiments at the highest sodium PSS concentration, i.e., 137 mg/mL (see Chapter 3). Additional PSS transport experiments with 1.37 mg/mL and 13.7 mg/mL sodium PSS in the cathodal chamber may provide a chance to test the agreement between the theoretical Nernst-Planck calculations for the main current conducting anion in the system, PSS, and the experimentally determined fluxes of the same.